Missouri S&T Library and Learning Resources

Scholars' Mine

Doctoral Dissertations | Student Theses and Dissertations

2014

Development of a nitrogen incorporated ultrananocrystalline diamond film based field emitter array for a flat panel X-ray source

Chrystian Mauricio Posada

Follow this and additional works at: https://scholarsmine.mst.edu/doctoral_dissertations

Part of the Nanoscience and Nanotechnology Commons, and the Nuclear Engineering Commons

Department: Mining and Nuclear Engineering

Recommended Citation

Posada, Chrystian Mauricio, "Development of a nitrogen incorporated ultrananocrystalline diamond film based field emitter array for a flat panel X-ray source" (2014). *Doctoral Dissertations*. 2505.
https://scholarsmine.mst.edu/doctoral_dissertations/2505

This thesis is brought to you by Scholars' Mine, a service of the Missouri S&T Library and Learning Resources. This work is protected by U. S. Copyright Law. Unauthorized use including reproduction for redistribution requires the permission of the copyright holder. For more information, please contact scholarsmine@mst.edu.

DEVELOPMENT OF A NITROGEN INCORPORATED ULTRANANOCRYSTALLINE DIAMOND FILM BASED FIELD EMITTER ARRAY FOR A FLAT PANEL X-RAY SOURCE

by

CHRYSTIAN MAURICIO POSADA ARBELAEZ

A DISSERTATION

Presented to the Faculty of the Graduate School of the

MISSOURI UNIVERSITY OF SCIENCE AND TECHNOLOGY

In Partial Fulfillment of the Requirements for the Degree

DOCTOR OF PHILOSOPHY

in

NUCLEAR ENGINEERING

2014

Approved by:

Carlos H. Castaño, Advisor

Hyoung K. Lee

Ayodeji B. Alajo

Shoaib Usman

Ralu Divan

ABSTRACT

As an alternative to conventional X-ray sources, a flat panel transmission X-ray source is being developed. A field emitter array (FEA) prototype to be incorporated as cold cathode in this flat panel X-ray source was fabricated for this work. Using the Particle-in-Cell code OOPIC Pro, an initial FEA was designed through simulations. Based on the simulation results, a FEA prototype was fabricated using conventional microfabrication techniques. Planar nitrogen-incorporated ultrananocrystalline diamond (N-UNCD) films were used as field emitters. This N-UNCD based FEA prototype was composed of 9 pixels distributed in a 3×3 array, with a pixel size of 225×225 µm, and a 500 µm pitch. Each pixel was composed of a N-UNCD-based cathode and a free-standing copper grid used as extraction grid. Field emission from each pixel could be addressed individually. Emission currents per pixel in the order of 0.05 – 3.0 µA were obtained for extraction fields between 4 and 20 V/µm. Delamination issues were found in the microfabrication of the first FEA prototype. Consequently, a second generation N-UNCD based 3×3 FEA was designed and fabricated. In this design, the free-standing grid was replaced by a tungsten layer composed of a matrix of 11×11 extraction gates. Each extraction gate had a circular aperture of 6 µm in diameter. These design changes solved the delamination issues found for the first prototype. Also, for an extraction field of 7 V/µm, an emission current around 0.14 µA per pixel was measured; this value is higher than the 0.08 µA per pixel obtained from the initial FEA prototype at the same extraction field.

Keywords: Field Emission, Cold Cathode, Flat Panel Transmission X-Ray Source, OOPIC Pro, Ultrananocrystalline Diamond Films, N-UNCDs, Field Emitter Arrays.

ACKNOWLEDGMENTS

I owe my deepest gratitude to my advisor, Dr. Carlos H. Castaño for his continued support throughout these years. His enthusiasm, guidance and funding, made possible and easier the completion of this work. Also, I would like to thank Dr. Hyoung K. Lee for being a continuous source of ideas for my research.

I also would like to express my gratitude to Prof. Pieter Kruit for allowing me to join the Charged Particle Optics group at TU-Delft as a visiting researcher. This appointment provided me with invaluable research and personal experiences. I am grateful to all the members of the CPO group; especially Leon van Kouwen and Jan de Looff for sharing all their experience on Schottky electron sources, field emission, electron optics, high vacuum systems and high voltage electronics. Special thanks to Takashi and Angela who made my stay in Delft full of good memories.

Having access to the clean room facilities of the Center for Nanoscale Materials at Argonne National Laboratory was key for the success of this project. Thanks to the CNM's scientific staff for making available their microfabrication experience and expertise, especially Dr. Anirudha Sumant who made sure of making available N-UNCD samples every time they were required. Also, I have to give a big and special thank you to Dr. Ralu Divan; everything I know about microfabrication comes from her.

I am indebted to my professors at the National University of Colombia. During my bachelors they provided me with the basis needed to successfully complete this stage of my career. I am especially grateful to Carlos Sanchez, Carlos M. García, Diego Durango, Hernán Álvarez and Veselina Pashova.

My officemates Lucas Tucker and Edwin Grant provided me a fun and stimulating environment throughout these years. Special thanks to Lucas for letting me win that triathlon, and to Edwin for all his contributions to the experiments of this work.

Lastly, and most importantly, I want to thank my mom Miriam Arbeláez, my brother Mateo Gómez and my pretty girlfriend Heveline Vieira. They are the greatest support I have in life and the biggest motivation for trying to be a better person and professional every day.

TABLE OF CONTENTS

Page

ABSTRACT iii

ACKNOWLEDGMENTS iv

LIST OF ILLUSTRATIONS viii

LIST OF TABLES xi

SECTION

1. INTRODUCTION 1

  1.1. CONVENTIONAL X-RAY TUBES 1

  1.2. ADDRESSABLE FLAT PANEL TRANSMISSION X-RAY SOURCE 3

  1.3. RESEARCH MOTIVATION 5

  1.4. DISSERTATION ARRANGEMENT 6

2. BACKGROUND AND RATIONALE 8

  2.1. ELECTRON SOURCES 8

    2.1.1. Thermionic Emission 8

    2.1.2. Photo-Induced Emission 9

    2.1.3. Secondary Emission 9

    2.1.4. Schottky Emission 9

    2.1.5. Field Emission 9

  2.2. ELECTRON FIELD EMISSION 10

  2.3. ULTRANANOCRYSTALLINE DIAMOND FILMS 13

    2.3.1. Polycristalline Diamond Films. 14

    2.3.2. Synthesis of Polycrystalline Diamond Films 15

    2.3.3. Properties of UNCD Films. 19

  2.4. UNCD FIMLS AS FIELD EMITTERS 19

3. FIELD EMISSION SIMULATIONS 23

  3.1. PARTICLE-IN-CELL CODES 23

  3.2. SIMULATION PROCEDURES 24

  3.3. PRELIMINARY OOPIC PRO SIMULATION RESULTS 30

    3.3.1. Total Number of Particle and Convergence 30

3.3.2. Electron Trajectories 31
3.3.3. Current Density as a Function of Extracting Voltage (J_{FN}-V curves) 33
3.3.4. Space-Charge Effects 35
3.3.5. Energy Distribution of Electrons at the Anode 37
3.3.6. Focal Spot Size Versus Grid Voltage. 40
3.3.7. Conclusions from Preliminary Simulations 41
4. EXPERIEMENTAL SET-UP 43
4.1. VACUUM SYSTEM CONFIGURATION 43
4.1.1. Vacuum Chamber 44
4.1.2. Electrical Feedthroughs 45
4.1.3. Vacuum Pumps and Gauges 45
4.1.4. DC Power Supplies 45
4.1.5. X-Ray Detection System 46
4.2. TESTING OF EXPERIMENTAL SET-UP 47
4.2.1. Field Emission Characteristics 48
4.2.2. X-Ray Generation Characteristics 49
5. FIRST GENERATION FIELD EMITTER ARRAY 53
5.1. PROTOTYPE FABRICATION 53
5.2. FIELD EMISSION TESTING 58
6. SECOND GENERATION FIELD EMITTER ARRAY 65
6.1. FITTING SIMULATION TO EXPERIMENTAL RESULTS 65
6.2. DESIGN OF ALTERNATIVE FEA GEOMETRIES 67
6.2.1. Single Gate Configuration 67
6.2.2. Double Gate Configuration 72
6.3. ALTERNATIVE N-UNCD FEA FABRICATION PROCEDURE 77
6.4. FE TESTING OF THE SINGLE GATE FEA 81
6.5. FABRICATION OF THE DOUBLE GATE FEA 84
7. CONCLUSIONS 86
8. RECOMMENDATIONS FOR FUTURE WORK 89

APPENDICES

A.INPUT FILE USED FOR THE OOPIC PRO SIMULATIONS...............................91

B. DERIVATION OF THE FOWLER-NORDHEIM EQUATION......................... 115

C. TABULATED VALUES FOR THE FN FUNCTIONS s(y) and v(y)……........… 119

BIBLIOGRAPHY... 121

VITA 126

LIST OF ILLUSTRATIONS

Figure Page

1.1. Main components of a conventional X-ray tube. 2

1.2. Schematic diagram of the distributed flat panel X-ray source. 3

1.3. Cross sectional view of the proposed flat panel X-ray source. 4

1.4. Schematic of the proposed 3x3 field emitter array prototype. 5

2.1. Mechanisms for emission of electrons from a solid material [9, 14] 10

2.2. Mechanism for field emission of electrons from a solid material [15]. 11

2.3. Variation of the functions $\upsilon(y)$ and $t(y)$ as a function of y [15]. 13

2.4. Top: Representation of NCD film, bottom: Representation of UNCD film [22]. 14

2.5. 915 MHz large area MPCVD system used for UNCD films growth at the Center for Nanoscale Materials, Argonne National Laboratory [23]. 15

2.6 SEM images of the films prepared by MPCVD with different mixtures of Ar, H_2 and CH_4 [18] 17

2.7. Compositional map of the Ar-H_2-CH_4 system for diamond films growth [18] 18

2.8. Conductivity of UNCD films as a function of nitrogen content in the gas phase [25]. 19

2.9. SEM images of the samples used for field emission measurements of several N-UNCD coated microstructures [20] 20

2.10. Anode current (µA) vs. cathode voltage (V) from N-UNCD on Si substrates with different topographies [20] 21

3.1. Diagram of the PIC algorithm [33] 24

3.2. Triode structure used for the field emission simulations 25

3.3. Screenshot of actual geometry modeled in OOPIC Pro 27

3.4. Dimensions defined for the extraction grid in the PIC 2D simulation 28

3.5. Total number of emitted electrons in the triode structure as a function of time 30

3.6. Trajectory of the electron beam when no focusing lenses are used 31

3.7. Trajectory of the electron beam when focusing lenses are used 33

3.8. J_{FN}-V curves – Anode current density (mA/mm^2) as a function of the grid voltage at different anode voltages 34

3.9. Current density at the anode as a function of time, no focusing lenses are used...... 36

3.10. Electron trajectory in the triode structure 37

3.11. Energy distribution of electrons striking the anode 38

3.12. Average energy of electrons reaching the anode vs. anode (accelerating) voltage 40

3.13. Focal spot size as a function of the extracting voltage 41

4.1. Overview of the vacuum system used for the experiments 43

4.2. Vacuum chamber and Al upright style frame. 44

4.3. Experimental Apparatus... 47

4.4. CNT-based electron source used for testing the experimental set-up...................... 48

4.5. *I-V* behavior for the CNT-based electrons source.. 49

4.6. Experimental set-up used inside the vacuum chamber to evaluate the generation of X-rays.. 50

4.7. X-ray spectrum at different electron beam energies obtained for the CNT-based electron source 51

4.8. Anode potential versus maximum X-ray energy 52

5.1. Right: Flat-Panel X-ray source. Left: Proposed 3x3 FEA prototype....................... 53

5.2. Process flow of the microfabrication process of the FEA microfabrication process.54

5.3. Electrical circuit designed for individually addressable pixels............................... 56

5.4. Micrographs of the N-UNCD prototype obtained during the microfabrication process... 57

5.5. Optical micrographs of the first 3×3 N-UNCD FEA prototype 58

5.6. Micro fabricated N-UNCD 3x3 field emitter arrays.. 59

5.7. I-V characteristics of field emitted electrons from given N-UNCD pixels 60

5.8. Fowler-Nordheim plots of the cathode-grid configurations tested...........................61

5.9. High field regin of the FN Plots used to calculate β as a function of $\phi_{N\text{-}UNCD}$ for the two cathode-grid configurations tested. 62

5.10. Optical micrographs of samples showing copper delamination and grid removal issues. 63

6.1. *I-V* characteristics of the first N-UNCD FEA prototype. 66

6.2. Single gate geometry proposed for the second generation N-UNCD FEA. 67

6.3. Electron beam trajectories for different extraction gate apertures........................... 68

6.4. Current-voltage (*I-V*) behavior of the different triode configurations simulated 69
6.5. Space-charge limitation effects at different cathode voltages 71
6.6. Proposed double-gate N-UNCD FEA configuration. 72
6.7. Electron beam trajectories for the 10 μm ((a) and (b)), and 16 μm ((c) and (d)) double-gated structures, gate aperture: 6 μm 73
6.8. Electron beam trajectories for the 6 μm (top) and 16 μm (bottom) double-gated structures, gate aperture: 10 μm 74
6.9. Electron emission characteristics for the double-gate structure in comparison to the single gate structure, gate voltage: 0 V, cathode voltage: -35 V...................... 75
6.10. Electron emission characteristics for the double-gate structure in comparison to the single gate structure, gate voltage: 0 V, cathode voltage: -40 V...................... 76
6.11. Microfabrication process of the second generation single gate N-UNCD FEA..... 77
6.12. SEM images of the N-UNCD film used in the second generation FEA................. 79
6.13. Optical micrographs of the second generation N-UNCD FEA 80
6.14. SEM images of the second generation N-UNCD FEA showing details of the single extraction gate.. 80
6.15. SEM/EDX analysis performed in one of the gates of the second generation N-UNCD FEA.. 81
6.16. Measured *I-V* characteristics of the single gate N-UNCD FEA at different times. 82
6.17. Influence of anode high voltages on the *I-V* characteristics of the single gate N-UNCD FEA.. 83
6.18. Comparison of the *I-V* characteristics of the first and second generation N-UNCD FEAs. 83
6.19. Proposed double gate second generation N-UNCD FEA for microfabrication....... 84
6.20. Micrographs indicating issues found during the attempt of microfabricating a double gate N-UNCD FEA 85

LIST OF TABLES

Table Page

1.1. Design variables for the distributed transmission flat panel X-ray source 6

2.1. Ratio of reactant gases used for the MPCVD growth of diamond films [18]........... 16

3.1. FN parameters used in initial OOPIC Pro simulations 26

3.2. Geometric and electric parameters used for the OOPIC Pro simulations................. 28

5.1. Field emission characteristics of the N-UNCD FEA prototype................................ 63

1. INTRODUCTION

This section gives an outline on the work performed for this dissertation and the motivation behind it. It begins by providing an overview on conventional X-ray tubes and their mechanism of operation. This sets the basis for later introducing the conceptual design of the addressable Flat-Panel Transmission X-ray Source. Finally, the specific objectives of this research and the arrangement of this dissertation are presented.

1.1. CONVENTIONAL X-RAY TUBES

In 1895, while he was working with electrical charges flowing through vacuum tubes, Wilhelm C. Roentgen noticed an “unknown type rays” that would produce light when they strike a fluorescence material. After performing additional experiments, Roentgen realized he had actually discovered a new type of rays, which he called X-rays. This discovery of the X-rays opened the door to a new way of practicing medicine, allowing doctors to view inside their patients without the need of physically opening their bodies [1]. This discovery was later used by William Coolidge to develop the hot cathode X-ray tube, making a major contribution to move forward the field of radiology. Coolidge’s invention also set the basis for the conventional X-ray sources used today.

These conventional X-ray sources are composed of a cathode and an anode encapsulated in a glass envelope as shown in Figure 1.1 [1]. Electrons are thermionically emitted at the cathode, which is composed of one or several helical coil filaments made of a refractory material such as Mo or Mo-W alloys. During operation, filaments are kept at temperatures as high as 2200 °C and carry currents ranging between 3.5 A and 5 A [1]. A high voltage (30 to 150 kV) applied across the cathode-anode gap is used to accelerate the emitted electrons toward the anode. The anode or target is usually made of a thin tungsten or tungsten alloy [1]. A field shaping technique is used in order to focus the high energy electrons on a small region (0.1 to 1.5 mm^2) of the target. The small region where electrons strike the target is denominated *focal spot*. X-rays are produced by Bremsstrahlung interactions between high energy electrons striking the target and the

target atoms [1]. The small region where electrons strike the target is denominated *focal spot*.

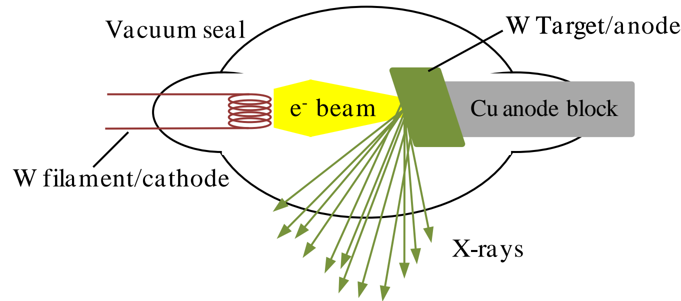

Figure 1.1. Main components of a conventional X-ray tube.

Conventional X-ray sources are used today for medical imaging, industrial examination and homeland security inspection. However, despite the wide diversity of applications, the mechanism behind X-ray generation has changed little since the first X-ray source was developed over a century ago.

The generation of X-rays from the single focal spot where high energy electrons strike the X-ray target leads to several constraints. For instance, this characteristic makes heat dissipation in the X-ray target an important operational problem. In fact, X-ray generation due to Bremsstrahlung interactions is a very inefficient process. More than 99% of the total electron energy is converted into heat in the target, leading to X-ray generation efficiencies of less than 1% [1]. In consequence, heat accumulation in the target and operation of X-ray tubes are always limited by the ability to dissipate heat in the tube.

In addition, X-rays generated from a single focal spot yield a widely diverging X-ray cone beam, leading to geometric distortions of the patient anatomy or of internal 3D structures of imaged objects due [1]. Also, for patient safety and X-ray optics reasons, the generation of X-rays from a single focal spot demands large distances between the source and the imaged object. It results in bulkier imaging devices and bigger imaging room requirements [1].

To overcome these problems, an addressable flat panel transmission X-ray source is proposed. Similar to the way old tube television were replaced by modern flat panel screens, the flat panel X-ray source proposed in this work is intended to take advantage of the progress seen in the field of vacuum microelectronics to move forward the field of X-ray imaging.

1.2. ADDRESSABLE FLAT PANEL TRANSMISSION X-RAY SOURCE

As an alternative to the problems of conventional X-ray sources, a field emission (FE) based flat panel transmission X-ray source is being developed. This source is based on a two dimensional array of micro (200 μm) X-ray cells similar in format to conventional flat panel displays (see Figure 1.2) [2].

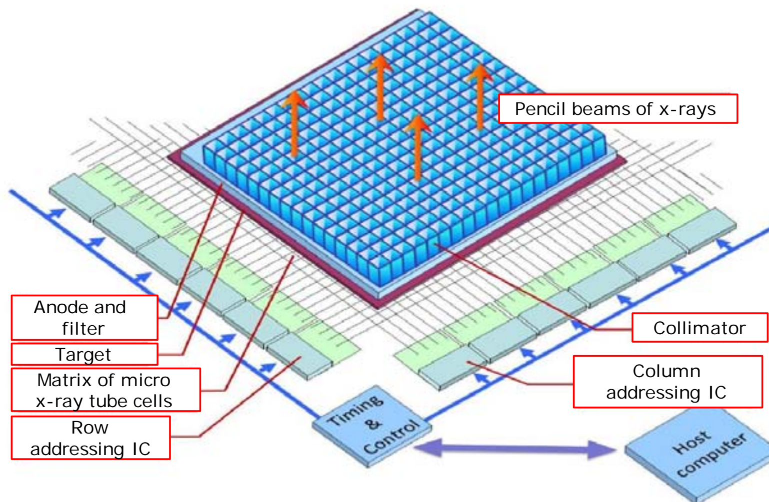

Figure 1.2. Schematic diagram of the distributed flat panel X-ray source.

In this design, X-ray generation in each of the micron-sized cells can be controlled independently, allowing the source to be operated in scanning mode; such that only one or a few cells produce X-rays at a time. Using this technique, while coupling the system to an anti-scatter grid-based detector, scattered X-ray photons can be almost completely rejected, resulting in the production of high quality, high contrast images with

minimum dose. Also, the parallel X-ray beams generated in each micro X-ray source will reduce image distortion due to magnification, and the space required between the source and the image detector will be smaller.

As shown in Figure 1.3, each micro cell is composed of a triode structure. In this triode structure, electrons extracted from the *cathode* are accelerated towards an anode material where X-rays are produced by Bremsstrahlung interactions [2,3]. A metallic layer with small apertures is used as extraction grid. In order to extract the electrons from the cathode, low voltage bias are applied between the cathode - extraction gate gap. The emitted electrons are accelerated toward the anode due to high voltage bias applied between the cathode - anode gap. High voltages between 30 ~ 150 kV are used to accelerate the electrons toward the anode. Transmission X-rays are generated at the anode by Bremsstrahlung interactions between a thin X-ray target material and high energy electrons [3]. In this X-ray source, electrons are generated by field emission, instead of using the conventional hot filament.

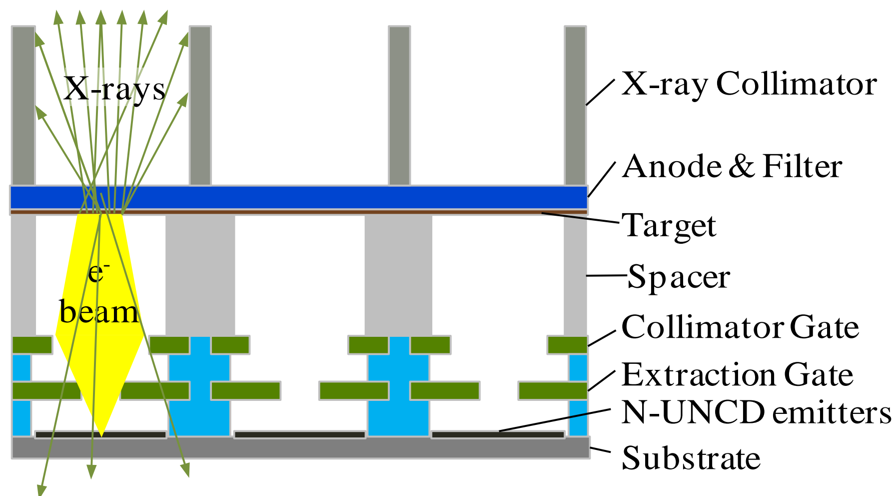

Figure 1.3. Cross sectional view of the proposed flat panel X-ray source.

Field emission (FE) is preferred over thermionic emission because no heating is required to extract the electrons and the emission of electrons can be controlled using an externally applied electric field [2, 4-11]. It allows for individual, fast and accurate

control of the X-ray generation from each micro cell, enabling the desired scanning mode operation of the X-ray source. In addition, when operating in scanning mode, heat generated from a single cell can be dissipated over the entire anode layer, offering an alternative to the problem of heat accumulation in the X-ray target. These interesting features make this addressable flat panel transmission X-ray source technically and scientifically attractive.

1.3. RESEARCH MOTIVATION

This work was carried out as part of the development of the Flat-Panel X-ray source described above. The main objective of this work is to design and fabricate a robust, reliable FE electron source prototype to be incorporated as cold cathode into the X-ray source. As shown in Figure 1.4, the proposed prototype is composed of nine individually addressable pixel arranged in a 3×3 arrays, where each pixel is corresponds to a triode structure.

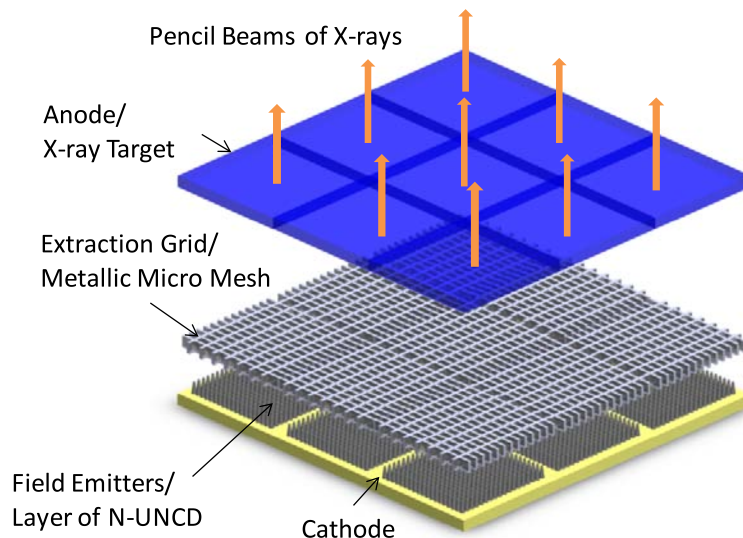

Figure 1.4. Schematic of the proposed 3x3 field emitter array prototype.

The field emission characteristics of the developed prototype are evaluated both experimentally and through simulations. In early stages of this project, carbon nanotubes (CNTs) were considered as potential field emitter materials. However, later considerations led to the selection of nitrogen-incorporated ultrananocrystalline diamond (N-UNCD) films as the field emitter materials to be used in this work. Further details about the N-UNCD films and the electron field emitter prototype are presented later in this work. A summary of variables analyzed for the design of a firs electrons field emitter prototype is presented in Table 1.1

Table 1.1. Design variables for the distributed transmission flat panel X-ray source.

Component	**Variable**	**Dimension**
Grid	Distance	2 - 30 µm
	Aperture	5 - 30 µm
	Material	Copper, Tungsten
Anode	Anode distance	0.1 - 1.0 cm
	Material	Tungsten, Molybdenum
Spacers	Material	SiO_2, Glass
Electrical parameters	Anode potential	0 - 100 kV
	Grid potential	0 - 200 V
	Focusing Voltage	0 - grid potential

1.4. DISSERTATION ARRANGEMENT

The reminder of this dissertation is organized as follows. In Section 2, background information about field emission, electron sources and N-UNCDs is presented. A brief description about the Particle-In-Cell method used for the simulations is also included.

Section 3 presents preliminary simulation work carried out to evaluate the technical feasibility of this project. The two dimensional Particle in Cell (PIC) code OOPIC Pro was used for the simulations. Based on this simulation work, a first design

for the electron source is obtained. Results presented in this section include the evaluation of the trajectory of emitted electrons with and without focusing structures. J_{FN}-V curves obtained for different gate and anode voltages. A correlation between the accelerating voltage and the average energy of electrons striking the anode is also presented. The current density and energy distribution of electrons at the anode is included as well. Section 4 introduces the experimental set-up used for the FE measurements and its calibration. In this section, FE and X-ray measurements obtained with a commercial electron source are presented.

In Section 6, the microfabrication work and testing of the N-UNCD field emitter arrays (FEA) is presented. This section shows results obtained for two different FEA configurations. In this section starts by showing the FE results obtained for a first FEA prototype. Later, experimental results are compared to a new set of simulations and a new FEA design if proposed. Finally, the microfabrication and testing of this new FEA design is presented.

In Section 7 the main results obtained from this work are discussed. Finally, recommendations for future work and the conclusions of this dissertation are found in Section 8.

2. BACKGROUND AND RATIONALE

2.1. ELECTRON SOURCES

Vacuum microelectronics refers to the fabrication and study of devices of micrometric dimensions that operate with electrons in vacuum. This term was first used in 1988 at the 1st Vacuum Microelectronics Conference held Williamsburg, Virginia [12]. Since then, this field has received a growing amount of attention. This growing attention is supported by the possibility of fabricating a number of novel devices while taking advantage of microfabrication technologies already in place for the semiconductor industry. One of these applications is possibility of using field emission sources in X-ray tubes to replace the bulky thermionic sources. This will lead to a revolution the field of X-ray imaging similar to the one already seen with TV as they made the transition from the cathode ray tube into flat panel displays.

In this regard, a fundamental element in X-ray sources, as well as in other systems where vacuum microelectronics can find an application, is doubtless the electron beam. Therefore, the electron source used to produce this electron beam can be considered as one of the main constituents in conventional X-ray systems. It is the component in charge of providing the electrons that will later be modulated, accelerated, and modified to finally strike and interact with the X-ray target were X-rays are produced. In order to perform their job, electron sources need to provide a mechanism to get enough electrons out of a solid material and direct them into a beam. It implies supplying enough energy to make electrons overcome the barrier (work function) that keeps them from escaping the surface of the solid material. There are several mechanisms to make electrons overcome this barrier. In fact, electron sources can be classified according to the mechanisms used to overcome the work function and extract electrons from the emitter material. The following electron emission mechanisms are usually considered [13].

2.1.1. Thermionic Emission. Thermal energy is provided to heat an emitter material. When the temperature is high enough (~2300 K), electrons from the tail of the energy distribution will have sufficient energy to overcome the potential barrier and leave the emitter surface. This is probably the most widely used mechanism in electron sources and it is the mechanism employed in today's conventional X-ray sources.

2.1.2. Photo-Induced Emission. In this emission mechanism, an external source is used to excite the electrons and overcome the emitter´s work function. More specifically, a laser beam of sufficient energy is used to overcome the potential barrier and generate photo emission.

2.1.3. Secondary Emission. In secondary electron emission, a target material is hit with primary electrons with sufficient energy to produce enough secondary electrons. This type of electron sources use the secondary electrons generated by the interaction between the incident beam and the target material.

2.1.4. Schottky Emission. In Schottky electron sources, a sharp tungsten tip or Schottky emitter is heated up to about 1800 K and a high electric is used to lower the work function by the "Schottky effect". Thermal electrons are then emitted by the combination of heat and electric field applied to the emitter.

2.1.5. Field Emission. Under certain geometrical characteristics, an external field can be enhanced in sharp edges or tips or a material. Field emitters take advantage of this geometrical enhancement to lower the potential barrier and make it thin enough that electron can tunnel through it. In this mechanism, the emission electron is controlled by the externally applied electric field. Consequently, field emission is a preferred mechanism when fact, accurate modulation of the electron beam is required. It is because of these characteristics that FE was the mechanism selected for our electron source prototype.

A summary of the mechanisms described above is shown in Figure 2.1 [9, 14].

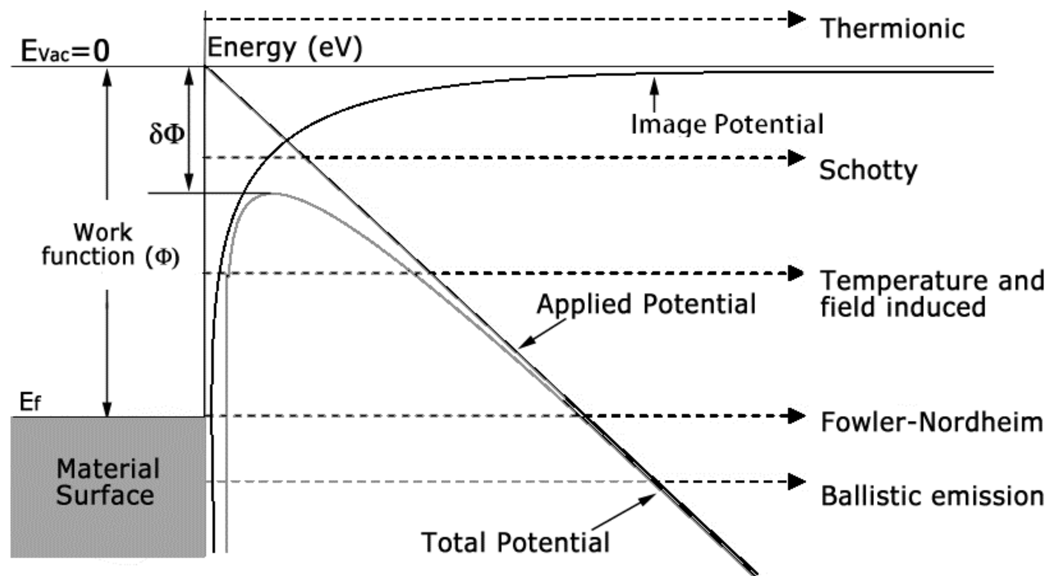

Figure 2.1. Mechanisms for emission of electrons from a solid material [9, 14].

2.2. ELECTRON FIELD EMISSION

Field emission (FE) refers to the process of extracting electrons from the surface of a material under the influence of an externally applied electric field. Figure 2.2 shows a representation of the process of field emission. As shown in Figure 2.2, at room temperature, electrons in the surface of a material stay near the Fermi level. In order to leave the emitter's surface, electrons need to overcome a potential barrier whose height is determined by the material's work function (Ø). This work function is given by the difference in height between the Fermi level and the vacuum level; and it is usually in the order of a few eVs. As shown in Figure 2.2, in the absence of high electric fields, the potential barrier U_x (eV) is infinite in width and its shape is determined exclusively by image forces given by the expression $-e^2/4x$, where x (Å) is the distance from the surface of the emitter material [5, 6, 14]. In this case, for the emission of electrons to happen, they are required to jump over this potential barrier. This is the mechanism behind the *thermionic emission* of electrons from surfaces at high temperatures [4, 9, 14].

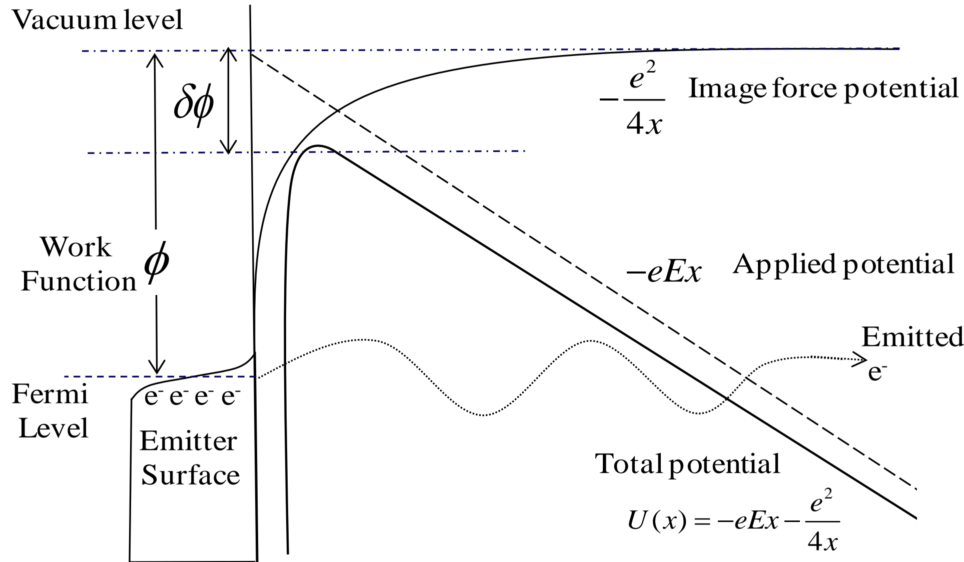

Figure 2.2. Mechanism for field emission of electrons from a solid material [15].

On the other hand, if a strong electric field (E) in the order of 10^7 V/cm to 10^8 V/cm is applied at the surface of a material, the potential barrier is deformed by the Schottky effect. See Figure 2.2 [4, 5]. In consequence, this barrier becomes finite in width, with its shape is now determined by the expression $-(e^2/4x) - eFx$ [4, 5]. These changes induced to the potential barrier allow electrons to tunnel through it by quantum mechanical effects. Therefore, under the effect of these strong electric fields, electrons can be emitted into free space without the need of having to jump over the potential barrier. This is the mechanism behind field emission [4-6, 14].

FE was first explained quantitatively by Fowler and Nordheim in 1928 [4]. They established that at low temperatures, the FE current density is a function of the work function (*Ø*) of the material, the strength of the externally applied electric field (E), and a field enhancement factor (*β*) due to special geometric configurations of the emitter material [4, 9].

Based on the concepts presented above, Fowler and Nordheim developed an expression to quantify the FE current density as a function of the externally applied electric field (*E*). The general form of the Fowler-Nordheim (FN) equation is:

$$J_{FN} = \frac{A_{FN}(\beta E)^2}{t^2(y)\phi} \exp\left(\frac{B_{FN} v(y) \phi^{3/2}}{\beta E} \right) \quad (1)$$

with,

$$A_{FN} = \frac{e^3 8\pi}{h_p} = 1.5415 \times 10^{-6} \; [A \; eV \; V^{-2}] \quad (2)$$

and

$$B_{FN} = -\frac{4}{3} \frac{(2m_e)^{1/2}}{e \; (h_p / 2\pi)} = 6.8309 \times 10^9 \; [eV^{-3/2} \; V \; m^{-1}] \quad (3)$$

In this equation, J_{FN} is the field emission current density [mA/mm^2], E is the electric field acting over the emitting surface [V/m], β is a field enhancement factor, ϕ corresponds to the characteristic work function of the emitting material [eV], e and m_e are the charge and mass of the electron respectively, and h_p is the Planck's constant. The FN equation also includes other correction parameters that can be calculated using the functional forms:

$$y = (e^3 E)^{1/2} / \phi \, , \quad (4)$$

$$t(y) = \upsilon(y) - (2y/3)(d\upsilon(y)/dy) \quad (5)$$

and,

$$\upsilon(y) = 1 - C_v y^2 \quad (6)$$

Further details in the derivation of the FN equation are provided in Appendix B. In addition, tabulated values of $\upsilon(y)$ and $t(y)$ are presented in Appendix C. Also, a graphical representation of the functions $\upsilon(y)$ and $t(y)$ with respect to y is show in Figure 2.3. C_v is a correction factor also discussed elsewhere [16].

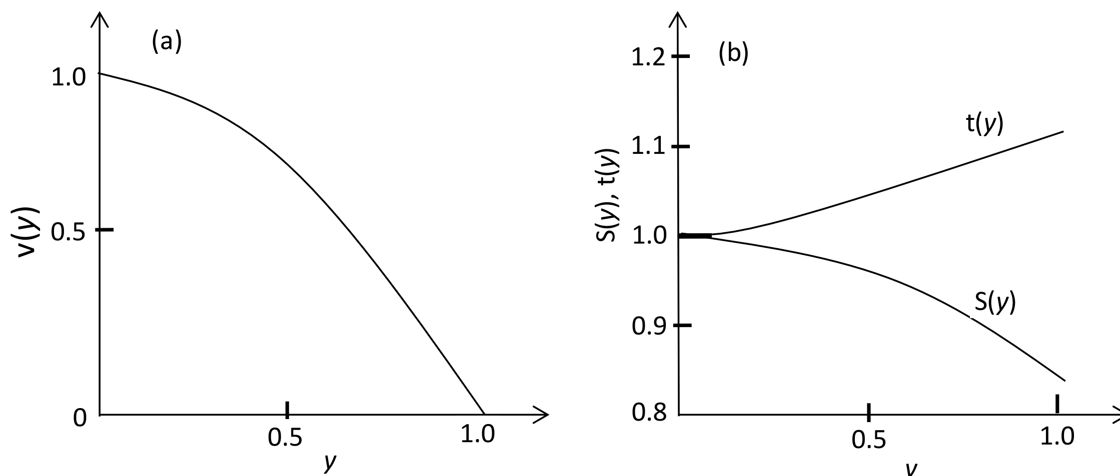

Figure 2.3. Variation of the functions $\upsilon(y)$ and $t(y)$ as a function of y [15].

2.3. ULTRANANOCRYSTALLINE DIAMOND FILMS

Advances in microfabrication have led to the necessity of developing materials capable of supporting the current and future needs for new micro and nanofabrication techniques, alternative architecture of micro and nanodevices and higher functionality in the macro and nanoscale [17]. Due to properties such as low or negative electron affinity, chemical and mechanical stability and high thermal conductivity, polycrystalline diamond films are interesting materials to growing attention as emerging materials interesting materials to address the needs mentioned above [17,18]. Applications of polycrystalline diamond films have been studied for multiple process and devices, including: coatings for mechanical pumps [19], field emission cathodes [20], field emission displays, high frequency micro and nanodevices [21], and X-ray sources [7, 8]. Polycrystalline diamond films typically consist of several crystallites with sizes in the range of micrometers to a few nanometers. In fact, these films are classified according to the size of their crystals. In this section, the factors leading to the transition from microcrystalline (MCD) to ultrananocrystalline diamond films (UNCD) will be discussed. Also, an overview on nitrogen-incorporated ultrananocrystalline diamond (N-UNCD) films and previous work on their field emission properties will be presented.

2.3.1. Polycrystalline Diamond Films. Micro and nanodiamod films can be described as polycrystalline films of diamonds with grain sizes in the range of few hundreds of nanometers to a few nanometers. According to their grain size, polycrystalline diamond films are classified into three categories: microcrystalline diamond (MCD) films, nanocrystalline diamond (NCD) films and ultrananocrystalline diamond (UNCD) films [17, 25]. In general, MCD films have grain sizes greater than a few hundred nanometers, rough surfaces and wide grain boundaries. NCD films have grain sizes in the order of 100 to 10 µm and are usually smoother than MCD films. Due to their grain size, they have a large number of grain boundaries with graphitic impurities. On the other hand, UNCDs are much smoother and denser films when compared to NCDs. Their grain sizes range between 2 and 10 nm [17, 18, 22]. In Figure 2.4 a representation of the structure of NCD and UNCD films is shown [22].

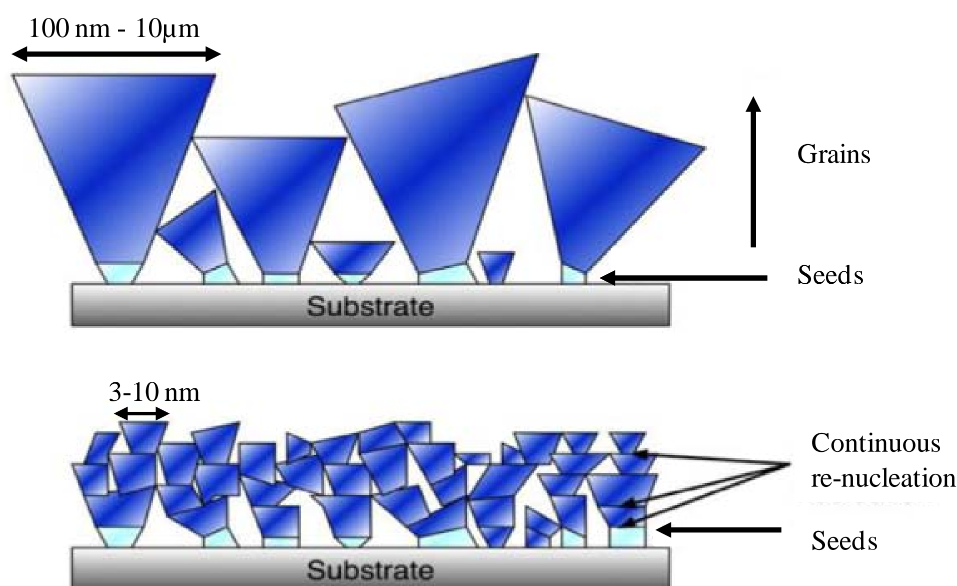

Figure 2.4. Top: Representation of NCD film, bottom: Representation of UNCD film [22].

Figure 2.4. indicates how NCD films, crystals grow as a single element, yielding bigger grain sizes when compared to UNCDs. This is due to the chemistry of synthesis of

UNCDs which favors the growth of the crystals through a continuous re-nucleation process, yielding smaller grain sizes [22].

2.3.2. Synthesis of Polycrystalline Diamond Films. The standard techniques for the growth of polycrystalline diamond films on non-diamond substrates are: Hot filament chemical vapor deposition (HFCVD) and Microwave Plasma Enhanced Chemical Vapor Deposition (MPCVD) [18- 22].

Previous the growth process of these polycrystalline diamond films, the surface on which the films are to be growth are treated to promote continuous and uniform growth of the diamond film. This surface treatment is called *seeding* and corresponds to the embedding of diamond nanoparticles on the surface of the substrate to be used for the growth of the diamond film, see Figure 2.4 [17 - 22]. Following the seeding process, growth of diamond films is based on CVD techniques involving hydrogen-rich chemistry in the case of MCD and NCD films [18] and argon-rich chemistry in the case of UNCDs [17]. The most popular method for the growth of polycrystalline diamond films is the MPCVD. In Figure 2.5 a typical MPCVD system is shown.

Figure 2.5. 915 MHz large area MPCVD system used for UNCD films growth at the Center for Nanoscale Materials, Argonne National Laboratory [23].

When MPCVD is used as growing method, a microwave energy source activates the gases inside the vacuum chamber used to grow the films. A study carried out by Zhou, et. al. in 1998 analyzed the morphology diamond films grown by MPCVD using different ratios of gas reactants in the growth chemistry[18]. This study showed that the crystalline structure of polycrystalline diamond films is determined by the plasma chemistry used during the growth process. In fact, Zhou's results indicated that there is a transition from microcrystalline to nanocrystalline and ultrananocrystalline diamond films, which is driven by different ratios of $Ar/H_2/CH_4$ in the growth chemistry. The $Ar/H_2/CH_4$ ratios used in Zhou's study are summarized in Table 2.1.

Table 2.1. Ratio of reactant gases used for the MPCVD growth of diamond films [18].

Sample #	**Reactant gas (vol%)**			**Structure**
	Argon	**Hydrogen**	**Methane**	
1	2	97	1	MCD
2	20	79	1	MCD
3	40	59	1	MCD
4	60	39	1	MCD
5	80	19	1	MCD
6	90	9	1	NCD
7	97	2	1	NCD
8	99	0	1	UNCD

For Zhou's experiments, the CH_4 flow rate in the vacuum chamber was kept constant at 1 sccm, while H_2 and Ar flow rates ware varied from 0 to 99 sccm. The growth temperature was set at 800 ºC and the total pressure, and input power were set at 100 Torr and 1200 W respectively [18]. These conditions are representative of the typical conditions used for the growth of diamond films by MPCVD.

Using the conditions stipulated by Zhou, et. al., and summarized in Table 2.1 [18], the microstructure of the films obtained was analyzed by scanning electron microscopy (SEM). These SEM micrographs exhibit a clear change in the diamond films surface morphology as the growth chemistry is modified. In Figure 2.6-(a) a film with well-defined microcrystalline structure can be observed. As the ratio H_2/Ar is reduced, the grain size is reduced as well, as seen in Figures 2.6 (b) through (e). For Figures 2.6 (e) - (f), the edges of the large size diamond crystals begin to disappear and diamond crystallites of nanometric scale become more abundant.

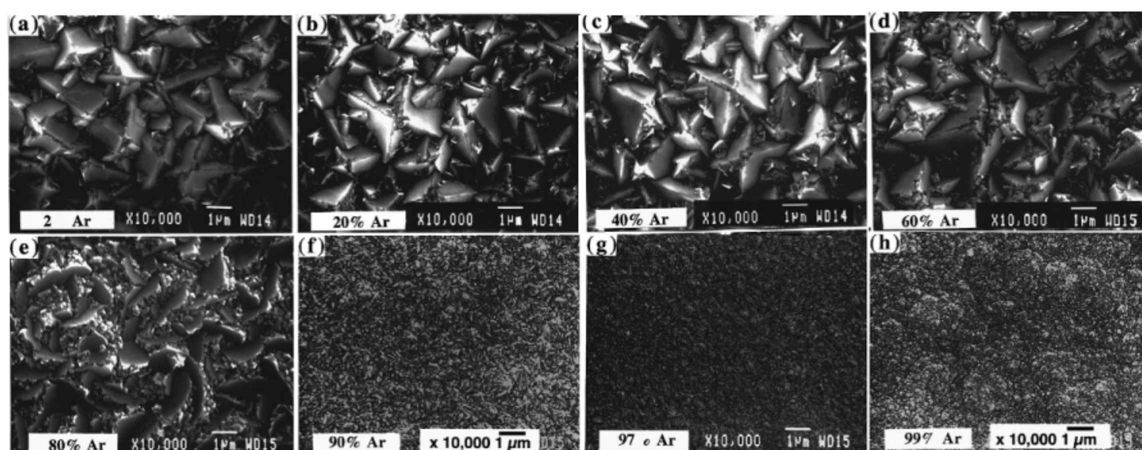

Figure 2.6 SEM images of the films prepared by MPCVD with different mixtures of Ar, H2 and CH4. (a) film 1, (b) film 2, (c) film 3, (d) film 4, (e) film 5, (f) film 6, (g) film 7, and, (h) film 8 [18].

This change in the microstructure indicates a transition from a microcrystalline structure into a nanocrystalline structure for the diamond films. Furthermore, as shown in Figure 2.6 (h), the grain size of the diamond film can be further reduced in the cases in which the growth chemistry was composed only of CH_4 and Ar. This further reduction of the grain size in the absence of H_2 in the growth chemistry results in the production of ultrananocrystalline diamond (UNCD) films with grain sizes in the order of 3 to 10 nm [18, 20]. These results can be compared with the ones obtained by Li, et, al., [24]. Using a HFCVD they also analyzed the microstructure of polycrystalline diamond films for different Ar/H_2/CH_4 mixtures. Their results are summarized in Figure 2.7, were a

transition from MCD films into NCD films is observed as well. Following a similar line to the work presented by Zhou et. al., Li's results also indicate that the transition from MCD to NCD films is driven by a lower proportion of H_2 in the growth chemistry.

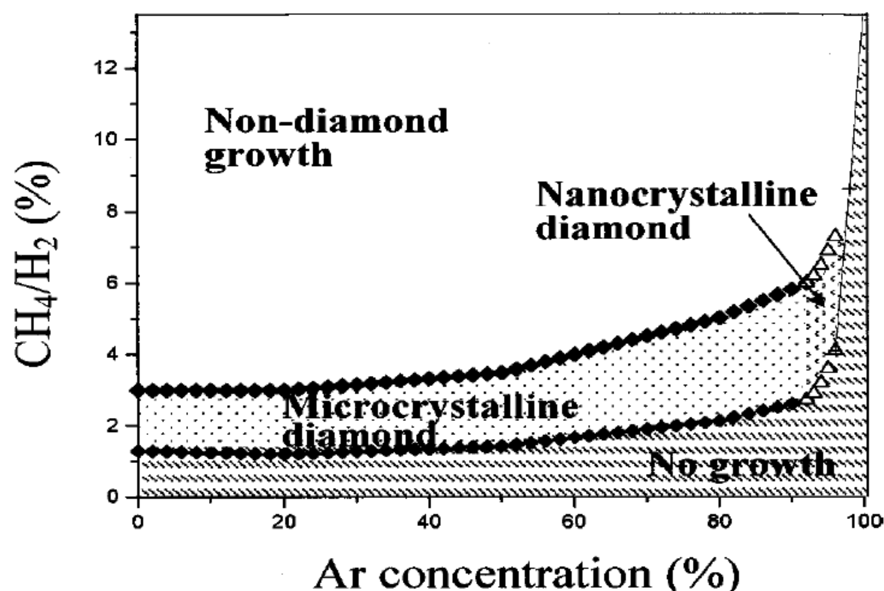

Figure 2.7. Compositional map of the Ar-H_2-CH_4 system for diamond films growth [18].

An explanation to the changes in morphology presented above lays on the dominant growth species and the synthesis path follow by the diamond films for different proportions of Ar/H_2/CH_4 in the growth chemistry [18]. In this regard, using optical emission spectroscopy, Zhou [18] found out that as the ratio of Ar/H_2 is increased in the diamond films growth chemistry, the concentration of C_2 dimers in the growth plasma is increased as well. These results indicate that MCD and NCD films are grown under the presence of atomic hydrogen, following a CH_3 mechanism of growth. On the other hand, the growth mechanism for UNCD films has C_2 dimers as the dominant growth species. Further details about the synthesis of diamond films can be found elsewhere [18, 22, 24, 25].

2.3.3. Properties of UNCD Films. NCD and UNCD films are originally electrical insulators, however under the right conditions they can become conductors if "doped" with electron acceptor or donor chemical elements [25]. In this regard, NCD and UNCD films show two different mechanisms of metallic conductivity [25]. In NCD films, conductivity is usually achieved via boron substitution, leading to p-type conductivity. On the other hand, UNCD films show n-type conductivity obtained by introducing nitrogen into the synthesis gas while reducing the argon concentration [25, 26]. Presence of nitrogen in the synthesis gas is believed to induce the n-type conductivity of UNCD films by favoring the formation of sp^2 bonds between carbon atoms, especially in the materials grain boundaries [25]. A correlation between conductivity of UNCD films and the concentration of nitrogen in the synthesis gas is presented in Figure 2.8.

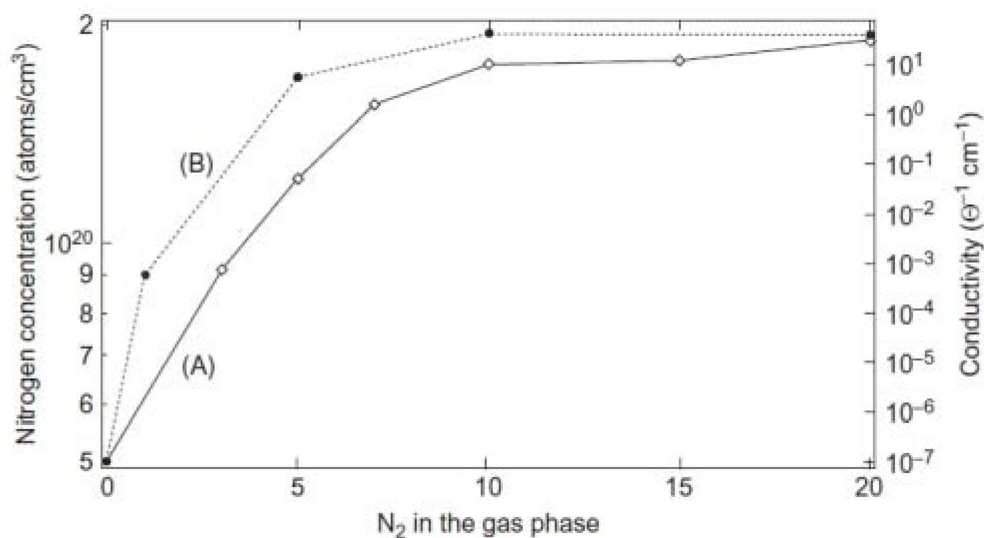

Figure 2.8. Conductivity of UNCD films as a function of nitrogen content in the gas phase [25].

2.4. UNCD FIMLS AS FIELD EMITTERS

As mentioned before, UNCD films are originally insulators. However, as shown in Figure 2.8, the addition of nitrogen into the synthesis gas leads to drastic increase in

the conductivity of these films. This increase in conductivity is associated to a higher amount of sp^2 bonded carbons, especially in the grain boundaries. In fact, nitrogen-incorporated UNCD films are currently the only form of diamond that shows n-type conductivity at ambient temperature [25]. N-UNCD films were first developed at Argonne National Laboratory as a result of the pioneer work of Bhattacharyva, et. al. [26]. This work opened the door to new world of applications with diamond films in which conductivity at room temperature was a key point. One of these new applications, and the most interesting one for the objectives of this work, is the possibility of using N-UNCD as field emitter materials.

Several groups have investigated the FE characteristics of N-UNCDs. Results have shown that these films have unique chemical, electrical and mechanical properties that make them excellent candidates for vacuum microelectronic devices like the field emitter arrays (FEA) developed for this dissertation [17, 27]. A recent study carried out by Getty et. al. as part of a collaboration between NASA and Argonne National Laboratory investigated the FE emission characteristics of several N-UNCD coated microstructures [20]. These microstructures included high aspect ratio silicon tips, silicon bars and planar silicon wafers, as shown in Figure 2.9.

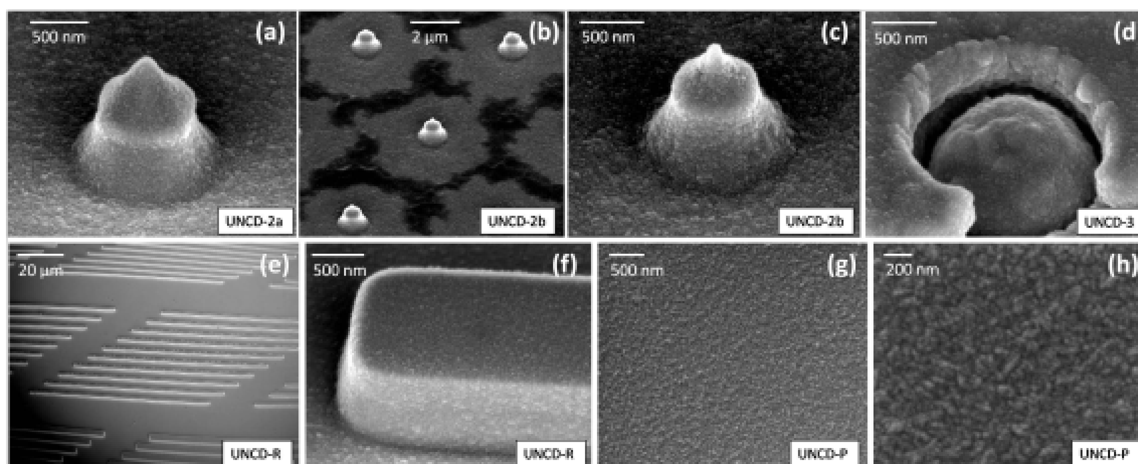

Figure 2.9. SEM images of the samples used for field emission measurements of several N-UNCD coated microstructures. (a) 250 nm tip, (b) and (c) 100 nm tip (d) 500 nm tip, (e) and (f) N-UNCD features on Si ridges, and (g) N-UNCD films grown on a planar silicon substrate [20].

To evaluate their FE characteristics, current-voltage curves measurements were performed for each of the samples shown in Figure 2.9. As shown in Figure 2.10, results indicated that a higher emission current is obtained as the radius of the silicon tip used as substrate is reduced. This behavior was expected and agrees with the FN theory, as a smaller emitter tip radius would yield higher emission currents due to the expected increase in field enhancement (Subsection 2.2). However, results obtained by Getty and collaborators also have shown that N-UNCD coated high aspect ratio silicon tips and N-UNCD coated silicon flats yield similar field emission characteristics, see Figure 2.10.

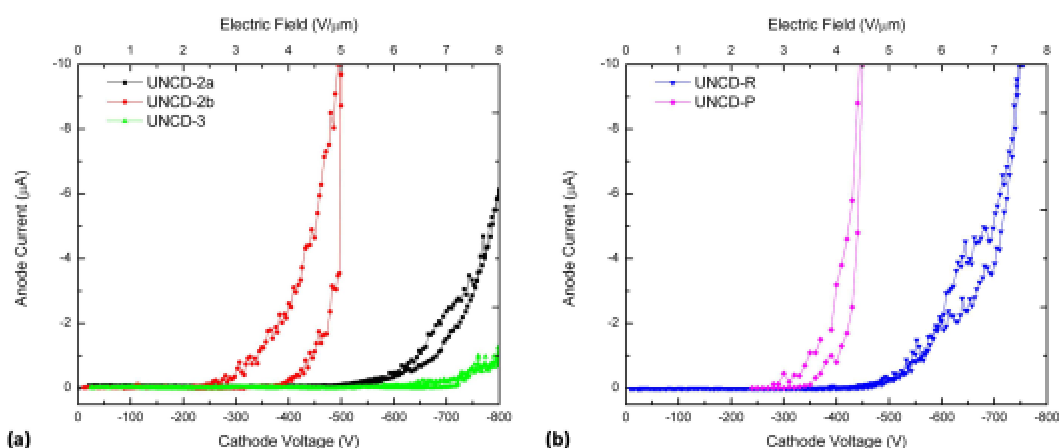

Figure 2.10. Anode current (μA) vs. cathode voltage (V) from N-UNCD on Si substrates with different topographies. (a) 250 nm Si tips (black squares), 100 nm (red circles), and 500 nm (green up triangles); (b) Si microridges (blow triangles) and planar Si substrate (purple diamonds) [20].

These interesting results are believed to be due to the unique microstructure of N-UNCD films [20, 22, 25]. In these films, FE is believed to originate in their interstitial grain boundaries. As mentioned before, the incorporation of nitrogen into UNCD films modify their grain boundary regions. This leads to a higher amount of sp^2 bonded-carbons in the grain boundary regions, favoring the N-UNCDs electron transport properties and consequently, their FE characteristics. For N-UNCD films, emission current densities as high as $15mA/cm^2$ have been reported, with turn-on fields as low as 6

V/μm [8, 20, 25]. These results indicate that N-UNCD planar films are a robust, and an excellent electron emission source, capable of yielding high emission currents at low electric fields. Also, the possibility of working on a flat substrate greatly simplifies the microfabrication process of N-UNCD based electron sources. These characteristics make N-UNCDs the ideal emitter material for the field emitter array developed in this work, and for many other vacuum microelectronics applications.

3. FIELD EMISSION SIMULATIONS

3.1. PARTICLE-IN-CELL CODES

Particle-In-Cell (PIC) codes are commonly used in plasma simulations because of their capacity of simulating densely populated beams of charged particles that interact both among themselves and with externally applied fields [27, 28, 31]. Taking advantage of this proven capacity of PIC codes of simulating beams of charged particles, the commercially available OOPIC Pro code [29, 31] was used to carry out a series of preliminary simulations for the design of the electron source proposed in this paper. OOPIC Pro is a two dimensional PIC code developed to simulate the interaction between plasmas and beams of charged particles with externally generated fields [29-31].

To minimize the computational requirements of the simulations, PIC codes use the concept of macromolecules in the calculations. These macromolecules are the sum of up to 10^6 individual molecules, and each time step they are advanced in space due to the forces generated by both externally applied and self-induced electric fields. For these, the externally applied fields are calculated across a number of spatial cells (grids). In the case of this work, each of the simulated macroparticles represents up to 10^6 individual electrons.

In Figure 3.1 a diagram showing the steps involved in PIC simulations is presented. Initially, the fields for each point in space are defined and distributed among the spatial cells defined by the user. In this same step, the positions and velocities of particles initially present in the system are calculated. Then, the influence of each particle is included into the external field calculated for the cells in which they reside. In this step, the Poisson's Equation, (Eq. (7)), is used to determine the Electric Field as a function of the charge density:

$$\nabla \bullet \vec{E} = \nabla^2 \phi = -\frac{\rho}{\varepsilon_0} \tag{7}$$

Once the initial external fields and charge density are determined, particles are advanced in time using a leap-frog. In this work, an electrostatic model was used, in

which case the forces acting upon each macroparticle as a consequence of the electric field are calculated using the Lorentz Force Equation (Eq. (8)).

$$\vec{F} = m\frac{d\vec{v}}{dt} = q(\vec{E} + \frac{\vec{v}}{c} \times \vec{B}) \tag{8}$$

Once the force acting on each macroparticle is calculated, their new positions and velocities are determined. In this step, the number of particles collected in the boundaries of the system are removed from the calculations and the diagnostics requested by the user are performed. With the new position and velocities of the particles, fields and charge density are calculated again, and the process is repeated [30-32].

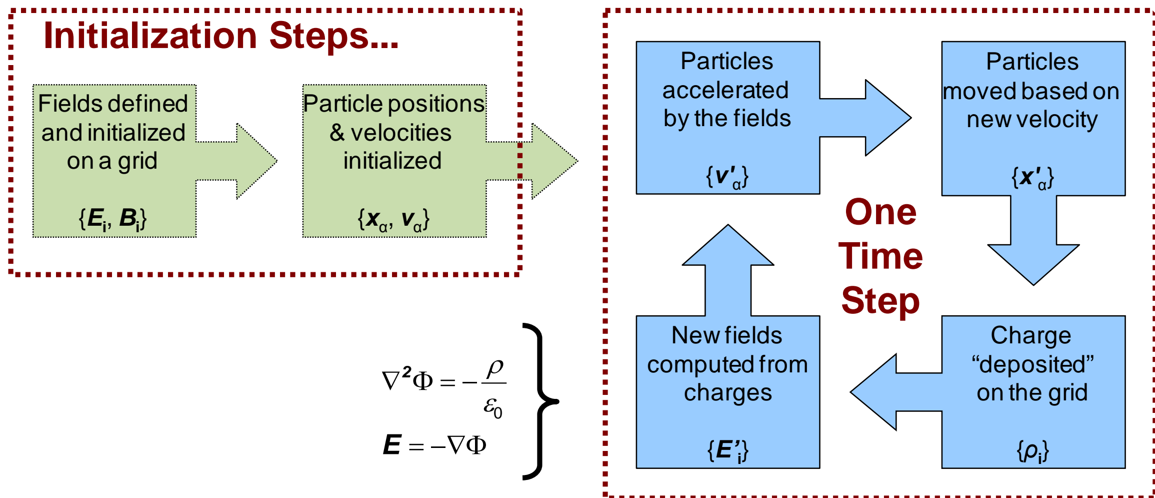

Figure 3.1. Diagram of the PIC algorithm [33].

3.2. SIMULATION PROCEDURES

To evaluate the expected FE emission characteristics of a first design for the FEA prototype developed in this work, a series of simulations were performed. This section summarizes the simulation procedures and preliminary results obtained from those simulations. For the simulations, the triode structure presented in Figure 3.2 was modeled using OOPIC PRO [29]. This triode structure has three basic components: the cathode,

the extraction grid and the anode. The walls of the cell are simulated as insulators. In addition, focusing lenses were added to the triode structure to determine their effect on the electron trajectories. The emitters' layer was simulated as a layer of FN emitters located on the cathode. This layer of emitters was set to be centered and to cover 50% of the total surface of the cathode.

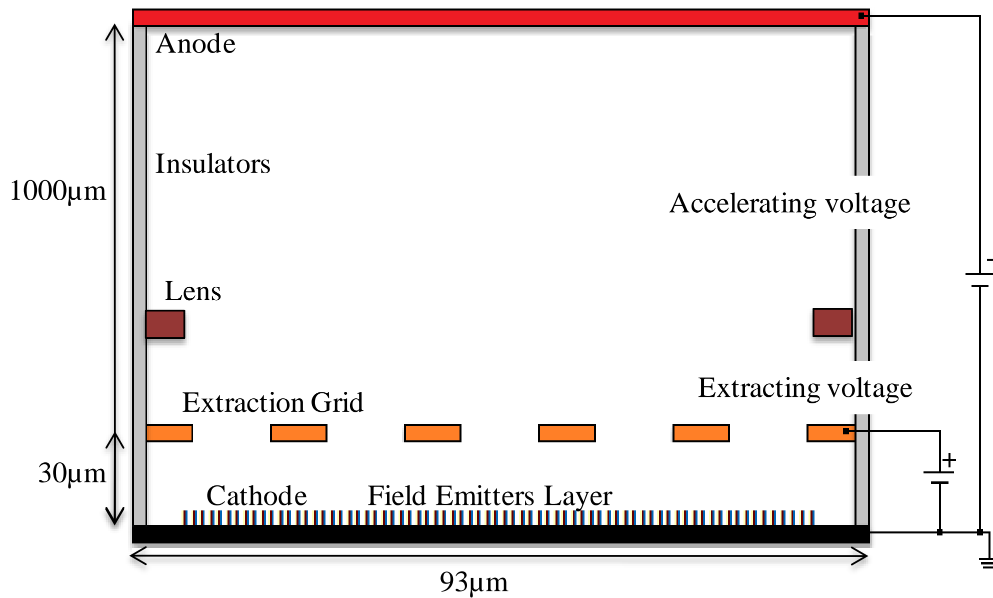

Figure 3.2. Triode structure used for the field emission simulations.

The FN parameters used in the simulations are summarized in Table 3.1. At this stage of the project, the field emitter materials to be used in the fabrication of the prototype had not been selected yet. Therefore, the simulations were performed with parameters that were according to results reported in the literature for carbon based-field emission systems; specifically for CNT-based cold cathode systems [34-37].

Table 3.1. FN parameters used in initial OOPIC Pro simulations.

FN Parameters	Value
Work Function (eV) Φ_w	5
Field Enhancement β_{FN}	2200
A_{FN}	1.5415 x 10^{-6}
B_{FN}	6.830 x 10^{9}
Cv	0
Cy	3.79 x 10^{-5}

The components of the triode structure shown in Figure 3.2 are defined in OOPIC Pro as boundary surfaces (surfaces where particles are collected). The types of boundary surfaces used to represent each component have been selected according to their expected electrical properties. Thus, cathode, extraction grid, anode and focusing lens are defined as equipotential boundary surfaces. In OOPIC Pro, equipotential surfaces behave as perfect conductors grounded at a specific potential, this potential can be fixed or defined as a function of time [29]. The insulators or walls of the triode structure were simulated as dielectric boundary surfaces. The accumulation of charges due to electrons striking the surface of the dielectric surfaces is taken into account in the OOPIC Pro model [29]. Emission of electrons from the CNT emitters located at the cathode was modeled according to the FN mechanism discussed before (see Eq. (1)) [4]. The FN mechanism is an OOPIC Pro built-in function, which is called by incorporating the "FowlerNordheimEmitter" block in the input file (See Appendix A) [29].

A screenshot of the actual geometry modeled in OOPIC Pro is shown in Figure 3.3, in which the x-y phase space output of one of the simulations run in OOPIC Pro is seen. The components of the simulated triode structure are indicated in Figure 3.3. In this figure, emitted electrons are seen as a sequence of dots next to the surface of the cathode.

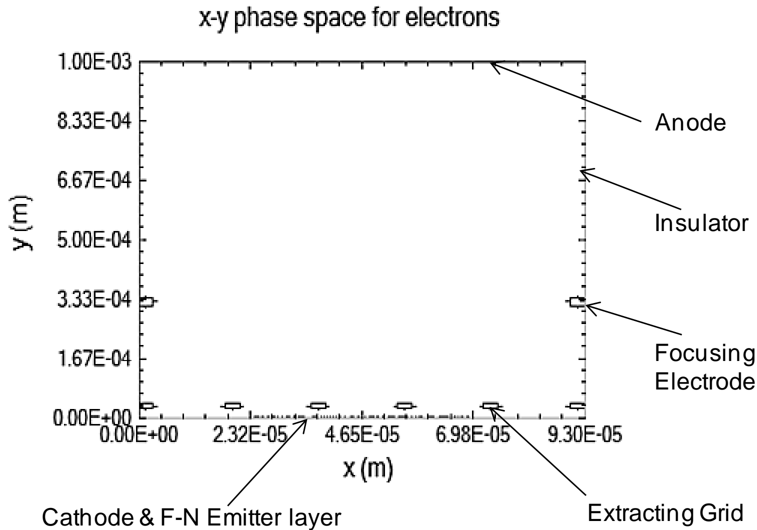

Figure 3.3. Screenshot of actual geometry modeled in OOPIC Pro.

For operation of the electron source, a low voltage bias (20-70 V) is applied to the extraction grid (*extracting voltage*) to extract electrons from the emitters. The emitted electrons are accelerated toward the anode using a high voltage bias (30 -120 kV) applied between the cathode-anode gap (*accelerating voltage*); see Figure 3.2.

A pixel size of 100 by 100 µm was originally considered design. This pixel size corresponds to the width and depth of each of the micro X-ray cells. Taking into account this proposed pixel size and due to geometrical limitations of the code implemented in OOPIC Pro, the pixel size (width) selected for the simulations is 93 µm. Since OOPIC Pro is a two dimensional code, the third dimension cannot be defined in the input file. However, for the calculations, OOPIC Pro assumes the third dimension to be equal to 1 m (z = 1 m). The electric and geometric parameters used in the OOPIC Pro simulations are presented in Table 3.2.

Table 3.2. Geometric and electric parameters used for the OOPIC Pro simulations.

Parameter	Value
Cell width	93 µm
Cathode to Anode Distance	1000 µm
Cathode to Grid distance	25 µm
Grid Aperture	15 µm
Grid Width	3 µm
Grid Thickness	12.5 µm
Cathode Voltage	0 V – (Ground)
Grid (Extracting) Voltage	20 - 70V
Anode (Accelerating) Voltage	30, 40, 60, 80, 100 and 120 kV
Focusing lens Voltage	4kV (30kV Case) and 14kV (120kV Case)

As a starting point, the geometric characteristics of the extraction grid were selected according to the dimensions of commercially available transmission electron microscopy (TEM) grids. These commercially available TEM grids were initially considered to be used for the constructions of a first prototype of the proposed FEA. A diagram with the geometric characteristics of the extraction grid is presented in Figure 3.4.

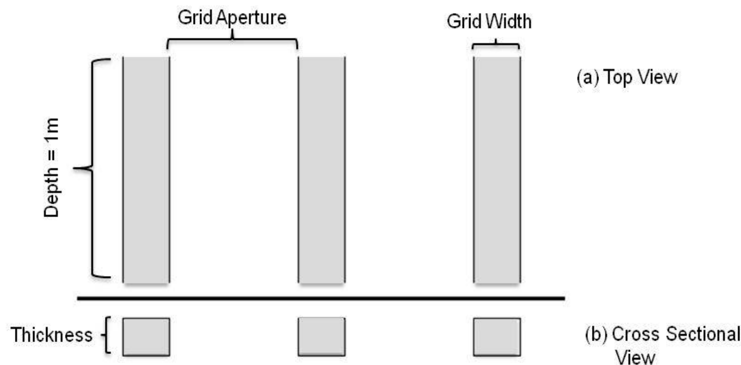

Figure 3.4. Dimensions defined for the extraction grid in the PIC 2D simulation. Diagram not to scale.

In Particle-In-Cell (PIC) simulations, defining the right spatial and temporal resolution is important to guarantee the stability of the code and the accuracy of the results. Due to the characteristics of the PIC algorithm, it is required to guarantee that particles will not advance more than one cell per time step. However, cells and time steps must be small enough so that sufficient details are revealed by the OOPIC Pro simulations with errors as small as possible [30]. In the preliminary simulations here presented, 31 and 80 cells were used in the x- and y-directions respectively. It gives us a spatial resolution equal to $dx = 3\mu m / cell$ and $dy = 12.5\mu m / cell$. Regarding the temporal resolution, the time step (t_{step}) has been defined as:

$$t_{step} = 0.5 * dy / c = 2.084 \times 10^{-14} s \quad (9)$$

In this equation, c corresponds to the speed of light (c = 2.99×10^{8} m/s). This condition establishes that any particle going as fast as the speed of light will travel only half of the distance *dy*, with *dy* being defined as the spatial resolution in the *y-direction*. In order to guarantee convergence and stability of the PIC algorithm, the denominated Courant-Lewly stability criterion needs to be satisfied. For the simulations presented in this work, the electrostatic solver has been selected; and the Courant-Lewly Criterion was guaranteed, such that particles will not jump more than one cell per time step [30]. For further details, the OOPIC Pro input file used in the simulations can be found in the Appendix A. Additionally, in the proposed design transmitted X-rays are generated by Bremsstrahlung interactions between high energy electrons and a target material located at the anode. The Monte Carlo code MCNPX has been used to evaluate the X-ray generation characteristics of the proposed structure. Results of the MCNPX simulations of the X-ray generation characteristics of the proposed structure are reported elsewhere [7].

3.3. PRELIMINARY OOPIC PRO SIMULATION RESULTS

3.3.1. Total Number of Particle and Convergence. The total number of particles at a given time was determined for each of the simulations. These results for the total number of particles in the system were used as the main convergence criteria. According to the model implemented, the layer of emitters located at the cathode is the only source of electrons in the system. In consequence, no accumulation of particles or total energy can occur in the system during steady state. Figure 3.5 shows a typical behavior for the total number of particles in the system as a function of time. The dc voltage applied to the extraction grid (20 – 70 V) is considered to have a rise time equal to 10 ps. Therefore, no emitted electrons are initially present in the system and the number of particle remains close to zero during the first $1x10^{-11}$ s. Around $1x10^{-11}$ s, the grid voltage is high enough for the emission of electrons to occur and the number of particles in the system starts increasing rapidly until it reaches a maximum. The time at which the number of particles in the system peaks indicates the time required for the first emitted electrons to reach the anode surface.

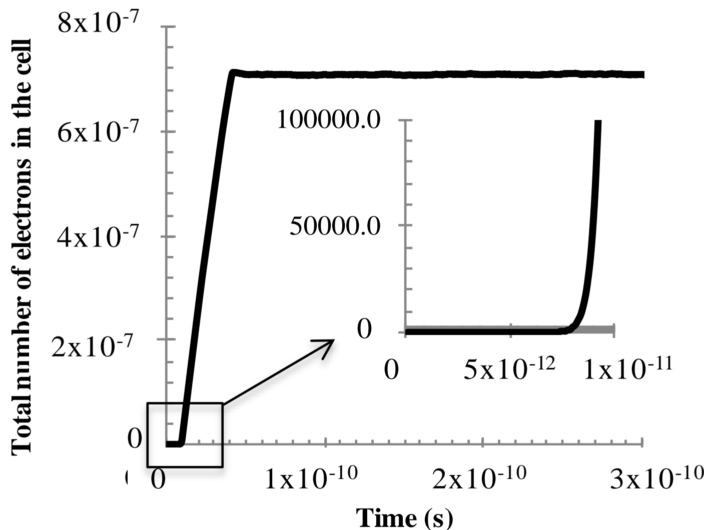

Figure. 3.5. Total number of emitted electrons in the triode structure as a function of time. Grid voltage: 42 V, anode voltage: 30 kV, no focusing.

In the case presented in Figure 3.5, the maximum number of particles is reached around 4.2 $x10^{-11}$ s. After the number of particles reaches its maximum, it remains fairly constant over time at a value around $7x10^{7}$ electrons. It indicates that equilibrium between the number of electrons being emitted at the cathode and the number of electrons leaving the system through the surfaces of the triode structure is established.

This constant value in the number of particles reaching the anode at a given time will determine the current density of electrons at the anode for steady state operation. If no convergence is reached in the simulations, the total number of particles in the system will continue growing without reaching a maximum point. This behavior will indicate the presence of non-physical phenomena in the simulations.

3.3.2. Electron Trajectories. Following the determination of the convergence, the trajectories of the emitted electrons were determined with and without focusing lenses being included in the triode structure. Typical results are presented in Figures 3.6 and 3.7. As shown in Figure 3.6-(a), no particles are initially present in the system.

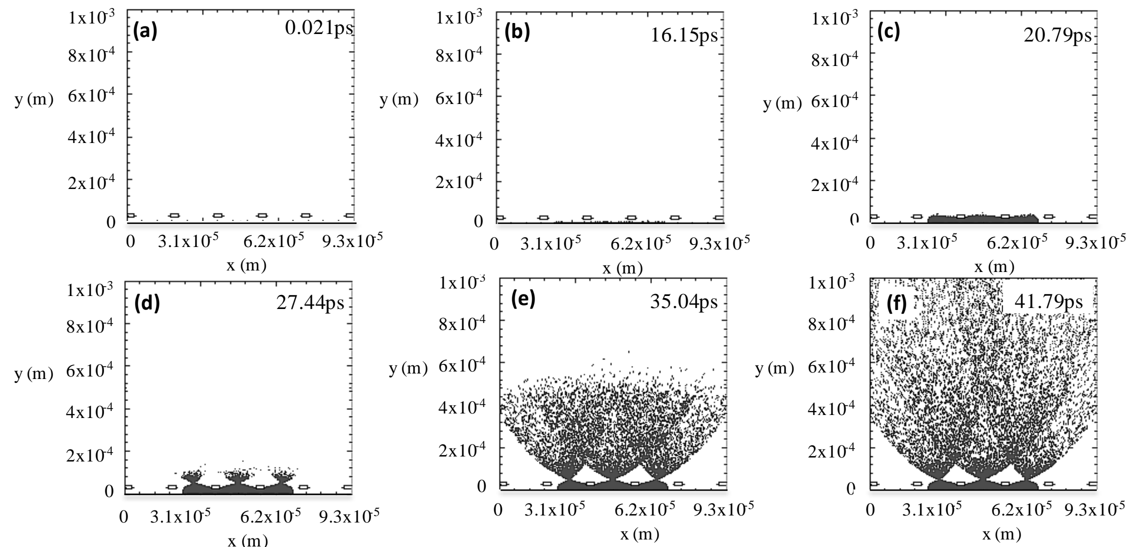

Figure 3.6. Trajectory of the electron beam when no focusing lenses are used. Grid voltage: 45 V, anode voltage: 30kV, no focusing.

As time goes on, the emission of electrons due to the electric field generated between the cathode-grid gap begins (Figure 3.6-(b)). In the vicinities of the extraction

grid, the trajectory of emitted electrons follows a convergent trajectory such that a crossover of the beam of emitted electrons is eventually observed (Figure. 3.6-(c) and -(d)). This crossover in the trajectory of the emitted electrons is associated to a distortion of the electric field lines in the surroundings of the extraction grid.

This convergent behavior observed for beams of field emitted electrons in triode structures has been reported before by D. M. Garner [38]. In his work, Garner modeled a triode structure and determined the trajectory of electrons using a Runge-Kutta algorithm. In agreement with the results presented in this work, Garner found the crossover of the electron beam to be associated with the distortion of the electric field around the edges of the extraction grid. This distortion is also associated to a self-focusing effect observed for electron beams accelerated at high voltages [38].

After passing the "crossover" region, electrons acquire a divergent trajectory (see Figure 3.6-(e)) which is kept until they reach any of the surfaces of the triode structure (Figure 3.6-(f)). Due to this divergent trajectory, some of the emitted electrons do not reach the surface of the anode and are collected on the walls of the triode structure instead. This will lead to accumulation of charges in the walls of the triode structure and large focal spot sizes.

The use of focusing structures was analyzed as an alternative to mitigate these potentially negative effects on the operation of the electron source. Results are presented in Figures 3.7-(a) through -(f). As seen in these figures, the initial trajectory of the electron beam, when a focusing voltage is applied, is similar to the trajectory of the electron beam obtained when no focusing is used (Figures 3.6 -(a) through -(d)). However, the presence of focusing electrodes changes the electron path from a divergent trajectory to a convergent one (Figures 3.7-(e) and -(f)). It indicates that using focusing electrodes both the accumulation of charges in the walls of the triode structure and the focal spot size of the electron beam can be effectively controlled.

The change in electron trajectories when focusing lens are present in the simulations is also associated to distortions in the electric field lines in the vicinities of the focusing lenses. More details can are reported elsewhere [39].

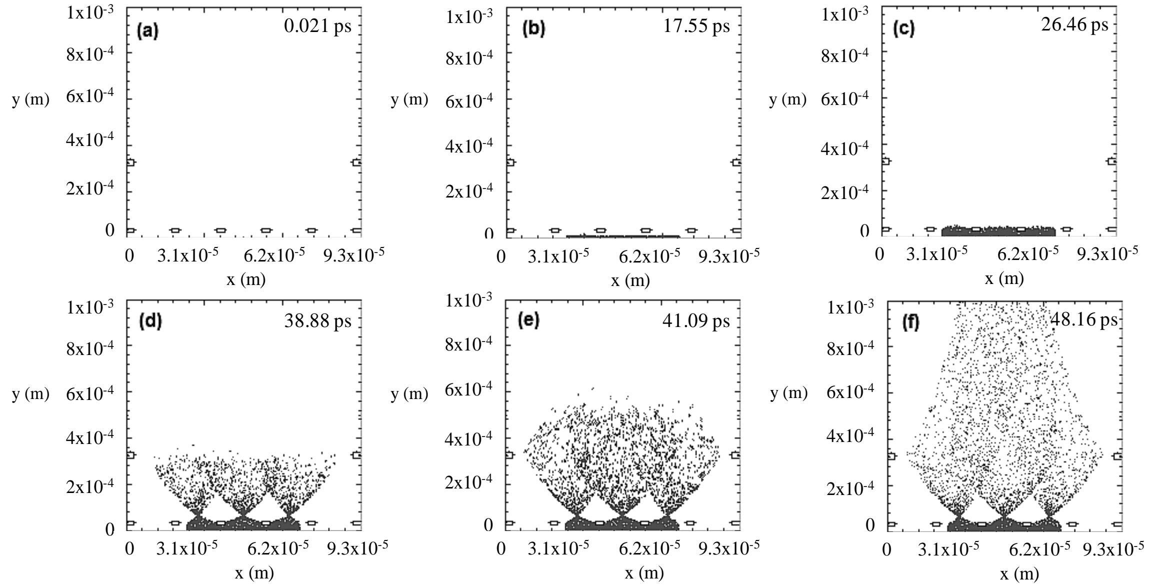

Figure 3.7. Trajectory of the electron beam when focusing lenses are used. Grid voltage: 45 V, anode voltage: 30 kV, focusing voltage: 4 kV.

3.3.3. Current Density as a Function of Extracting Voltage (J_{FN}-V curves). Two important variables in the design and operation of X-ray sources are the number and the energy distribution of X-rays being produced at the anode at any given time [1]. These two variables are associated with the number and energy distribution of the high energy electrons striking the anode. In this subsection, results including the current density (mA/mm^2) and energy distribution of electrons striking the anode at a given time are presented as a function of grid and anode voltages. Results obtained for the current density are summarized in Figure 3.8, where the J_{FN}-V curves of the simulated structure are presented. These J_{FN}-V curves correlate the electron current density at the anode with the grid voltage. A J_{FN}-V curve was built for each of the anode voltages listed in Table 3.2. Results indicate that the electron current density at the anode increases rapidly as the grid voltage is increased (see Figure 3.8). This "exponential" behavior of the current density with respect to the grid voltage is characteristic of FN emitters. This behavior can be explained by the exponential component of the FN equation used to model the emission of electrons from the field emitters (Eq. (1)). Furthermore, results presented in Figure 3.8 indicate the existence of a grid voltage below which no detectable FE of electrons will occur; this voltage is denominated turn-on voltage. For the 120 kV anode

voltage case the turn-on voltage was found to be as low as 28.5 V, whereas for the 30 kV anode voltage case, the turn-on voltage was found to be around 40 V. Results presented in Figure 3.8 also indicate that the electron current density is mostly controlled via grid voltage; a similar result is reported for other FE based triode structures [34]. This control of the emission current via grid voltage needs to be guaranteed in order to allow the proposed flat panel X-ray source to be operated in scanning mode in a fast and accurate way. Control via grid voltage allows the emission of electrons/generation of X-rays from each micro X-ray cell to be controlled independently. The grid control mechanism has been tested and proved by other research groups currently attempting to use this type of cold cathode technology on the generation of X-rays [34, 36, 37, 40, 41]. These research groups are also attempting to develop a flat panel X-ray source, although results are reported mostly for reflection-rays, no transmission X-rays.

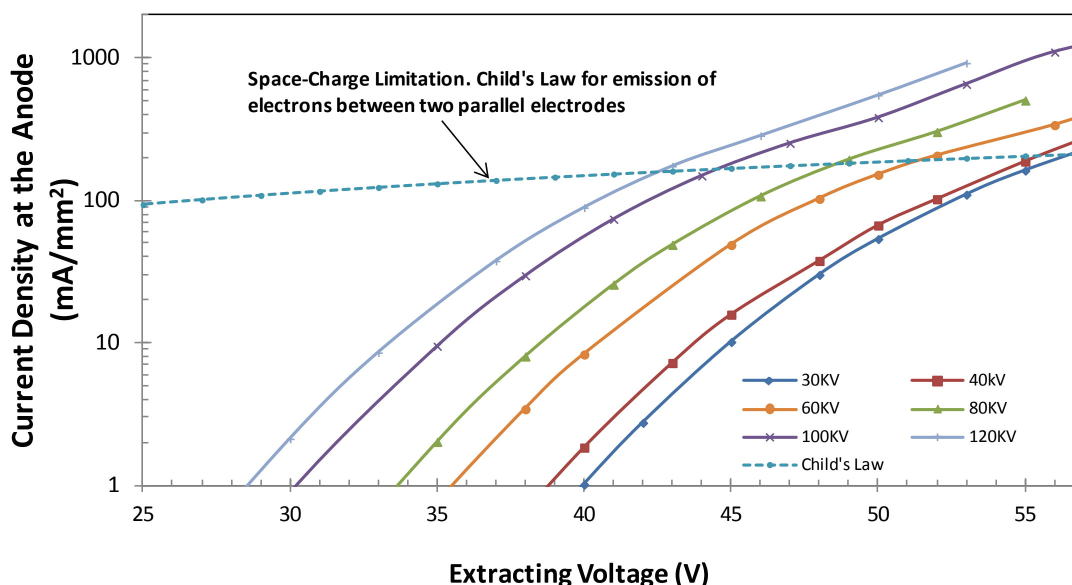

Figure 3.8. J_{FN}-V curves – Anode current density (mA/mm^2) as a function of the grid voltage at different anode voltages. No focusing electrodes present in the triode structure.

3.3.4. Space-Charge Effects. Results of the emission current density as a function of grid voltages indicated the existence of a grid voltage at which the emission of electrons goes from a continuous process to an oscillatory one, see Figure 3.9. This transitional grid voltage is associated with charge limitation effects related to Child-Langmuir's law [42]. The Child-Langmuir's law establishes that for two parallel plate electrodes, there is a point at which the number of charges is so high that their electric field will equal the externally generated electric field, reflecting new emitted charges and creating a virtual cathode [42]. The transition from a continuous to an oscillatory emission of electrons is seen in Figure 3.9-(a) through -(d). As shown in Figure 3.9-(a), at low extracting voltages (30 V) the current density is low enough such that no space charge effects are induced. However, as the extracting voltage is increased, the number of electrons in the system increases as well. The presence of a higher number of electrons increases the magnitude of the fields induced by the electrons. As a consequence, the effective magnitude of the externally applied electric field at the cathode surface diminishes. Therefore, a smaller number of electrons are emitted. This effect is seen in Figure 3.9-(b), where the value at which the current density stabilizes is lower than the maximum value of the current density obtained in the initial stages of simulations, where no space charge effects where present in the system. Further increasing the magnitude of the grid voltage leads to an oscillatory emission of electrons (Figures 3.9–(c) and –(d)). These oscillations are explained by the time dependent nature of the space charge effects. Following the reduction of the electric field at the cathode surface, the number of emitted electrons is lowered as well; therefore, decreasing the magnitude of the space charge effects. As a result, more particles can be emitted [27, 28, 43, 44]. This cycle gets repeated numerous times, leading the system to operate in oscillatory mode as indicated in Figure 3.9-(d).

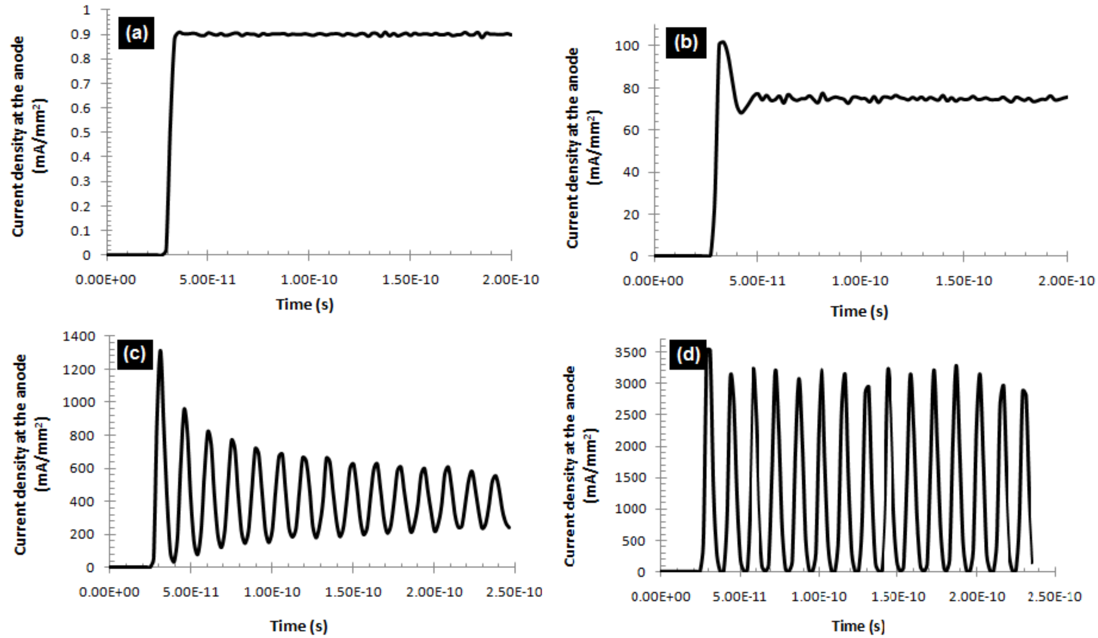

Figure 3.9. Current density at the anode as a function of time, no focusing lenses are used. Transition from FN to space charged limited emission. Anode voltage: 100 kV; grid voltage (a) 30 V, (b) 41 V, (c) 50 V and (d) 56 V.

Results presented in Figure 3.9 are in agreement with results presented in Figure 3.8, where Child-Langmuir's law is plotted and is seen as a fairly horizontal line (note the logarithmic scale used for the y-axis). In Figure 3.8, for a 100 kV anode voltage case, the Child-Langmuir's plot indicates that the space-charge limitation phenomena will become significant at grid voltages above 44 V.

Depending on the anode voltage, the space-charge limitation was found to become significant for simulations with at grid voltage between 43 and 58 V. This is a benchmark for the simulated model. In general, lower the anode voltage, the higher the grid voltage will need to be for space-charge limitation effects to become significant. The trajectory of electrons for systems featuring continuous and oscillatory emission of electrons is presented in Figures 3.10–(a) and –(b), respectively.

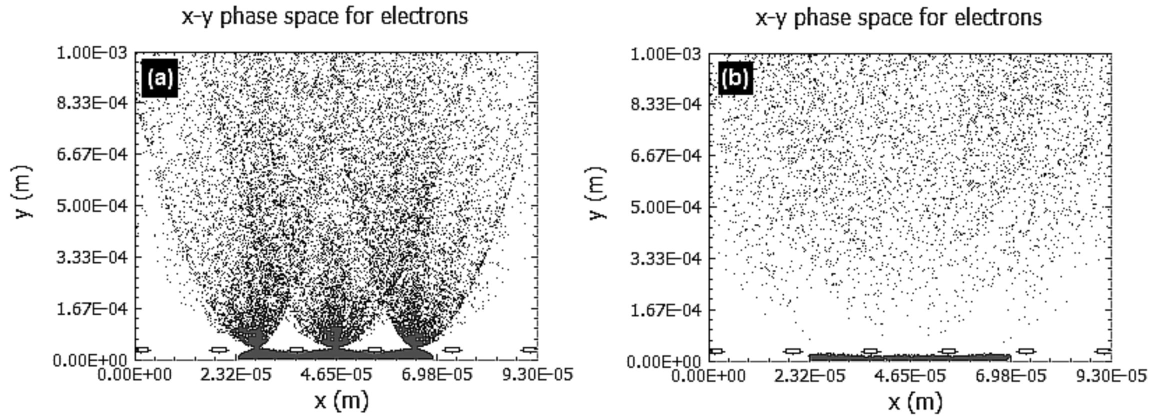

Figure 3.10. Electron trajectory in the triode structure. Anode voltage: 100kV, (a) grid voltage: 35V - continuous emission of electrons, (b) grid voltage: 55V - oscillatory emission of electrons.

3.3.5. Energy Distribution of Electrons at the Anode. In order to evaluate the field electron emission characteristics of the proposed electron source, the electron trajectories have been presented above for different simulation conditions. Furthermore, the number of electrons striking the target has been evaluated in terms of the current density of electrons at the anode surface for a given time. In this subsection, attention will be focused on the energy distribution of electrons reaching the anode.

A comparison between results obtained with and without focusing lenses being included in the triode structure. Figure 3.11 shows the results obtained for an anode voltage of 120 kV and a grid voltage of 40 kV. In Figures 3.11-(b) and -(d) a focusing voltage of 14 kV was applied. From the analysis of the electron trajectories, it was established that the beam of emitted electrons has a diverging trajectory when no focusing electrodes are used (see Figure 3.6). As a consequence, electrons reaching the anode are distributed over the whole anode surface, but still over a narrow energy range.

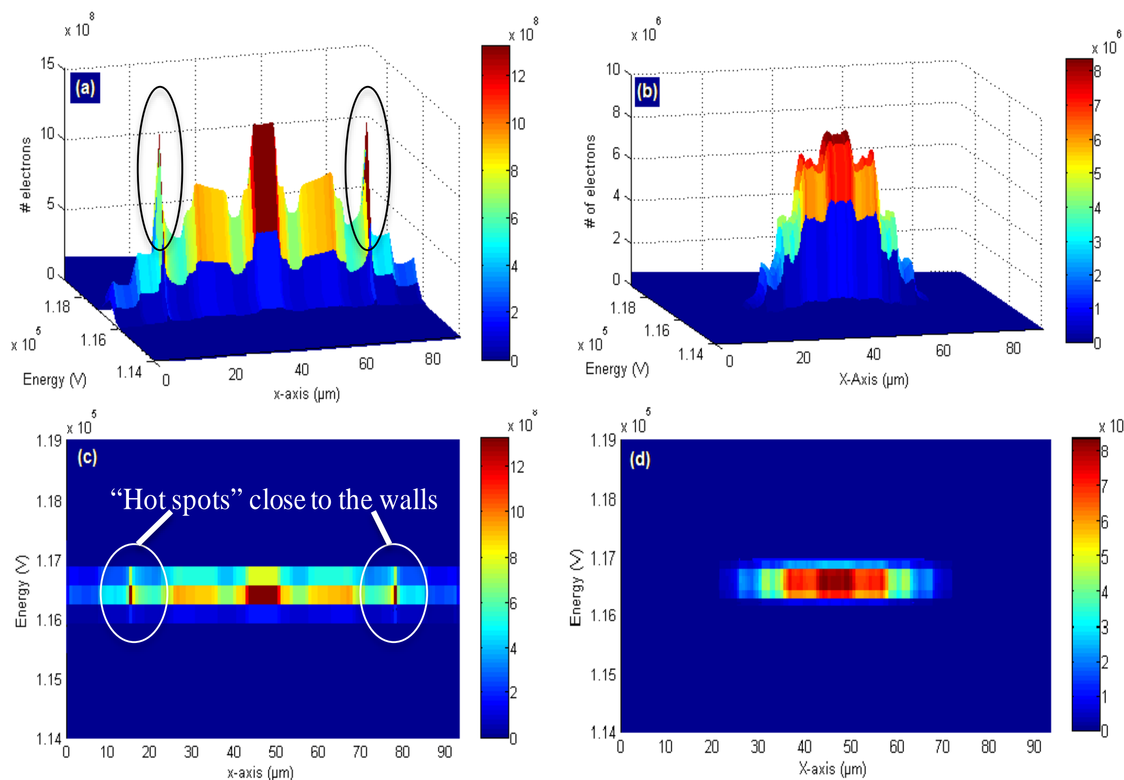

Figure 3.11. Energy distribution of electrons striking the anode. Simulation conditions: Anode voltage:120 kV, (a) grid voltage: 40 V, no focusing, 3-D view, (b) grid voltage: 40 V, focusing voltage: 14 kV, 3-D view, (c) same conditions as (a), top view. (d) same conditions as (b), top view.

Figure 3.11-(a) shows a typical distribution of electrons at the anode. In this figure, the z-axis indicates the number of electrons reaching the anode and the x-axis indicates the position in which the electrons are hitting the anode at a given time. Results show a non-uniform distribution of electrons, and some "hot spots" are observed in the center of the anode surface. In addition, the "hot spots" are approximately 20 µm away from each of the walls of the triode structure. On the other hand, in the cases where focusing electrodes are present in the triode structure, a more uniform distribution of electrons is obtained (Figure 3.11-(b)). In this case, the number of electrons striking the anode reaches its maximum at the center and decreases gradually toward the edges of the anode surface. This behavior of the distribution of electrons is associated to the convergent trajectory acquired by the beam of emitted electrons when it passes through the focusing lens (Figure 3.7). In addition, the thickness of the 3-D plots presented in

Figures 3.11-(a) and-(b) correspond to the energy distribution of electrons reaching the anode. These energy distributions are better illustrated in Figures 3.11-(c) and -(d).In both cases (Figures 3.11-(c) and -(d)), it is seen that the energy of electrons reaching the target is slightly lower than the 120 kV potential applied to accelerate the electrons toward the anode in that particular case.

In the case where no focusing structures were used, electron energy ranged between 116 and 117 kV (See Figure 3.11-(c)). This energy band is spread over the whole anode surface. On the other hand, when focusing structures are employed, electron energy still ranged between 116 and 117 kV, but the energy band is limited to the center of the anode surface, leading to a focal spot size of about 60 μm (See Figure 3.11-(d)).

Following these results and according to the triode configuration used in the simulations, the energy of electrons striking the target is controlled via anode voltage. Under ideal conditions, the final energy of electrons will be equal to the high voltage applied to the anode. However, electrons not only interact with the externally applied electric field, but they also experience Coulomb interactions among themselves.
Due to these multiple interactions experienced by the emitted electrons, their final energy will be lower than the potential applied at the anode. This effect is seen in Figure 3.12, where the average electron energy is plotted as a function of the accelerating voltage. According to this figure, a linear relationship exists between average energy of electrons reaching the anode and the accelerating (anode) voltage. The correlation obtained from Figure 3.12 indicates that the average electron energy is between 2 - 9 % lower than the potential applied at the anode.

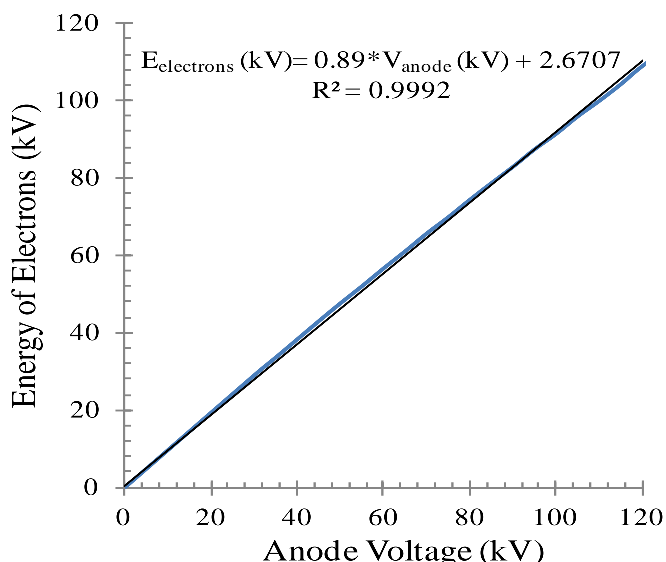

Figure 3.12. Average energy of electrons reaching the anode vs. anode (accelerating) voltage. The grid voltage for these simulations was kept at 45 V.

3.3.6. Focal Spot Size Versus Grid Voltage. Results presented in Figures 3.7 and 3.11 indicate the possibility of using focusing structures to control the focal spot size of the electron beam striking the anode. For instance, as seen in Figures 3.11–(b) and (d) the use of focusing structures leads to a focal spot size of around 60 µm. In this case, the relationship of the focal spot size with the grid voltage is studied for the 30 kV and 120 kV cases; results are shown in Figure 3.13. For the 30 kV case, the focal spot size decreases as the extracting voltage increases, whereas for the 120 kV case, an increase in the focal spot size is observed as the extracting voltage is increased. Using a typical triode structure, Chang et. al.,[35] reported that for a 30 kV anode voltage the focal spot size of the electron beam tends to decrease as the grid voltage is increased. Even though there are differences in the applied grid voltages and the simulated geometries, their results are in general agreement with results presented in this paper. No previous results reporting the behavior of the focal spot size with respect to the grid voltage applied in a triode structure operating at high anode voltages (>100 kV) were found. However, the increasing behavior of the focal spot size with the grid voltage at high anode voltages (>100 kV) is believed to be associated with the difficulty in changing the original trajectory of the electrons due to their higher inertia. In other words, even though the

electrons can be focused, they still tend to keep a proportion of their originally divergent trajectory. This effect is more evident as the extracting voltage is increased due to the higher number of emitted electrons. In addition, as the number of emitted electrons increases, the effect of coulomb interactions will increase as well. However, results obtained from the simulations presented in this work do not appear to be conclusive about the tendency observed for the focal spot size in the 120 kV case. In order to obtain a better understanding of this trend, more sophisticated 3-D PIC simulations will be required.

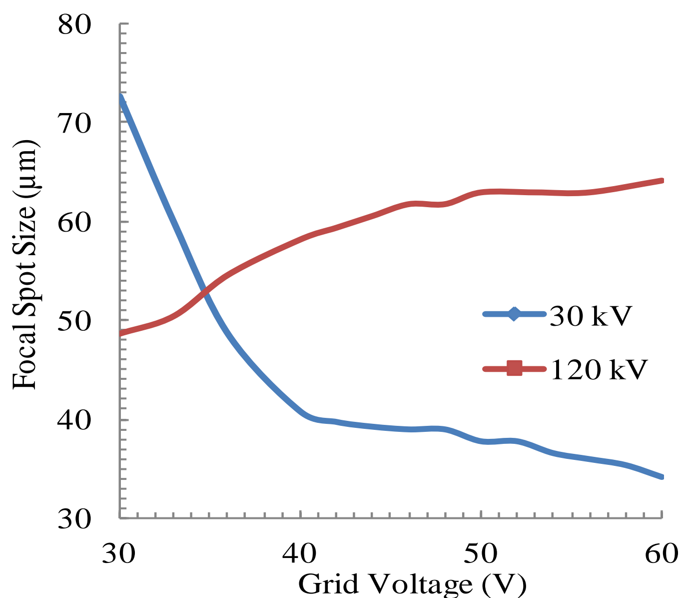

Figure 3.13. Focal spot size as a function of the extracting voltage. 30 kV and 120 kV anode voltage cases.

3.3.7. Conclusions from Preliminary Simulations. Results presented in this subsection indicated the technical feasibility of the proposed FEA to be used as electron source in the Flat-Panel X-ray source. The beam of emitted electrons was found to have a divergent trajectory when no focusing electrodes were employed. The divergent trajectory was modified into a convergent one by presence of focusing structures in the simulated triode structure. The J_{FN}-V curves constructed for the systems indicated that the

electron current density is controlled via grid voltage. A small influence of the anode voltage on the electron current density was observed as well. Space charge limitation effects were found to become important at grid voltages between 43 V and 58 V, depending on the anode voltage. Due to these space charge effects, continuous emission of electrons becomes an oscillatory emission. These results are set the basis for the experimental presented in these next sections, which includes the fabrication, testing and further modification of the FEA prototype simulated in this section.

4. EXPERIEMENTAL SET-UP

4.1. VACUUM SYSTEM CONFIGURATION

In order to perform FE measurements, high vacuum conditions must be guarantee during the experiments. These conditions are important to prevent deterioration of the emitter materials due to molecules that otherwise might present in their vicinities and to minimize the probability of high voltage electrical breakdown. To provide these low pressure conditions, a state-of-the-art high vacuum system was built as part of this work. A diagram of the experimental set-up built for these experiments is presented in Figure 4.1. It consists of a vacuum chamber, equipped with multiple ports for high and low vacuum pumping, as well as for the connection of different types of hardware, such as: pressure gauges, electrical and motion feedthroughs, a residual gas analyzer and other components.

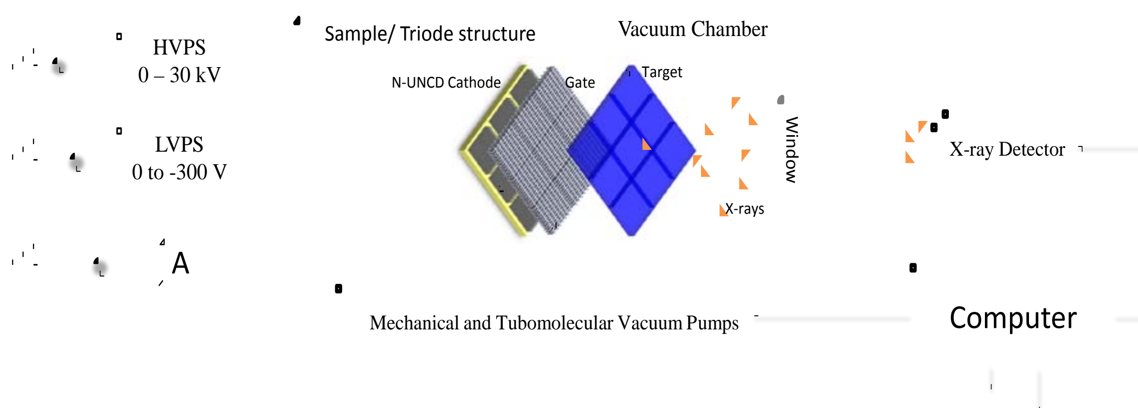

Figure 4.1. Overview of the vacuum system used for the experiments. Components not to scale.

During the experiments, the system can reach and maintain a pressure as low as 3×10^{-9} Torr. Special high voltage feedthroughs allow X-ray generation experiments to be performed at voltages as high as 70 kV. Several low voltage feedthroughs are available for electrical connections inside the chamber. The chamber is equipped with an ultra high vacuum compatible 0.13 mm thick Be window that can be used for the X-ray

experiments. The power supplies and detectors of the system are all connected to a central computer allowing the experiments to be carried out remotely. The following are the main components and specific details of the vacuum system built:

4.1.1. Vacuum Chamber. For the experiments, a 12" spherical 304 stainless steel vacuum chamber was used. It has four 8" CF ports, two 6" CF ports, four 2.75" CF ports, and one 4.5" CF port. For better vacuum conditions, these ports are all fitted to the other components using copper gaskets, thus the chamber could be baked at temperatures up to 400 °C.As shown in Figure 4.2, the chamber is mounted on an extruded aluminum upright-style frame, which can also be used to easily move the system around the laboratory to meet the specific needs of the experiments. An 8" load-lock door is used for easy loading and unloading of the samples, it also serves as additional glass viewport.

Figure 4.2. Vacuum chamber and Al upright style frame.

4.1.2. Electrical Feedthroughs. For the X-ray generation experiments, high voltages should be applied to an anode/target material placed within the system. To meet this requirement in a safely manner, a high voltage electrical feedthrough was placed in the 4.5" CF port. This feedthrough can withstand up to 60 kV and 3 A. For details, see white element at the top of the chamber in Figure 4.2. Additionally, voltages up to 5 kV can be provided to the system through feedthroughs connected to other ports of the chamber. Commercial or custom-made vacuum compatible components are always used for the electrical connections inside the chamber. For better vacuum behavior, oxygen-free high thermal conductivity (OFHC) copper wires are used for the connections between the components and the system's feedthroughs.

4.1.3. Vacuum Pumps and Gauges. Following conventional practices, the high voltage conditions required for the experiments are reached in two steps. In the first step, a rotary vane mechanical pump is used to take the system's pressure down to 10^{-3} Torr. Once the system reaches this base pressure, a 280 L/s Varian turbo pump is used to take the system to high vacuum conditions. Under normal conditions, vacuum conditions in the order of $3x10^{-9}$ Torr can be reached within 24 hours of pumping. A convention gauge with integrated controllers is used to monitor the pressure between 760 and 10^{-3} Torr. For pressures below 10^{-3} Torr, a hot ionization, dual filament gauge with built in controller and display is employed. A Stanford Research Systems residual gas analyzer, RGA200, is coupled to the system for monitoring the gas composition inside the chamber in real-time. This RGA200 is used both, to monitor the gas composition inside the chamber during the baking of the system and to check for leaks using its He leak detector built-in function.

4.1.4. DC Power Supplies. To test the FE and X-ray generation characteristics of the N-UNCD FEA prototype presented in this document, two main power supplies (PS) are required. A Matsusada R4K-80H DC PS is used to provide the gate voltages required for the emission of electrons. This precision PS can deliver voltages between 0 and 320 V with output currents ranging between 0 and 0.5A. It has a voltage ripple of 20mVrms and digital control of it via USB has been enabled through a CO-U32m USB hub. Also, to provide the high voltages required to accelerate the electrons towards the anode, a Matsusada Precision AU120P10 PS is used. It can deliver voltages between 0 and 120 kV

and currents in the range of 0 to 10 mA. It can also be control via USB using a CO-U32m digital controller. For additional testing, such as an eventual evaluation of the focusing characteristics of a second gate in the FEA prototype, two additional power supplies are available. They are a Matsusada AU-5-12 power supply, which is used when voltages between 0 and 5kV are required, and a Matsusada Precision RG-650-0.1 PS used for experiments that require voltages between 0 and 650 V. The output of these power supplies can also be remotely controlled via USB when connected to a central computer using a CO-U32m USB hub. For the FE experiments, the gate and anode currents are measured using the dropping resistor method. For these measurements, the respective current is passed through a 10 MΩ resistor and the resulting voltage drop is measured using a Fluke 289 digital multimeter.

4.1.5. X-Ray Detection System. To evaluate the X-ray generation characteristics of the N-UNCD based Flat-Panel X-ray source, a custom X-ray detection station was built. This station was designed to be easily coupled to the X-ray system, such that the X-rays going through any of the two viewports can be measured. For X-ray characterization, the station houses an X-ray detector, a Canberra Lynx system, and X-ray angular collimation devices. The generated X-rays are then counted and characterized with a low energy (> 3 keV) Ortec GLP series X-ray detector. A Canberra Lynx system that acts as a web server for remote access is used as digital signal processing module. This Lynx system also acts as a built-in single channel analyzer (SCA) and multichannel analyzer (MCA) up to 32K channels. The X-ray detection station allows the detector to be moved up and down to be positioned in plane with the spot where X-rays are produced. Additionally, the detector can be swept over a large angle to determine the angular distribution of the X-ray output.

An image of the actual experimental set-up is presented in Figure 4.3. The Ortec X-ray detector located seen in the left of Figure 4.3 is placed in front of the 8” glass viewport. Before any X-ray measurements were performed, an X-ray energy calibration was completed using a Cd-109 source. This Cd-109 source emits three X-rays (22 keV, 25 keV and 88 keV), this characteristics makes it an useful source for low energy calibrations.

Figure 4.3. Experimental Apparatus. Left: Ortec X-ray detector placed in front of glass view port for X-ray measurements. Right. Vacuum system with the high and low voltage power supplies connected to it.

4.2. TESTING OF EXPERIMENTAL SET-UP

To check for the correct operation of the experimental set-up described in the previous subsection, FE and X-ray generation experiments were performed using a commercial electron source, shown in Figure 4.4. A carbon nanotube (CNT) based FE electron source purchased from HeatWave Labs was used for these measurements. This source is arranged in a diode configuration, in which a metallic grid of 3 mm in diameter is used to extract the electrons from a layer of field emitters placed on a conductive cathode (Figure 4.4-(a)). For the experiments, voltages between 0 to 1200 V were applied to the extraction gate. The experiments were conducted at pressures below $2x10^{-8}$ Torr. In seen in Figure 4.4, the source was placed on a Teflon table for electrical insulation. As seen in Figures 4.4-(b) and (c), a Teflon holder was used to maintain the source in place inside the vacuum chamber. This Teflon holder was also used to place a luminescent screen in front of the source, Figures 4.4 (d) and (e). This luminescent screen is made of a 25mm x 25 mm conductive ITO (Indium tin oxide) coated glass covered by a layer of phosphor scintillator powder P-47. This luminescent screen is excited by emitted electrons striking the screen; therefore photons in the form of blue light are emitted. Consequently, this luminescent screen can be used to determine the shape and position of the focal spot where electrons strike the target (See Figure 4.4-(f)). Also, a Teflon table is used to electrically insulate the electron source from the other components in the vacuum

chamber. This is made to minimize the probability of electrical breakdown inside the chamber, especially when high voltages are applied.

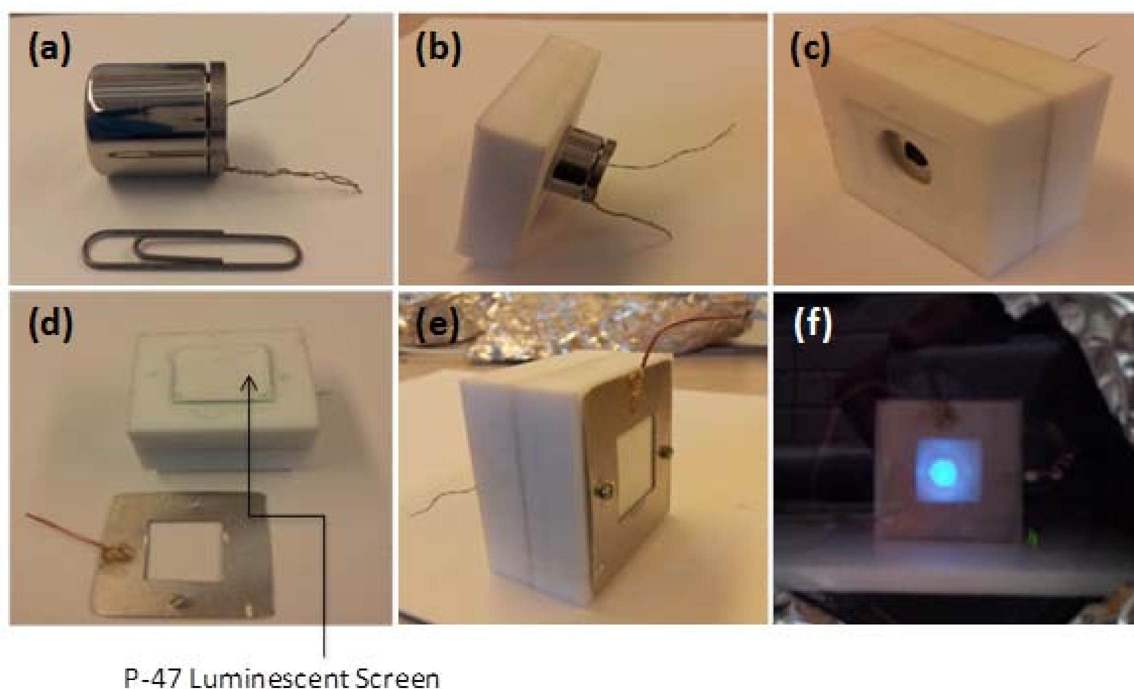

Figure 4.4. CNT-based electron source used for testing the experimental set-up. (a) Electron source. (b) and (c) Teflon holder used to put the chamber inside the vacuum system. (d) and (e) P47 luminescent screen and (f) blue light generated inside the vacuum chamber due to electrons striking the P-47 luminescent screen.

4.2.1. Field Emission Characteristics. The current-voltage (I-V) behavior of the CNT-based electrons source was evaluated by the dropping resistor method described in subsection 4.1. For the experiments, the gate voltage was varied between 0 and 1600 V; at each gate voltage the respective emission current was recorded. Results are presented in Figure 4.5. It is observed that the emission current follows an exponential trend with respect to the gate voltage. This behavior is in agreement with the Fowler-Nordheim theory for FE presented in Section 2, see Eq. (1). In general, emission currents in the order of tens of microamps were measured. This emission was coming from a cathode of 3 mm in diameter covered by the CNTs. This indicates that emission current

in the order of 0.1 to 0.5 mA/cm^2 were obtained. Additionally, the focal spot where the electron beam strikes the target was observed to be about 6mm in diameter. These results indicate that the vacuum system build was well suited for performing FE measurements and could be used for testing the N-UNCD FEA prototype. Furthermore, anode currents in the order of a few nA were measured during these experiments.

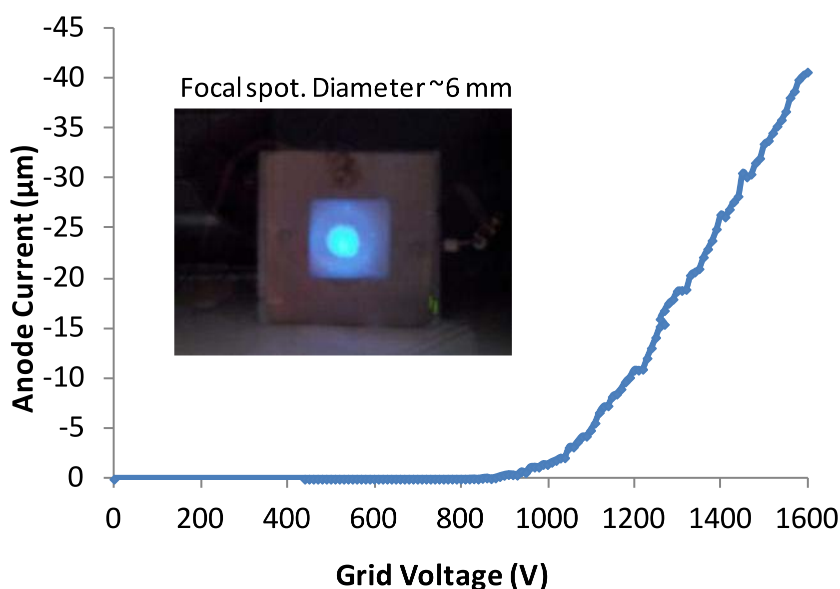

Figure 4.5. *I-V* behavior for the CNT-based electrons source. Inset: Electron beam focal spot.

4.2.2. X-Ray Generation Characteristics. Once the I-V behavior of the CNT based electron source was determined, the evaluation of the X-ray generation characteristics of this source was performed. For these experiments, the P-47 scintillator screen shown in Figure 4.4 was replaced by an X-ray target. Based on previous MCNPX simulations [3], a 650 nm thick tungsten target was selected as the optimum target for transmission X-ray generation for an incident 30kV electron beam. Therefore, an Aluminum-6061 anode with a 700nm thick layer of tungsten sputtered on it was used as X-ray target. In Figure 4.6 the experimental set-up including the X-ray target is presented.

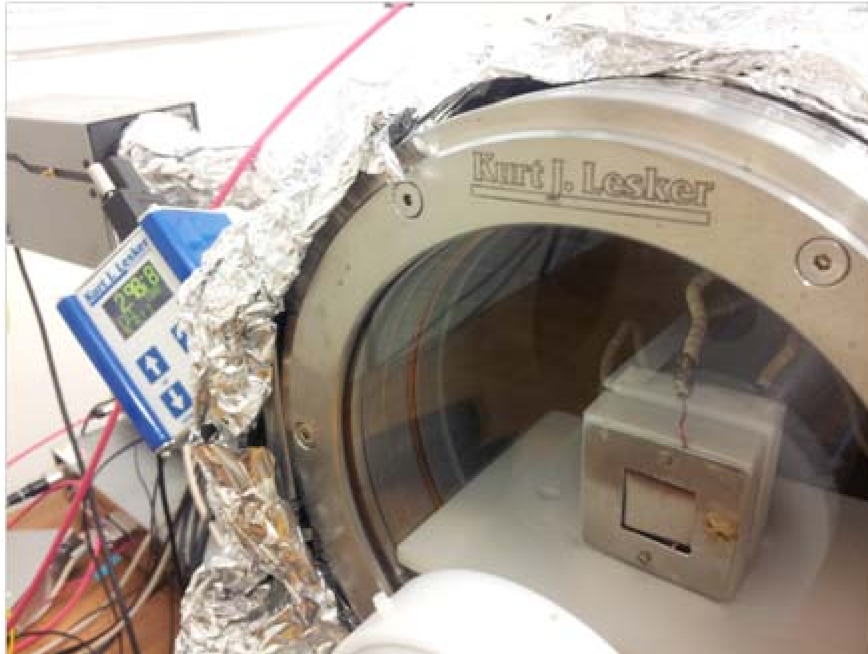

Figure 4.6. Experimental set-up used inside the vacuum chamber to evaluate the generation of X-rays. The 700 nm tungsten target can be seen facing the glass view port.

To evaluate the X-ray generation characteristics, the X-ray detection system described in subsection 4.1.5 is used. The gate voltage was set at 600 V, providing an anode current around 4 to 6 nm. The power supply Matsusada AU120P10 described in subsection 4.1.4 was used to vary the anode voltage between 1.0 kV and 30 kV. X-rays were counted for 30 seconds for each anode voltage, and results are presented in Figure 4.7.

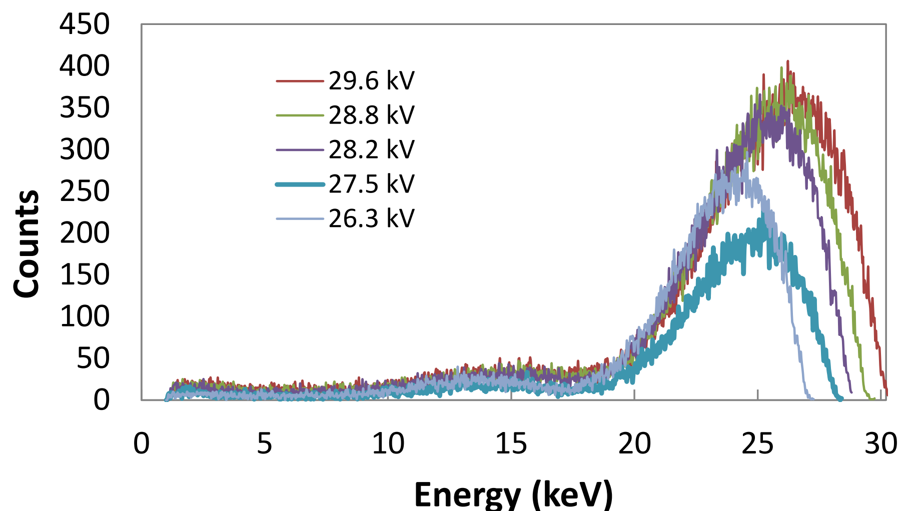

Figure 4.7. X-ray spectrum at different electron beam energies obtained for the CNT-based electron source.

No X-ray results below 20 kV are shown. This is due to the fact that most of the Bremsstrahlung X-rays below this energy are filtered by the anode and vacuum system components. In Figure 4.7, it is seen how the maximum X-ray energy and the number of X-rays (area under the curve) increase as the anode voltage is increased. This indicates that the energy of transmitted X-rays could effectively be controlled by the voltage applied at the anode.

These results are in concordance with those obtained from OOPIC Pro simulations for the anode voltage versus electron beam energy (Figure 3.12). In fact, Figure 4.8 shows a comparison between the simulation results obtained for the energy of the electron beam at the anode and experimental results obtained for the maximum X-ray energy at different anode voltages. As expected, a strong correlation between these variables in observed.

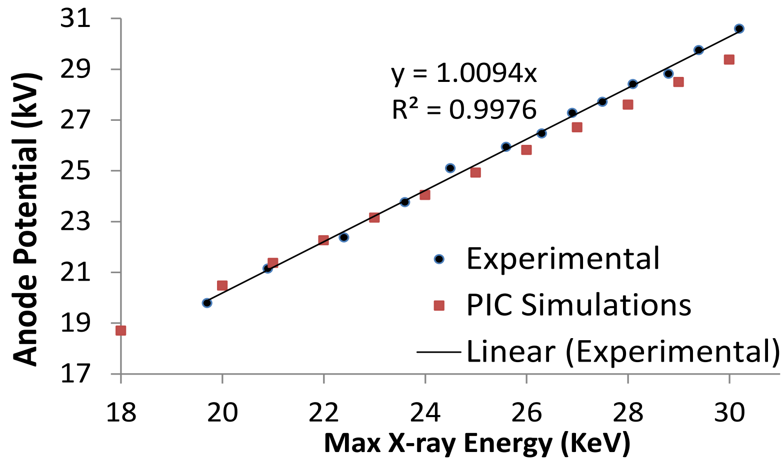

Figure 4.8. Anode potential versus maximum. X-ray energy. Simulation and experimental results.

5. FIRST GENERATION FIELD EMITTER ARRAY

As shown in Figure 5.1, the FEA prototype is composed of 9 pixels arranged in a 3x3 pixel array, with a pixel size of 225 µm by 225 µm, and a pitch of 500 µm. As mentioned in Section 2, N-UNCD films are used as field emitter materials. Therefore, this section is dedicated to describe the fabrication procedure of the first N-UNCD FEA prototype and its FE characteristics.

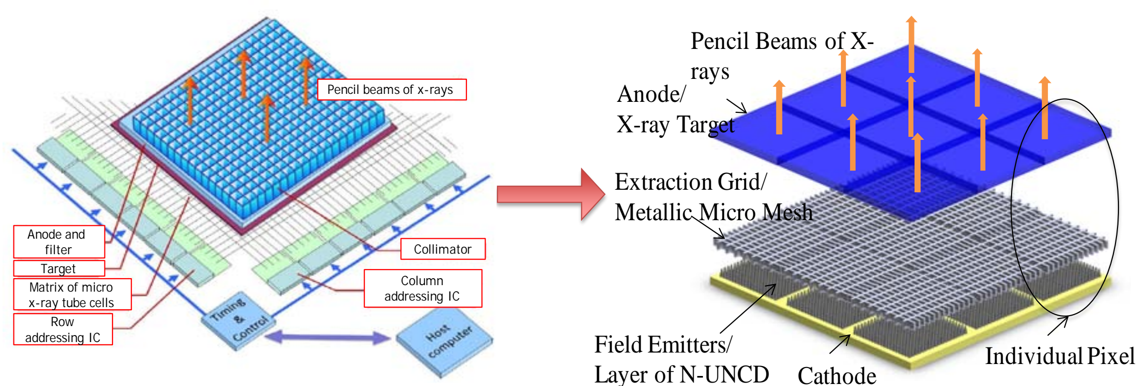

Figure 5.1. Right: Flat-Panel X-ray source. Left: Proposed 3x3 FEA prototype. To simplify the diagram, spacers and other elements are not shown in this image.

5.1. PROTOTYPE FABRICATION

The N-UNCD prototype fabricated has a cathode-extraction grid structure. It was developed using a microfabrication process that allowed for array to be composed of individually addressable N-UNCD pixels. This microfabrication work was performed entirely in the 11,500 sq. ft. clean room facilities of the Center for Nanoscale Materials at Argonne National Laboratory. Direct write optical lithography and contact UV lithograph, as well as different wet and dry etching techniques were used in this process. In addition, thin films were deposited using techniques such electron beam evaporation, plasma enhanced chemical vapor deposition (PECVD) and microwave plasma enhanced chemical vapor deposition (MPCVD). A flow schema of the steps involved in the

microfabrication of the N-UNCD FEA prototype is shown in Figure 5.2 and the process is described next.

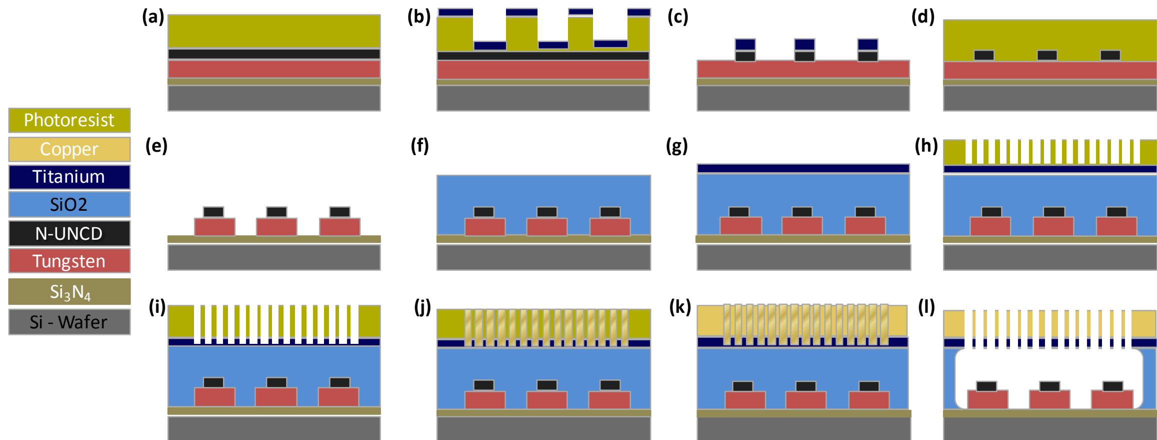

Figure 5.2. Process flow of the microfabrication process of the FEA microfabrication process: (a) - (e) show the steps involved on the growth of N-UNCD films on a tungsten substrate, (f) indicates the deposition of a 5 µm thick SiO2 layer for electrical insulation, (g) - (l) show the steps to electroplate a copper grid used as extraction electrode for field emission.

To start the FEA microfabrication process, p-type (100) Si wafers are coated with a low stress 1 µm Si_3N_4 layer deposited by low-pressure chemical vapor deposition (LPCVD). This Si_3N_4 layer provides electrical insulation between the Si wafer and the N-UNCD electron emitter layer. Next, an AJA International Inc. magnetron sputtering system was used to sputter a 250 nm tungsten layer onto the Si_3N_4 layer. This process was carried out at room temperature, 200W RF power, and 5mTorr. This W layer provides an electrical connection to the N-UNCD emitters and also serves as a seed layer for the N-UNCD growth process [23].

After W deposition, a 500 nm planar layer of N-UNCD field emitters is grown (Figure 5.2- (a)). In this stage, the W layer is seeded with nanodiamonds using a methanol solution containing commercial “Blue Seeds” nanodiamonds. After seeding, the N-UNCD layer is grown at 850°C using a MPCVD process developed by Argonne National Laboratory researchers [45]. For the growth process, a synthesis gas composed

of CH_3, Ar and N_2 is employed, with N2 accounting for 20% of the total gas composition. This gas composition of the growth plasma is selected such that maximum n-type conductivity is achieved for the N-UNCD films [25]. A Lambda Technologies Inc. 915 MHz large-area MPCVD system is used for the N-UNCD growth process.

To obtain a hard mask for pattern transfer in the N-UNCD layer, a 50 nm Ti layer is deposited by e-beam evaporation after UV lithography, Figures 5.2-(b) and 5.2-(c). For patterning, a 2.7-μm-thick S1827 (Shipley) photoresist was spin coated for 30 seconds at 3000 rpm, baked at 115°C for 1 minute and exposed using a Karl Suss MA6 mask aligner. The pattern was developed using 351 Microposit developer diluted 1:3 in deionized water (DIW) for 20 s. Ti lift-off was carried out at 700 ^{0}C in 1165 remover for 3 hours, following a 90 s ultrasonic bath, Figure 5.2 (b) and –(c). The N-UNCD layer was etched by reactive-ion etching (RIE) using an Oxford PlasmaLab 100 RIE-ICP system. This etching conditions were O_2 50 sccm, chamber pressure 10 mTorr, 1200 W ICP power and 10 W RF power (etching rate of ~50 nm/min) [46]. After etching the N-UNCD layer, a HF/H2O 1:9 solution was used to remove the Ti hard mask.

Following the growth and patterning of the N-UNCD emitter layer, an electrical circuit suitable for individually addressable pixels was designed. An overview of the arrangement of this electrical circuit can be seen in Figure 5.3. As shown, the W layer underneath the N-UNCDs is used to provide the voltage to the emitters.

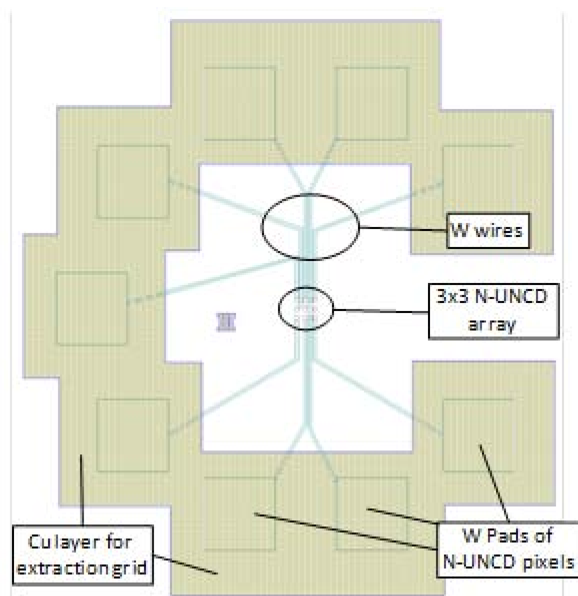

Figure 5.3. Electrical circuit designed for individually addressable pixels.

The patterning of the electrical circuit shown in Figure 5.3 was completed by UV optical lithography. For this, a maN-415 (Microchem) negative photoresist was spin-coated for 40 s at 3000 rpm and soft-baked at 115°C for 1 min (Figure 5.2-(d)). The tungsten layer was etched by RIE SF_6 plasma using a CS 1700 March system. The etching conditions were SF_6 20 sccm, 150 mTorr chamber pressure and 250 W RF power, for and approximate etching rate of 80 nm/min. After W etching, the microfabrication of the N-UNCD cathode with individually addressable pixels is completed, Figure 5.2-(e).

To integrate an electron extraction grid to the N-UNCD cathode, a standoff and electrically insulating layer is needed, as shown in Figure 5.2-(f). Due to its high dielectric strength, SiO_2 is used as the insulating material. In this step, a 5 μm layer of SiO_2 is deposited at 100 ^oC by PECVD. An Oxford Plasmalab 100 ICP CVD is used in this process. In the next step, copper was chosen as the extraction grid material due to its electrical and thermal properties. To improve the Cu adhesion characteristics to the previously deposited SiO_2 layer, a 50 nm layer of W was first sputtered onto the SiO_2 surface, as indicated in Figure 5.2-(g). To control the electroplating of the copper grid, a third optical UV lithography step was required, Figure 5.2-(h). In this step, S-1818 positive photoresist was used, allowing for a 1.8 μm thick copper grid with small electron

extraction openings. The copper electroplating was performed using a copper sulfate plating process from Lea Ronal, Inc. (Figure 5.2-(j)). The resulting Cu grid for the extraction of electrons has a pitch of 25 μm, hole-width of 19 μm and connecting bar thickness of 6 μm. An acetone bath was used to remove the photoresist from the surface.

Following the electroplating of copper, the 50 nm layer of W used for adhesion was etched by SF_6 RIE in the places where the S1818 photoresist was removed, Figure 5.2-(k). Finally, the SiO_2 layer under the copper grid was etched to expose the N-UNCD emitters, Figure 5.2-(l). A solution of buffered oxide etchant (BOE) was used to etch the 5 μm SiO_2 layer. As shown in Figure 5.2-(k), this SiO_2 etching step exposes the N-UNCD layer and completes the fabrication of the N-UNCD FEA prototype.

Optical micrographs obtained during the N-UNCD FEA fabrication process are shown in Figure 5.4. As seen, Figure 5.4-(a) shows the configuration of the tungsten voltage lines, Figure 5.4-(b) shows the N-UNCD/W/Si_3N_4 structure of one of the pixels, and Figure 5.4-(c) shows a the electroplated copper grid.

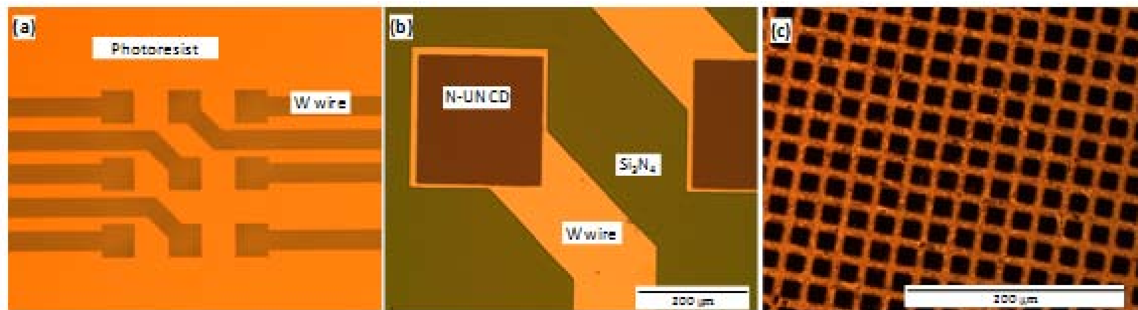

Figure 5.4. Micrographs of the N-UNCD prototype obtained during the microfabrication process (a) tungsten voltage lines, (b) configuration individual pixels, (c) electroplated copper grid.

In addition, optical micrographs of the 3x3 N-UNCD FEA prototype after completion of the microfabrication process are shown in Figures 5.5-(a) through (c). In these figures, the W electrical circuit and the 3x3 configuration of the N-UNCD pixels can be seen under the electroplated copper grid.

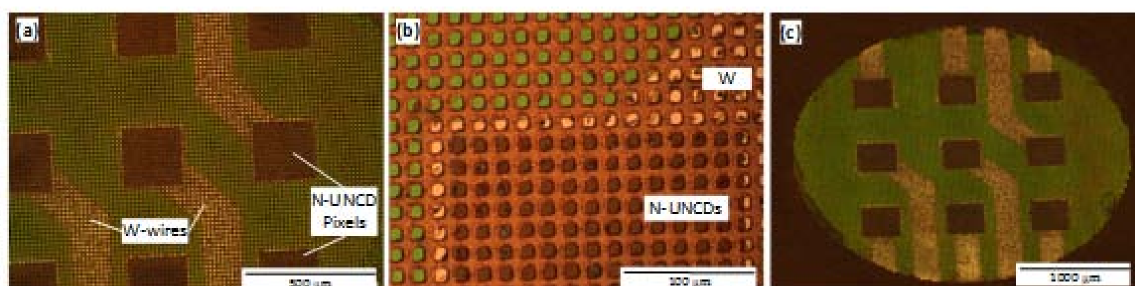

Figure 5.5. Optical micrographs of the first 3×3 N-UNCD FEA prototype. (a) 3×3 pixel array showing the W wires and N-UNCD pixels configuration under the electroplated copper extraction grid. (b) Close-up of a single N-UNCD pixel, (c) completed 3×3 pixel N-UNCD based FEA prototype.

5.2. FIELD EMISSION TESTING

Using a similar procedure to the one presented in Section 4 for testing the commercial CNT-based electron source, the FE characteristics of the microfabricated N-UNCD FEA prototype were evaluated by measuring its current-voltage behavior. For the experiments, the sample consisting of four 3x3 FEA was placed on an electrically insulated Teflon table, as shown in Figure 5.6-(a). The N-UNCD pixels and extraction grid contacts were connected to AWG 20 (0.032 in) Oxygen-free (OFHC) copper wires using silver epoxy, see Figure 6-(b). Before the I-V measurements were performed, the electrical contacts of the FEA were tested. Some pixels showed to have a small resistance, in the order of hundreds of ohms, between the Cu-grid layer and the W-wires. Therefore, only those pixels that showed infinite resistance between the two layers mentioned above were considered operational and were used for these experiments. In all cases, the field emission experiments were conducted at a pressure below 4×10^{-8} Torr. Additional details about the experimental set-up used for these experiments have already been presented in Section 4.

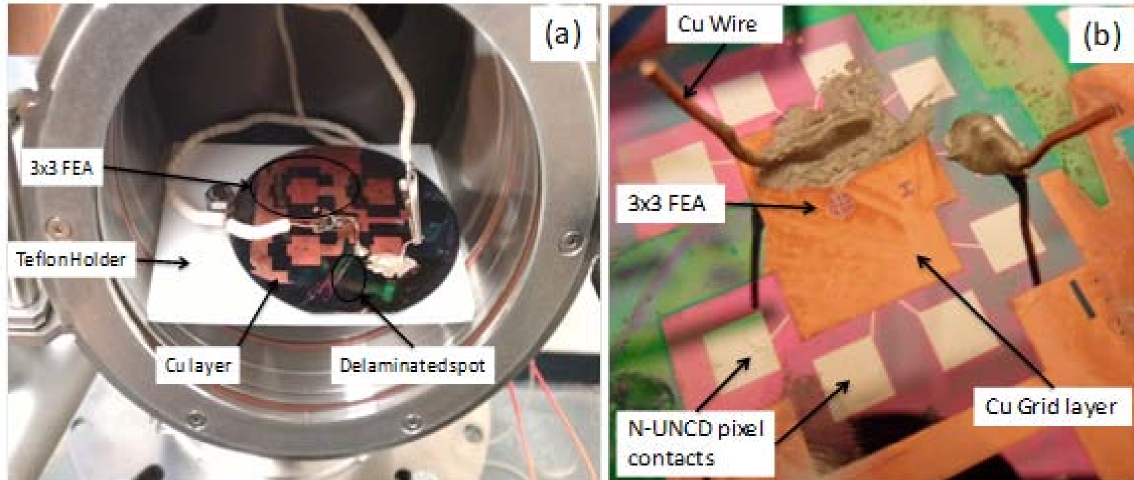

Figure 5.6. Micro fabricated N-UNCD 3x3 field emitter arrays. (a) Prototype placed inside vacuum chamber, (b) N-UNCD FEA components, including wires connected to the sample using silver epoxy.

To evaluate the *I-V* behavior of the N-UNCD prototype, the copper grid was electrically grounded and voltages between 0 and -140 V were applied to the N-UNCD emitter layer using the microfabricated W-wires shown in figure 5.5. The emission current at the grid (*I*) was recorded as the cathode voltage was varied. In this experiment two grids were tested and compared: (1) the electroplated copper grid (EP Grid) shown in Figure 5.5, which was monolithically fabricated according to the procedure presented in subsection 5.1, and (2) a 1000 mesh TEM copper grid (TEM Grid) which was attached to the copper electroplated layer of the FEA using silver epoxy. The distance between the N-UNCDs and the EP grid is 5 µm, while the distance between the N-UNCDs and the TEM Grid is 7 µm. These values of the cathode-grid gaps were used to determine the externally applied electric field (*E*) explained in Eq. (1). The difference in the gap sizes between the cathode and the grid configurations (1) and (2) is due to the fact that the TEM grid was attached on top of the 2 µm copper electroplated layer, while the EP grid is part of the copper electroplated layer itself.

In Figure 5.7, the *I-V* behavior of the two cathode-grid configurations tested is presented. As seen, emission currents per pixel up to 4 µA were measured. Considering the pixel sizes, it leads to current densities in the order of 7.9 mA/cm^2.

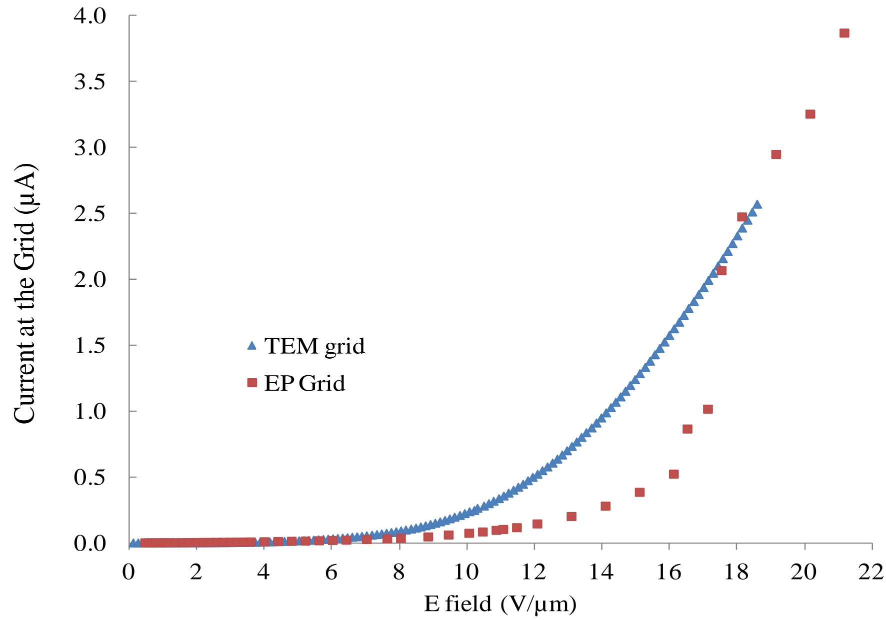

Figure 5.7. I-V characteristics of field emitted electrons from given N-UNCD pixels. (▲)Electroplated copper grid, (■)Mesh 100 TEM copper grid.

Based on the *I-V* results presented in Figure 5.7, the N-UNCDs FE characteristics were evaluated according to the Fowler-Nordheim (FN) theory presented in Section 2. According to this theory, FN graphs were made by plotting the values of $\ln(I/E^2)$ as a function of 1/E. The resulting FN plots are shown in Figure 5.8.

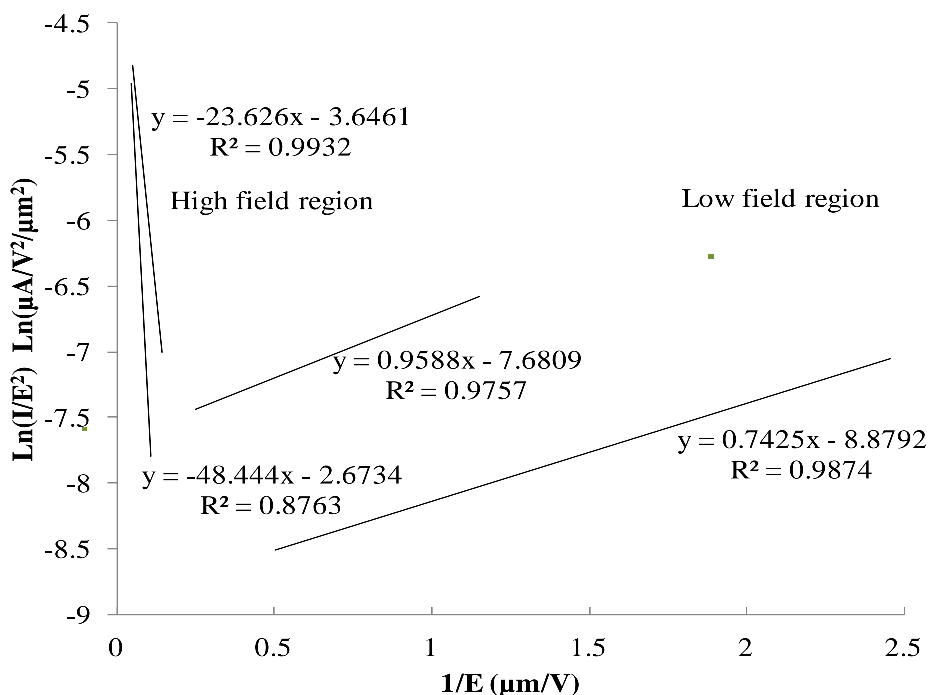

Figure 5.8. Fowler-Nordheim plots of the cathode-grid configurations tested. (▲) electroplated copper grid, (■) mesh 100 TEM copper grid.

Two regions are identified in the FN plots presented in Figure 5.8, a high field region and a low field region. For the two cathode-grid configurations tested, the data in the low and high field regions are fitted to linear functions. The turn-on electric field (E_0) for the device can be calculated by finding the intercept between the linear functions obtained for the high and low field regions [47-49]. Furthermore, the FE parameters of the N-UNCD samples can be extracted from the linear function fitted to the data in the high field region of the FN plots, Figure 5.9.

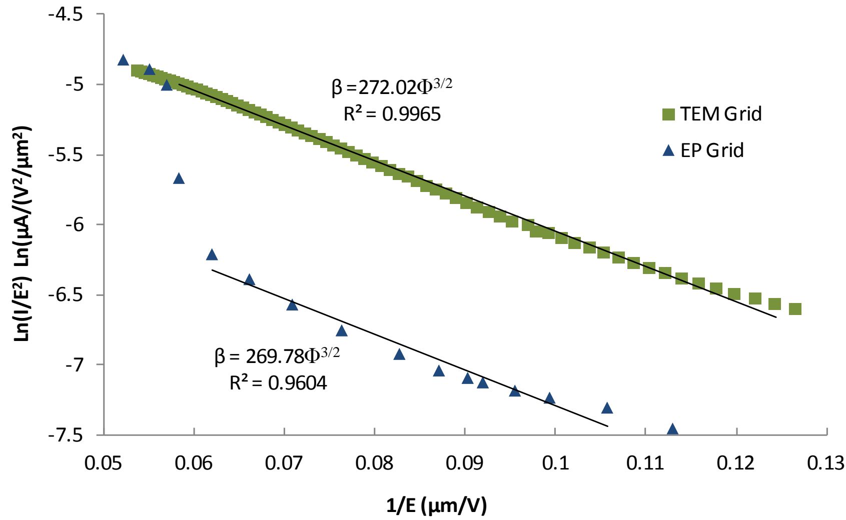

Figure 5.9. High field region of the FN Plots used to calculate β as a function of $\phi_{N\text{-}UNCD}$ for the two cathode-grid configurations tested. (▲)EP Grid, (■) TEM Grid.

Based on Eq. (1), the work function ($\phi_{N\text{-}UNCD}$) and the geometrical field enhancement factor (*β*) of the N-UNCD samples can be related to the slope of the high field regions by Eq. (10):

$$slope_{FN} = \frac{\partial \ln(I/E^2)}{\partial(1/E)} = \frac{-B_{FN}\Phi^{3/2}_{N-UNCD}}{\beta} \qquad (10)$$

Therefore, Eq. (10) is used in combination with the slopes of the FN plots shown in Figure 5.9 to determine the N-UNCDs effective work function defined in Eq. (11).

$$\Phi_{\varepsilon} = \frac{\Phi^{3/2}_{N-UNCD}}{\beta} \qquad (11)$$

Results obtained for the N-UNCD FE parameters are summarized in Table 5.1. These values are in agreement with values reported in the literature for similar systems [50-52].

Table 5.1. Field emission characteristics of the N-UNCD FEA prototype.

	E_o (V/μm)	J_e (mA/cm^2)	ϕ_e (eV)
TEM Grid	6.29	5.37	0.0036
EP Grid	6.24	6.42	0.0037

In Figure 5.9, the FN plot for the EP Grid sample showed a deviation from linearity at high electric fields. This deviation from linearity is believed to be associated with remnant SiO2 left between the electroplated copper grid and the N-UNCDs layer. This remnant of SiO_2 is left after the final BOE etching step and reduces the available emission are. It also affects the effective extraction field on the surface of the emitter's layer due to the finite resistance of the SiO2 [49].

In addition, when the electrical contacts of the FEA were tested, some pixels were found to be short-circuited. This short-circuit problem is related to copper delamination issues observed during the microfabrication process (Fig. 5.10).

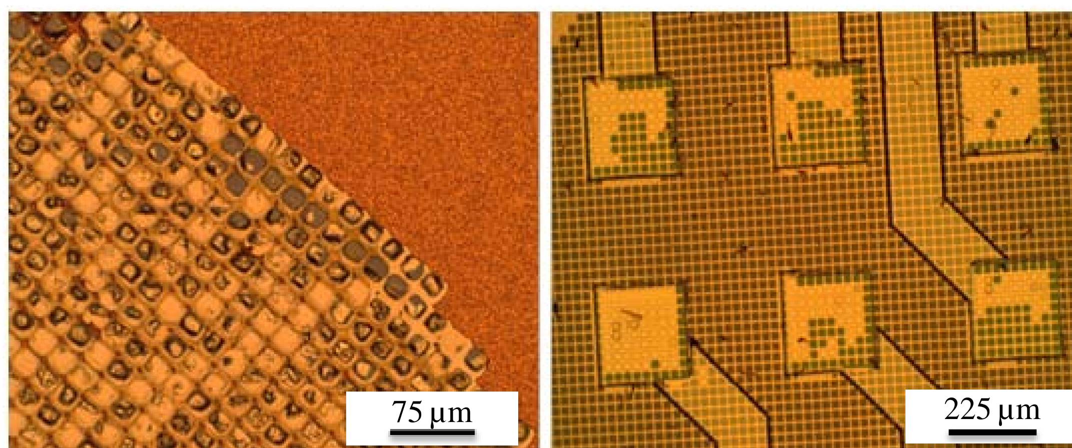

Figure 5.10. Optical micrographs of samples showing copper delamination and grid removal issues.

The final microfabrication step of the first N-UNCD FEA prototype corresponds to BOE etching of the SiO2 layer under the copper grid. However, the delamination issues mentioned above led to removal of the SiO2 insulating layer in the places where

the copper layer was missing. It allowed for undesired etching of the SiO_2 layer in some places, allowing for electrical contact between the Cu and W layers that should have been separated by the insulator.

As a solution to these problems, alternative FEA designs are evaluated in the next section of this document.

6. SECOND GENERATION FIELD EMITTER ARRAY

As an alternative to the microfabrication problems found for the first N-UNCD FEA prototype, single and double gate N-UNCD FEA designs are evaluated. These alternative designs are aimed to simplify the microfabrication process, and to improve the FE characteristics of the electron source. This section presents simulation and experimental results for these alternative N-UNCD FEA designs.

6.1. FITTING SIMULATION TO EXPERIMENTAL RESULTS

Prior simulating the alternative design, a comparison between simulations and actual experimental results is performed. In this regard, the experimental *I-V* characteristics obtained for the first N-UNCD FEA prototype (Section 5) are compared to *I-V* results obtained when an equivalent system is simulated with OOPIC Pro. To perform this comparison, the values of work function (Φ_{N-UNCD}) and geometrical field enhancement factor (β) obtained from the first N-UNCD FEA prototype are incorporated into the OOPIC Pro code used in the simulations. These values of work function and field enhancement the of the planar N-UNCDs are evaluated by using the N-UNCD FE characteristics presented in Table 5.1 in combination with Eq. (11), and assuming the N-UNCDs work function to be 4.5 eV. Therefore, β is estimated to be 2600. These values of β and Φ_{N-UNCD} are comparable to values reported elsewhere [8,51,52]. To carry out this comparison, simulation and experimental results were adjusted to a pixel size of 100 µm x 100 µm, as shown in Figure 6.1.

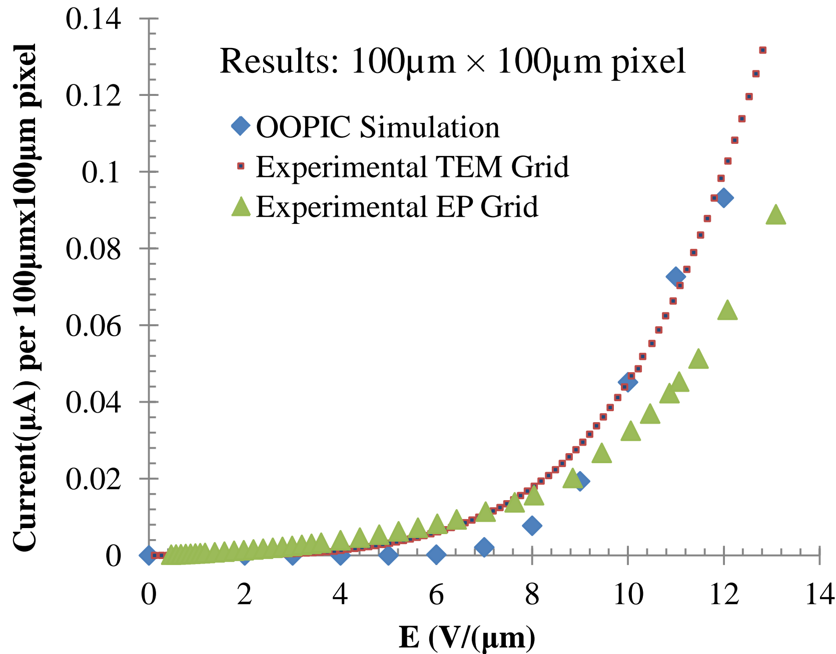

Figure 6.1. *I-V* characteristics of the first N-UNCD FEA prototype: Using a 1000 TEM Grid, the electroplated copper (EP) grid and values obtained from the OOPIC Pro simulations.

In Figure 6.1, the emission current per pixel measured at the grid is around 0.1 µA at an extraction field of 12 V/µm. These experimental values are smaller than those obtained from the PIC simulations. It should be noted that the simulation values shown in Figure. 6.1 were adjusted by multiplying them by a factor of 0.13. This adjustment factor is believed to be associated to the real emission area per pixel in the N-UNCD FEA prototype versus the ideal 100 µm × 100 µm emission area per pixel considered in the simulations. As mentioned before, this difference in emission area is associated with remnant SiO_2 left on the N-UNCDs layer after BOE etching.

Nonetheless, after this correction factor is applied, a good match between experimental and simulation results are obtained. Hence, PIC simulations of the alternative FEAs presented in the following subsections are expected to be a good indicator of their actual performances.

6.2. DESIGN OF ALTERNATIVE FEA GEOMETRIES

FE results obtained from the first N-UNCD FEA and problems found during its microfabrication suggested that a modification to the cathode-extraction grid geometry originally proposed was needed. This subsection describes the design through PIC simulations of alternative single and double gate configurations.

6.2.1. Single Gate Configuration. The main change introduced to first N-UNCD FEA prototype is the substitution of the complex grid geometry of the extraction electrode by a simpler single extraction gate aperture. As will be explained later, this modification leads to simplifications on the microfabrication process. As shown in Figure 6.2, in the new design, extraction gates with aperture sizes between 6 µm and 30 µm were considered in the simulations. For each aperture size, the electron trajectories and the current-voltage (I-V) characteristics of the resulting single gate N-UNCD FEA were determined

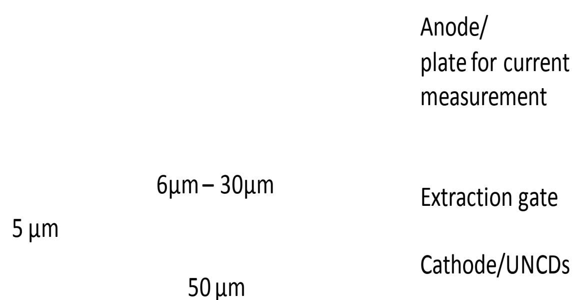

Figure 6.2. Single gate geometry proposed for the second generation N-UNCD FEA.

Additionally, the cathode-extraction gate distance was set to 5 µm (Figure 6.2). This gap corresponds to the thickest SiO2 layer that could be reliably deposited during the microfabrication of the first N-UNCD FEA prototype. Extraction gate apertures between 6 µm and 30 µm were tested. Also, to complete the triode structure for the simulation of the single gate FEA, an anode plate was placed 400 µm away from the cathode. In order to evaluate the electron emission characteristics of the system, the extraction gate was electrically grounded while a negative bias between 0 V and -70 V

was applied to the cathode. Current diagnostics at the extraction gate and the anode plate were recorded as the cathode voltage was changed.

The electron beam trajectories obtained for the different cathode-single gate configurations tested are shown in Figure 6.3.

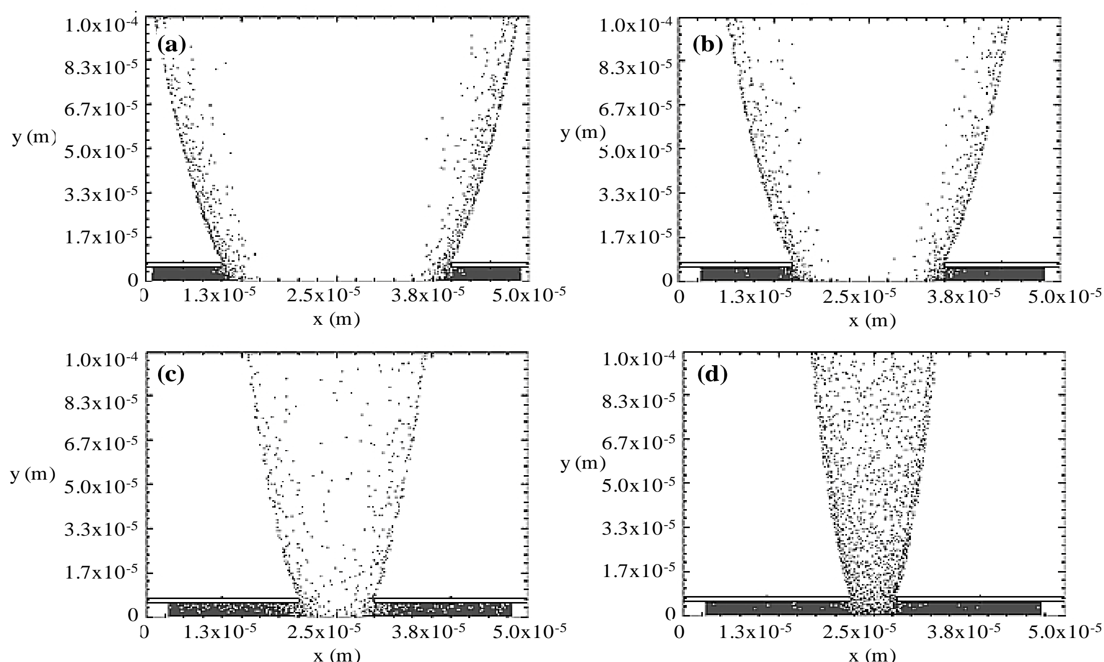

Figure 6.3. Electron beam trajectories for different extraction gate apertures: (a) 30 μm, (b) 20 μm, (c) 10 μm and (d) 6 μm. Gate voltage: 0 V, cathode voltage: -30 V, anode voltage: 258 V.

As expected, for large gate apertures (20 μm – 30 μm), electrons at the cathode tend to be extracted mostly from the regions under the edges of the extraction gate; leading to the generation of a highly diverging, non-uniform electron beams. On the other hand, a more uniform electron extraction pattern is observed for smaller gate apertures (6 μm – 10 μm). The effect of these emission patterns on the overall performance of the FEA is evaluated in terms of their *I-V* behavior, and results are presented next in Figure 6.4.

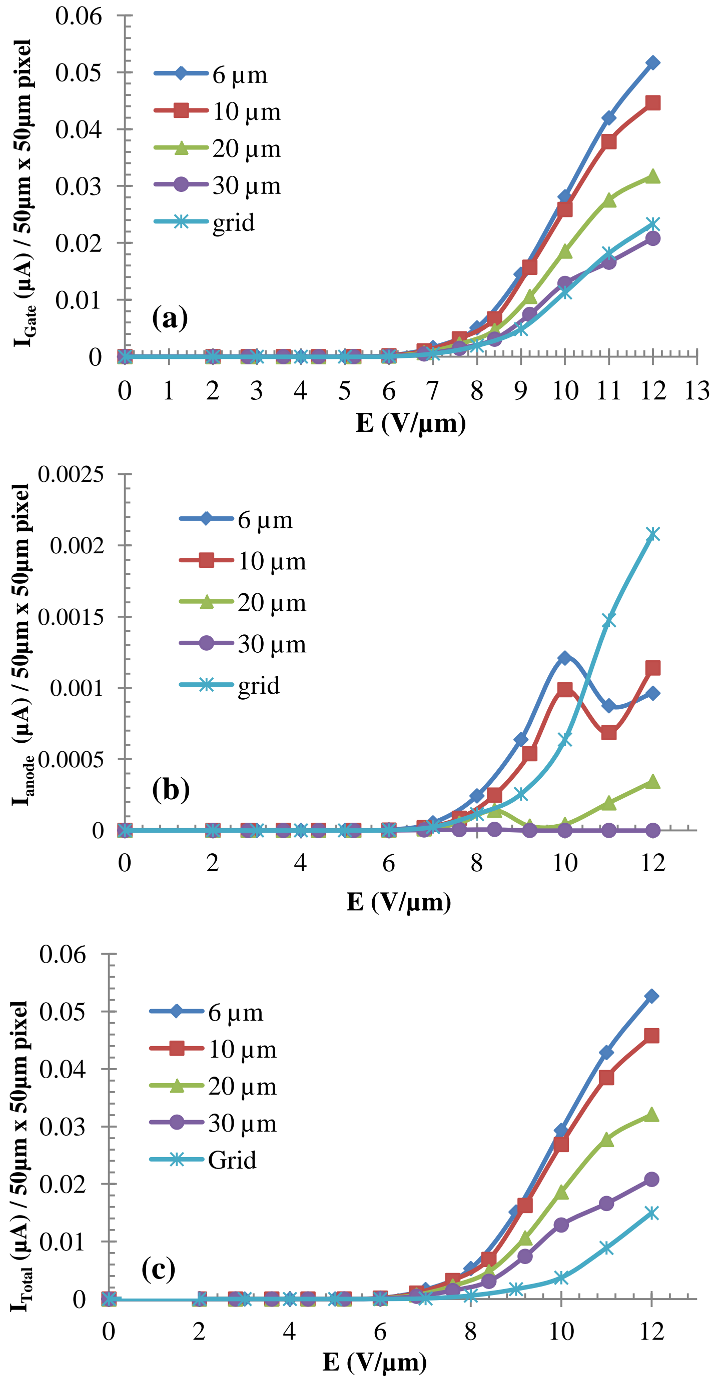

Figure 6.4. Current-voltage (*I-V*) behavior of the different triode configurations simulated. Different current diagnostics are considered: (a): Gate current, (b): Anode current. (c): Total current (gate + anode current).

Values for the gate (I_{gate}) and anode (I_{anode}) currents collected from the simulations are presented in Figures 6.4-(a) and 6.4-(b), respectively. Additionally, the

total emission current (I_{Total}) was defined as the summation of gate and anode currents at a given extraction voltage, Figure 6.4-(c). The general behavior observed in Figures 6.4-(a) through (c) indicates that at a given extraction voltage, smaller gate apertures yield higher values for the gate, anode and total currents. The emission currents for the electroplated grid configuration used in the first N-UNCD FEA prototype are also included in Figures 6.4-(a) through (c) (Grid series). A comparison between the values obtained for the different configurations shows that single gate configurations with gate apertures sizes between 6 µm and 10 µm yield higher emission currents. Therefore, changing the cathode–free standing grid configuration to a cathode–single extraction gate should have a positive impact on the overall electron FE performance of a second generation N-UNCD FEA prototype.

On the other hand, it is observed that smaller extraction gate apertures sizes lead to a decrease in the anode current at relatively high extraction voltages applied at the gate (48 V - 55 V). This decrease in the anode voltage is associated to space-charge limitation effects described by Child-Langmuir's law [42], and possible charge accumulation on the walls of the device. Due to these effects, a "virtual cathode" is created in the vicinities of the extraction grid (Figure 6.5-(c)), reflecting new emitted electrons and thus temporarily limiting the overall number electrons reaching the anode [2, 27, 28, 43, 44].

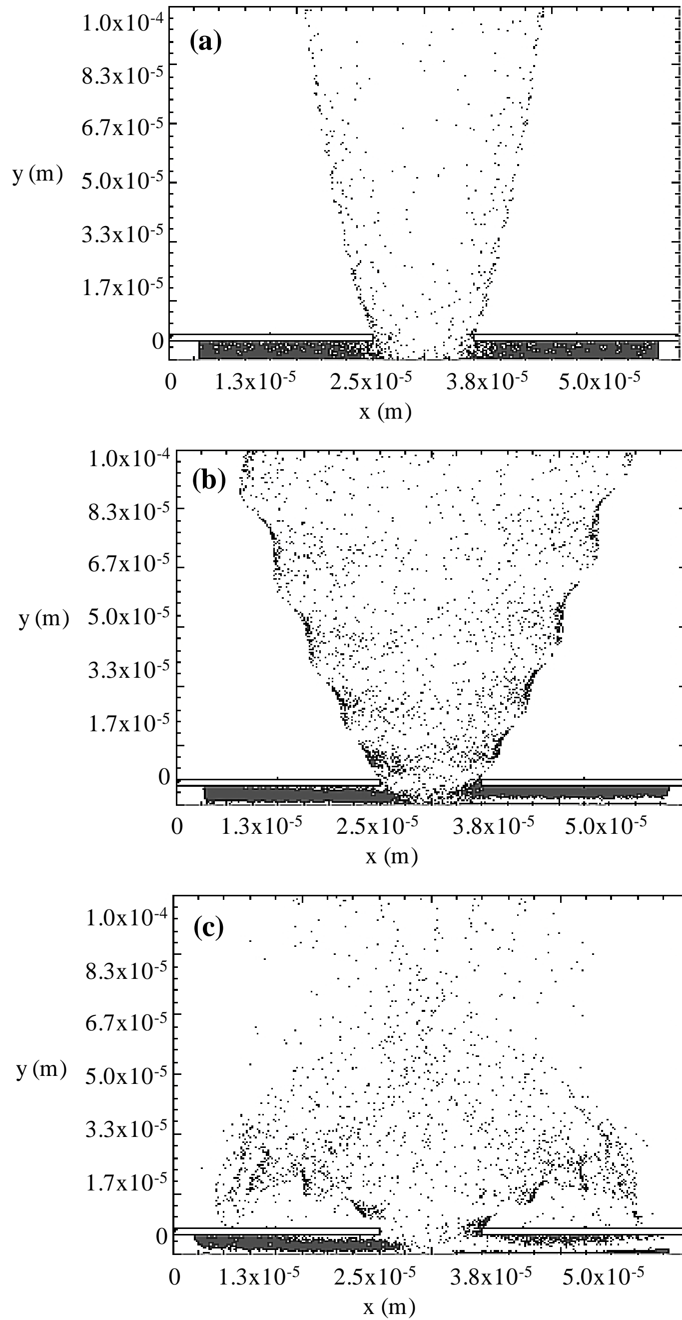

Figure 6.5. Space-charge limitation effects at different cathode voltages: (a) -30 V, (b) -46 V and (c) -55 V. Gate aperture: 10 μm. Gate voltage: 0 V, Anode voltage: 258V.

6.2.2. Double Gate Configuration. Simulations of the single gate FEAs indicated that small gate apertures will yield better electron emission results. However, it was also observed that this single gate configuration presents problems that could affect the overall performance of the FEA, including the generation of highly divergent electron beams. Therefore, in order to take full advantage of the second generation N-UNCD FEA, the FE characteristics of an alternative double gate FEA structure are also explored (Figure 6.6).

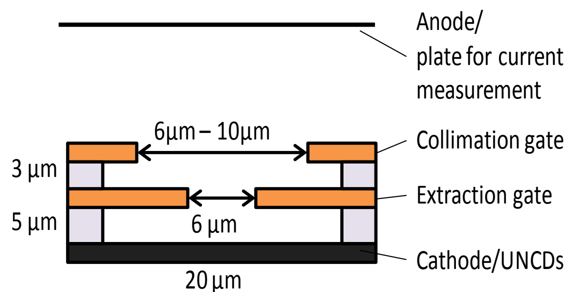

Figure 6.6. Proposed double-gate N-UNCD FEA configuration.

Based on the results obtained for the single gate structure, an aperture size of 6 µm was chosen for the extraction gate. As in the single gate geometry case, the cathode-extraction gate gap was set to 5 µm. The gap between the extraction gate and the electron beam collimation gate (second gate) was set to 3 µm. Two aperture sizes were considered for the collimation gate, 10 µm and 16 µm. For the simulations, the extraction gate was electrically grounded. According to results obtained for the single gate case, two extraction voltages (V_{gate}) were considered, 35 V and 40 V. In each case, the voltage on the collimation gate (V_{col}) was changed between 0 V and the value of the extraction voltage (35 V or 40 V). Values for the gate (I_{gate}) and anode currents (I_{anode}) were recorded as the ratio between the collimation/extraction gate voltages was changed.

Figures 6.7 and 6.8 show the electron beam trajectories obtained for the double gate geometry for different V_{col}/V_{gate} ratios. The best results in terms of beam collimation were obtained in the case in which a relatively small (10 µm) collimation gate aperture

was employed. However, it is expected that small gate apertures would affect the effective electric field acting over the emitters, reducing the overall emission current [53].

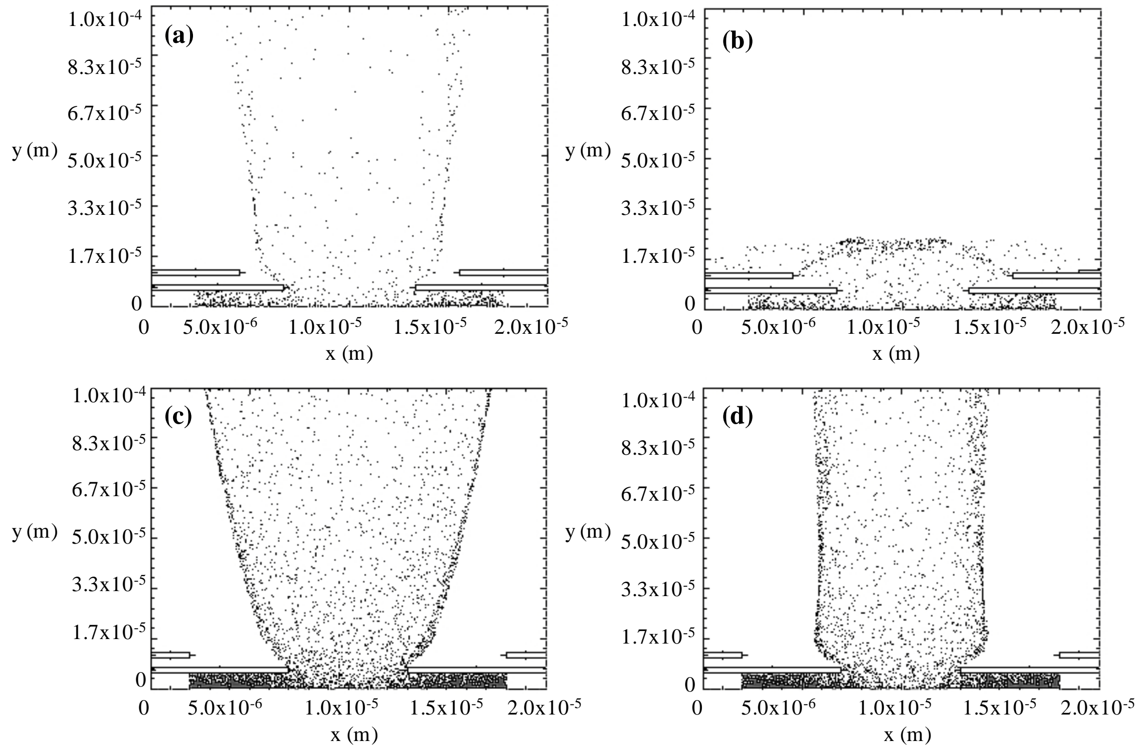

Figure 6.7. Electron beam trajectories for the 10 µm ((a) and (b)), and 16 µm ((c) and (d)) double-gated structures, gate aperture: 6 µm. Cathode voltage: -35 V. Gate voltage: 0 V. Collimation Voltage: -10 V for (a) and (c); and -30 V for (c) and (d).

The electron beam trajectories shown in Figures 6.7 and 6.8 include those obtained at collimation voltages of -10 V and -30 V. In general, higher beam collimation was observed at higher collimation potentials. However, even though results show that the divergence of the electron beam can be reduced, it should be pointed out that a negative potential is used in the collimation process. Therefore, at high collimation potential electrons could be reflected back from the collimation region and end up being collected at the extraction gate see Figure 6.7-(b). This would affect the number of electrons reaching the anode of our FEA and consequently the possible X-ray generation

[3, 7]. Cross-over of the electron beam due to high collimation strength (Fig. 6.8-(b)) should also be expected, affecting the final focal spot size.

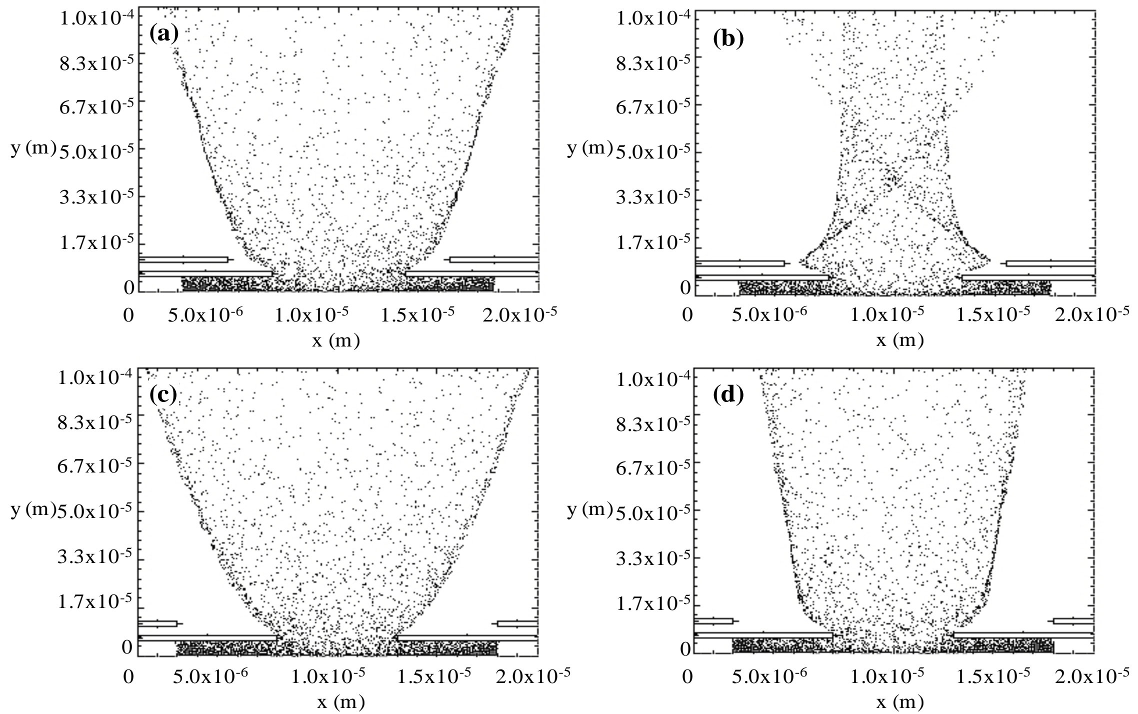

Figure 6.8. Electron beam trajectories for the 6 μm (top) and 16 μm (bottom) double-gated structures, gate aperture: 10 μm. Cathode voltage: -40 V. Gate voltage: 0 V. Collimation Voltage: -10 V (a) and (c) and -30 V (c) and (d).

Thus, for a better evaluation of the performance of the proposed double gate FEAs, their gate and anode emission currents are analyzed for different collimation aperture sizes and V_{col}/V_{gate} ratios. For this analysis, two gate voltages have been considered, -35 V and -40 V. Results obtained are summarized in Figure 6.9 for the V_{gate}= -35 V case and Figure 6.10 for the V_{gate}= -40 V case.

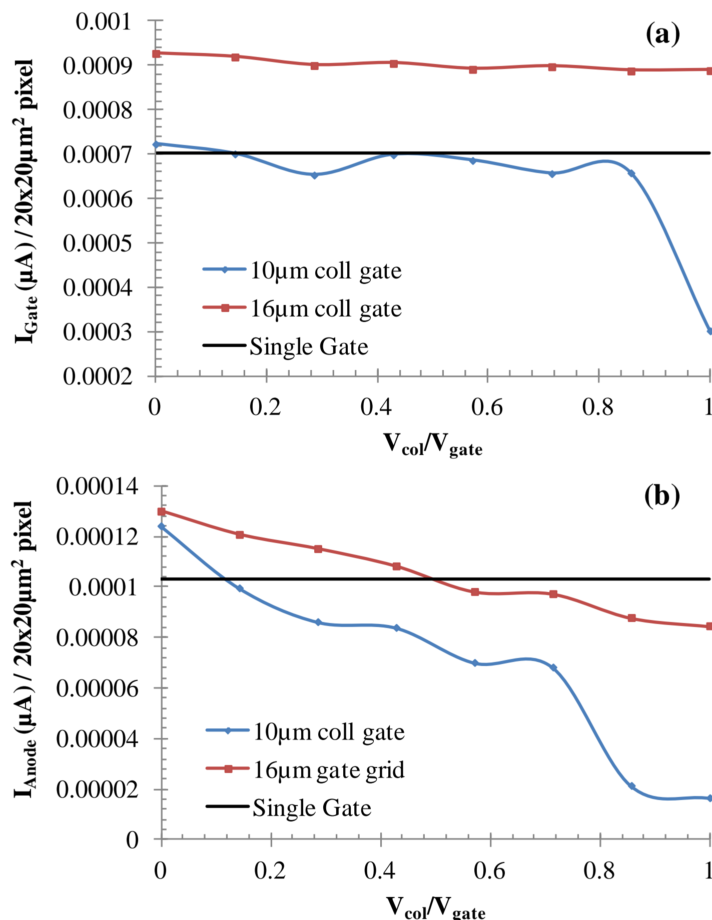

Figure 6.9. Electron emission characteristics for the double-gate structure in comparison to the single gate structure, gate voltage: 0 V, cathode voltage: -35 V. (a) Gate current, (b) anode current.

Results presented in Figures 6.9 and 6.10 indicate that in every case there is an optimum collimation/gate voltage that yields the best results for both gate and anode current [53]. In the case of the 10 µm collimation gate, even though a highly collimated beam can be obtained, the grid and anode current are below (or have similar values to) the ones obtained for the single gate configuration. On the other hand, for the 16 µm collimation gate case, an increase in both the grid and anode currents is observed. This result indicates that a relatively large collimation aperture would be more beneficial to the overall behavior of the second generation N-UNCD FEA in terms of both, collimation and electron emission characteristics. These results are in agreement with results presented in the literature for metallic double gate FEA [53], in which the authors report

that the best results for double gate FEAs are obtained for collimation gate aperture sizes between two and three times the size of the extraction gate.

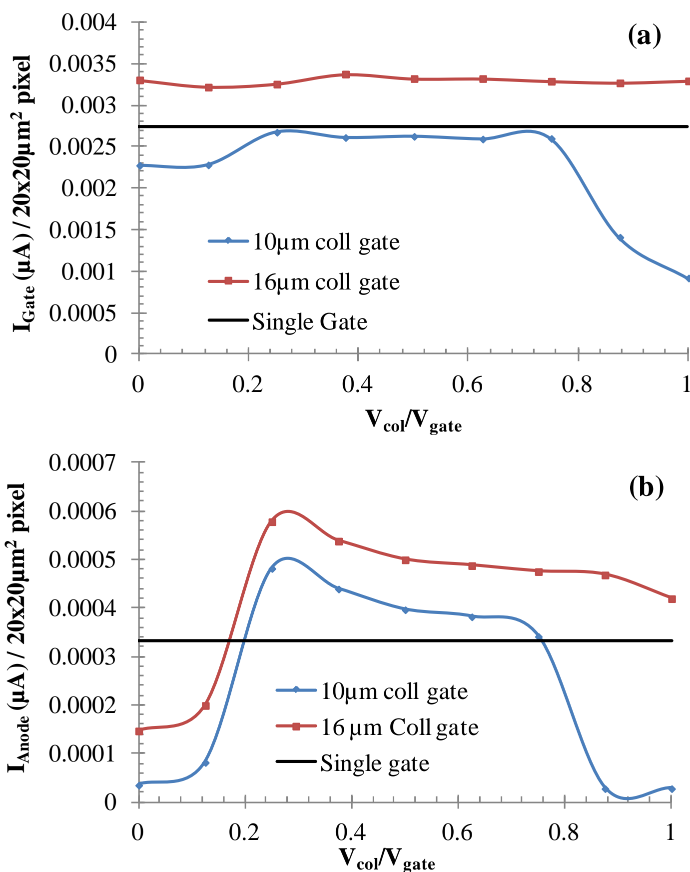

Figure 6.10. Electron emission characteristics for the double-gate structure in comparison to the single gate structure, gate voltage: 0 V, cathode voltage: -40 V. (a): Gate Current. (b): Anode Current.

Simulation results presented above showed that when compared to the first N-UNCD FEA, alternative single gate designs will yield a better performance when small gate apertures are employed. Also, when a double gate FEA configuration is used, the best collimation results are expected for collimation gates with relatively large aperture sizes. Based on these results, the microfabrication of a second generation N-UNCD FEA prototype was carried out.

6.3. ALTERNATIVE N-UNCD FEA FABRICATION PROCEDURE

Same as with the first N-UNCD FEA prototype, this microfabrication of the second generation FEA presented in this subsection was carried entirely in the clean room facilities of the Center for Nanoscale Materials at Argonne National Laboratory. This second generation prototype corresponds to a single gate FEA similar to the one simulated in the previous section. The microfabrication of this second generation prototype includes direct write optical lithography and contact UV lithograph, wet and dry etching techniques, and thin film deposition using electron beam evaporation, PECVD and MPCVD. A flow schema of microfabrication process is shown in Figure 6.11 and the process is described next.

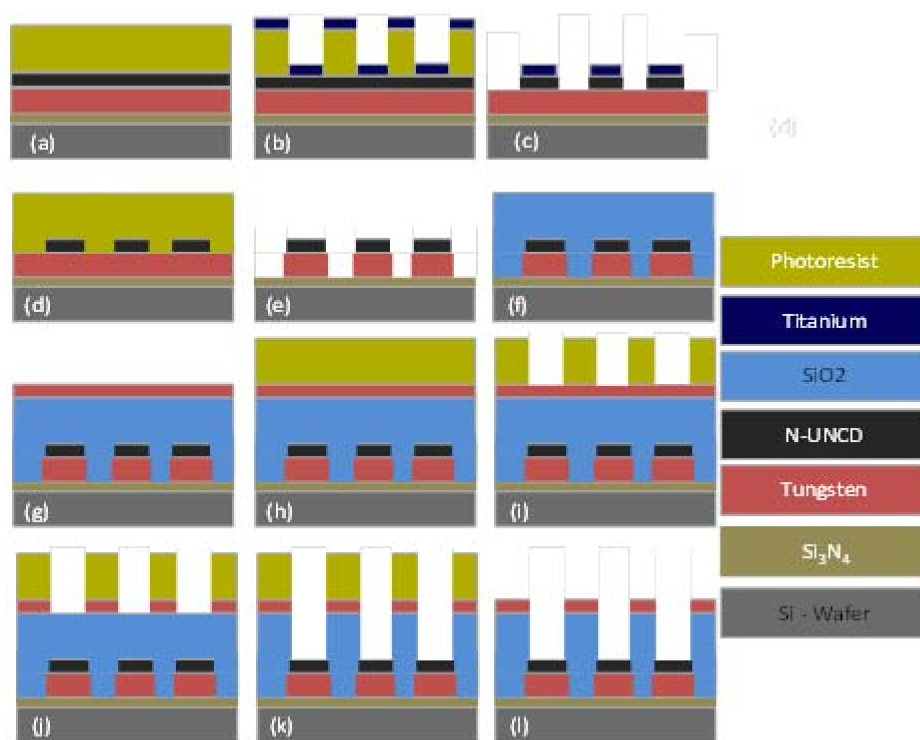

Figure 6.11. Microfabrication process of the second generation single gate N-UNCD FEA.

The microfabrication of the second generation N-UNCD FEA starts with p-type (100) Si wafers coated with a low stress 1 μm Si_3N_4 layer deposited by LPCVD.

Afterwards, a 200 nm tungsten layer was sputtered onto the Si_3N_4 layer at room temperature, 200W RF power, and 5 mTorr. This W layer is used to provide electrical connection to the N-UNCD emitters. After W deposition, a 1µm layer of N-UNCD emitters is grown at 850°C using the 915 MHz MPCVD process described in earlier sections. A 50 nm Ti layer deposited by e- beam evaporation after UV lithography is used as hard mask for pattern transfer. Figures 6.11-(a) through 6.11-(c). For patterning, a 1.8 µm thick S1818 photoresist was spin coated at 3000 rpm, baked at 115^0C for 1 min and exposed using a Karl Suss MA6 mask aligner. The pattern was developed using 351 Microposit developer diluted 1:3 in deionized water (DIW) for 30 s. Ti lift-off was done at 100 ^{0}C in 1165 remover for 3 hours, following a 90 s ultrasonic bath. The N-UNCD layer was etched by O_2 ICP-RIE, Figure 6.11-(c). This etching was performed by using oxygen 50 sccm, chamber pressure 10 mTorr, 1200 W ICP power and 10 W RF power.

After etching the N-UNCD layer, a HF/H_2O 1:9 solution was used to remove the Ti hard mask. Following the growth and patterning of the N-UNCD emitter layer, an additional UV lithography step was employed to design a W electrical circuit suitable for individually addressable pixels. To pattern this circuit, a maN-415 negative photoresist was employed, Figure 6.11-(d). This photoresist was spin-coated at 3000 rpm and baked at 100°C for 90 s. Afterwards; tungsten was etched by SF_6 RIE at 20 sccm, 150 mTorr chamber pressure, and 250W RF power, Figure 6.11-(e).

Following the W etching, a 3 µm layer of SiO_2 is used as spacer and insulator between the N-UNCD layer and the extraction gate (Figure 6.11-(f)). This SiO_2 layer is deposited at 100°C by PECDV using an Oxford Plasmalab 100 ICP CVD system. Next, a 300 nm layer of tungsten is sputtered onto the SiO_2, as shown in Figure 6.11-(g). This process was carried out at room temperature, 200W RF power, and 5mTorr using an AJA International Inc. magnetron sputtering system. This step represented one of the main differences between the microfabrication process of the first and second generation N-UNCD FEAs. In the case of the second generation FEA, no electroplating of copper is employed for the electron extraction layer, instead; the extraction gate is made exclusively of a second layer of tungsten, Figure 6.11-(g). A third UV lithography is employed to pattern this extraction gate layer. A S1818 positive photoresist is spin-coated at 3000 RPM for 30 s, soft baked at 115 °C for 1 min and exposed using a Karl Suss

MA6 mask aligner, Figure 6.11-(h). The pattern was developed for 15 seconds using 351 Microposit developer diluted 1:3 in deionized water (DIW), Figure 6.11-(i). Next, the tungsten layer is etched by RIE SF_6 plasma using a CS 1700 March system. The etching conditions were SF_6 20 sccm, 150 mTorr chamber pressure and 250 W RF power. Subsequently, BOE is used to etch the SiO2 layer SiO_2 layer and exposed the N-UNCDs, see Figure 6.11-(k). Finally, an acetone bath is used to remove the photoresist and complete the fabrication of the second generation N-UNCD FEA as shown in Figure 6.11-(l).

Micrographs of the N-UNCD films obtained after the 915 MHz, 815 °C MPCVD growth process are presented in Figure 6.12. It can be seen how the film has a relatively uniform microstructure, with grain sizes in the order of 5 to 10 nm as would be expected for N-UNCD films. These N-UNCD films showed a resistivity in the order of 0.002455Ω-cm and a sheet resistance around 24.4445 Ω/sq. The resistance measured in the surface of the films was in the order of 2.2 kΩ to 6.7 kΩ.

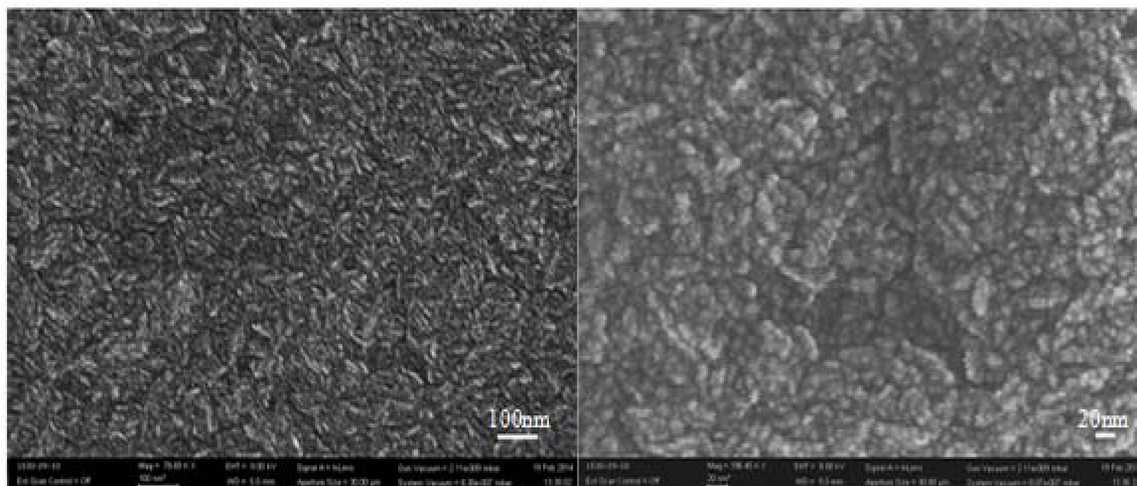

Figure 6.12. SEM images of the N-UNCD film used in the second generation FEA.

Optical micrographs obtained during the fabrication of this second generation N-UNCD FEA are shown in Figure 6.13.

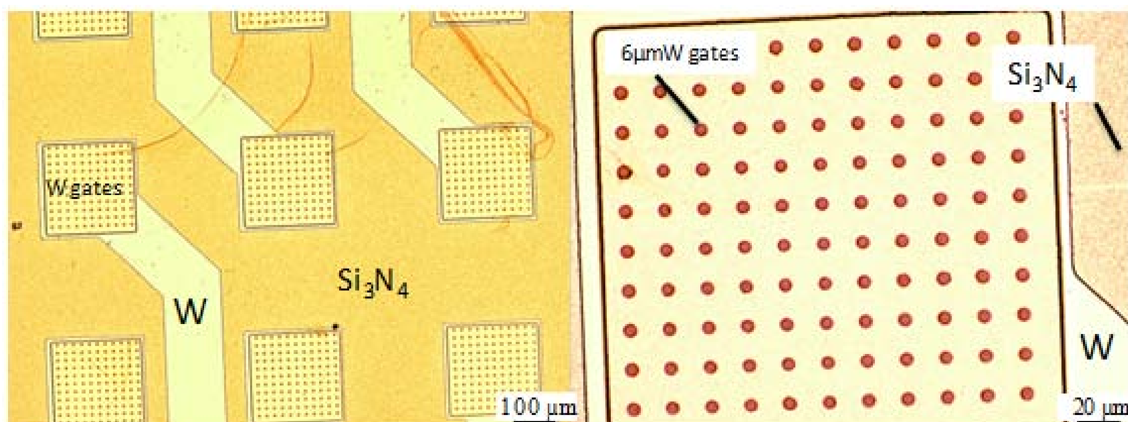

Figure 6.13. Optical micrographs of the second generation N-UNCD FEA. Left: 3x3 device. Right: Close-up of a given 225 µm x 225 µm pixel.

In addition, SEM images obtained from one of the pixels are shown in Figure 6.14.

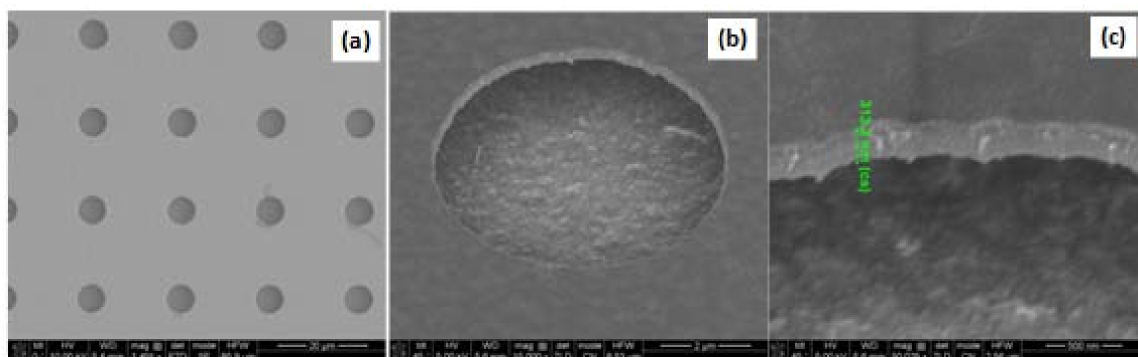

Figure 6.14. SEM images of the second generation N-UNCD FEA showing details of the single extraction gate. (a) Array of 6 µm W gates on the prototype, (b) detail of one of extraction gates, and (c) W extraction gate with an approximate thickness of 313 nm.

To corroborate that the SiO_2 BEO etching was complete and that the N-UNCD layer was effectively exposed, a SEM/EDS analysis was performed in one of the pixels. Results presented in Figure 6.15 indicate that the top layer effectively corresponds to W and the emitters layer is composed of a carbon based material, in this case N-UNCDs.

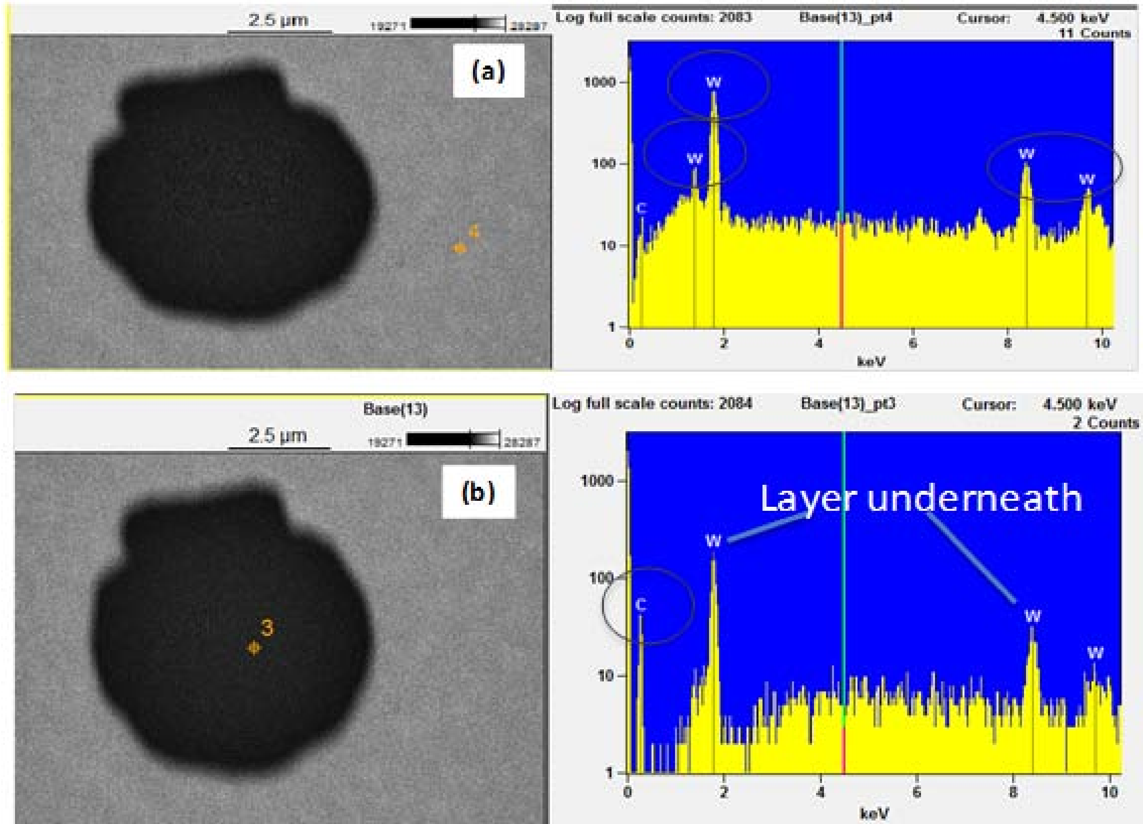

Figure 6.15. SEM/EDX analysis performed in one of the gates of the second generation N-UNCD FEA. (a) W extraction gate, (b) N-UNCD field emitter layer.

6.4. FE TESTING OF THE SINGLE GATE FEA

Following the same procedure described in Sections 4 and 5, the *I-V* characteristics of the single gate N-UNCD FEA were evaluated, and results are presented in Figure 6.16. The initial *I-V* behavior is compared to the ones obtained after a few minutes of operation, and after 24 hr of the first FE testing. A reduction in the emission current over times is observed, especially when initial results are compared to those obtained after a few cycles of operation. This reduction in emission current can be associated to accumulation of charged in the walls of the device, which could prevent further electrons from being extracted [4, 5]. On the other hand, no significant difference is found between the *I-V* characteristics obtained after a few cycles of operation or after 24 hours of operation. These results indicate that a stable operation of the N-UNCD FEA should be expected in the long run.

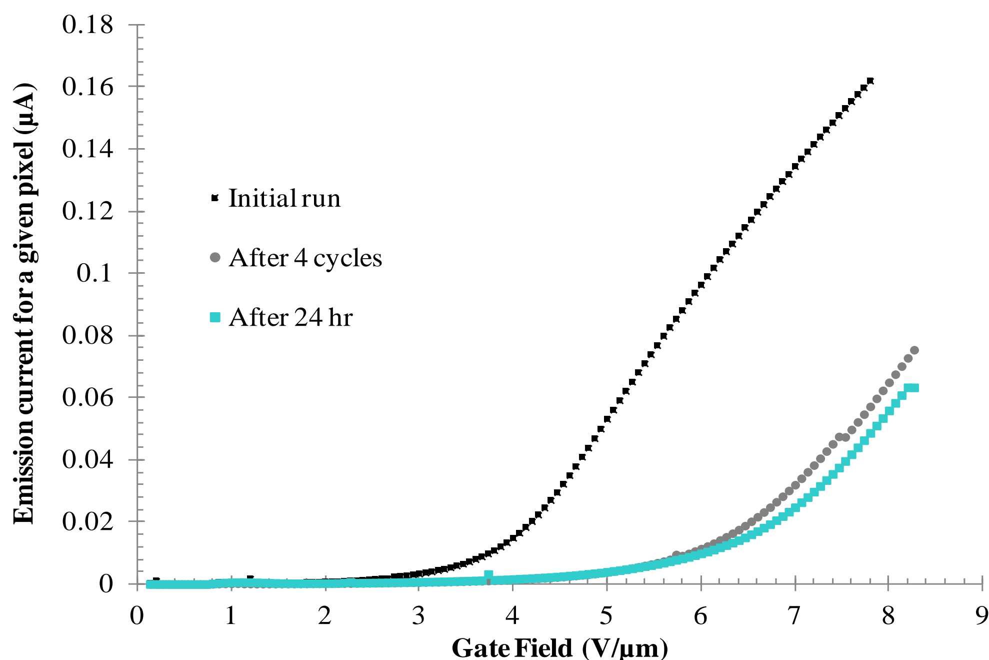

Figure 6.16. Measured *I-V* characteristics of the single gate N-UNCD FEA at different times.

The effect of the anode voltage on the FE performance of the single gate FEA was also evaluated. For this, the *I-V* characteristics of a given pixel of the FEA were evaluated at three different anode voltages: 0 kV, 4.5 kV and 8 kV, Figure 6.17. For a given extraction voltage, a small increase in the emission current is observed as the anode voltage is increased. This behavior could be due to a reduction on the space-charge limiting effects. As the electrons leaving the N-UNCDs and moving toward the extraction gate are rapidly accelerated away from the vicinities of the emitters by high anode potentials, their negative effect on the extracting field is reduced; thus allowing for additional electrons to be extracted. This rapid acceleration of the electron beam is actually a strategy employed in systems such free-electron lasers in which high current, high brightness electron sources are required [53].

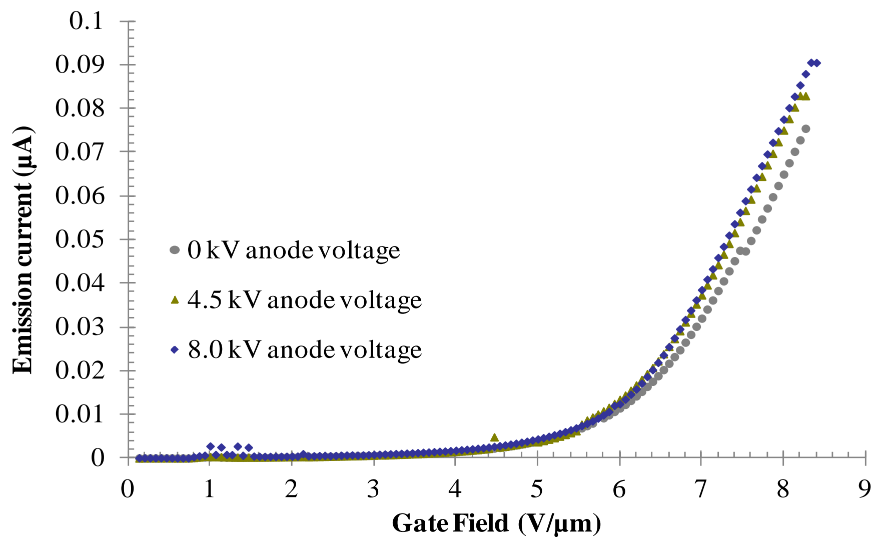

Figure 6.17. Influence of anode high voltages on the *I-V* characteristics of the single gate N-UNCD FEA.

Finally, a comparison of the I-V characteristics of the first and second generation N-UNCD field emitter arrays is presented in Figure 6.18. In every case, a higher emission current is observed for the single gate N-UNCD FEA.

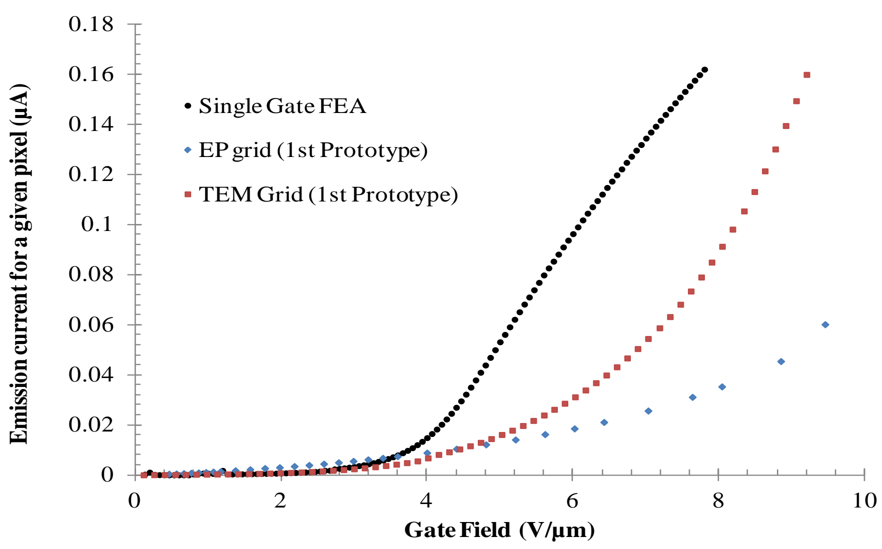

Figure 6.18. Comparison of the I-V characteristics of the first and second generation N-UNCD FEAs.

However, results presented in Figure 6.18 compare only the emission currents measured for the initial cycle of each of the prototypes. A comparison of the I-V characteristics obtained for FEAs after 24 hr of operation or more would provide further insight on their performance. Unfortunately, no samples of the first FEA prototype were available to make this comparison.

6.5. FABRICATION OF THE DOUBLE GATE FEA

An attempt to fabricate the double gate N-UNCD FEA shown in Figure 6.19 was performed. To add the second gate, three steps were added to the microfabrication process of the single gate FEA. These additional steps included: PECDV deposition of a 2 μm layer of SiO2 at 100 ^{0}C, sputtering of a 200 nm layer of W onto this 2 μm layer of SiO_2, and a final UV lithography step to etch holes of 16 μm in diameter through the recently deposited layers of W and SiO_2.

Anode/
plate for current
measurement
16 μm
Collimation gate
2 μm
Extraction gate
3 μm
6 μm
Cathode/UNCDs
20 μm

Figure 6.19. Proposed double gate second generation N-UNCD FEA for microfabrication.

Several attempts to fabricate of this second gate FEA were carried out, however results were unsuccessful. Figure 6.20 presents micrographs indicating some of the issues encountered during the steps leading to the microfabrication of the second gate.

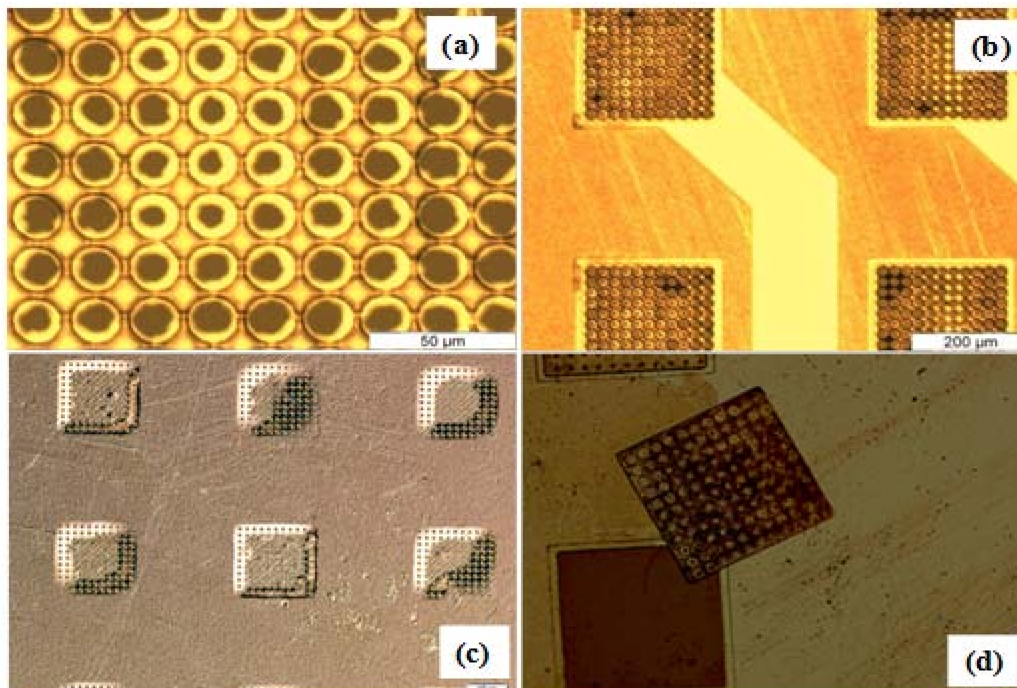

Figure 6.20. Micrographs indicating issues found during the microfabrication of a double gate N-UNCD FEA.

Figures 6.20-(a) and 6.20-(b) show that a good alignment between the first and second gates can be obtained using the MA-6 mask aligner. This is a promising result for future attempts to microfabricate the double gated FEA. However, “bubbling” effect was observed during the BOE etching of the 2 µm SiO_2 layer separating the two W gates (Figure 6.20). This could be due to an undercut of the SiO_2 generated by the isotropic nature of etching with BOE. In addition, delamination of the 200 nm layer right on top of some of the pixels was observed, Figure 6.20-(d). In Figure 6.20-(d) it is seen how the W gate layer on the of one of the pixels is removed, this could also be a consequence of SiO_2 undercut due to the isotropic nature of BOE etching. Furthermore, delamination of the tungsten layer during the deposition process was observed when the thickness of this layer was larger than 200 nm. This is not shown in Figure 6.20, but should be taken into account for future attempts to microfabricate a double gate N-UNCD FEA.

7. CONCLUSIONS

In an early stage of this work, the Particle in Cell code OOPIC Pro was used to simulate the FE characteristics of a triode structure. The emission of electrons from the cathode was simulated according to the Fowler-Nordheim theory. Simulations were run for grid voltages between 20 V and 70 V and anode voltages between 30 kV and 120 kV.

- *I-V* curves obtained from the simulations indicated that the emission current was controlled via extraction voltage, while the energy of the electrons at the anode was determined by the acceleration voltage.
- The electron beam was found to have a divergent trajectory when no focusing electrodes were employed. This divergent trajectory was modified into a convergent one by adding focusing electrodes to the simulated triode structure.
- Space charge limitation effects were found to become important at grid voltages between 43 V and 58 V, depending on the anode voltage.
- In general, these preliminary simulations indicated the technical feasibility of the proposed electron source to be used as cold cathode in the flat panel X-ray source.

Based on simulations results, a first electron source prototype was successfully fabricated using conventional microfabrication techniques. The microfabrication work of this prototype was carried out in the clean room facilities of the Center for Nanoscale materials at Argonne National Laboratory. This first prototype was composed of 9 pixels arranged in a 3x3 array using planar N-UNCD films as field emitters.

- In this first prototype, each pixel was composed of a N-UNCD based cathode and a free-standing copper grid used extraction gate. Cathode and grid were separated by a 5 µm stand-off layer of SiO_2 deposited by PECVD.
- The first prototype was successfully tested in a high vacuum system built for the purpose. Emission currents in the order of 0.05 to 3.0 µA per pixel were measured when electric fields in the order of 4 to 20 V/µm were applied.

- Problems with the delamination of the electroplated copper grid were encountered during the microfabrication of the first FEA prototype. These delamination issues, together with incomplete etching of the SiO_2 layer placed between the N-UNCDs and the copper grid affected the electron emission in the first N-UNCD FEA prototype.
- When compared to results obtained using the electroplated grid, emission currents about 50% higher were obtained when a TEM grid was used to extract the electrons in the first FEA prototype.

Having confirmed electron field emission from the first N-UNCD FEA prototype, a second generation FEA was designed through simulations with better performance and FE stability.

- Two alternative designs in the form of single and double gate N-UNCD FEA configurations were simulated using a PIC code. Results obtained from the simulation of the single gate structure were compared to those obtained with the first FEA prototype.
- According to these simulations, emission currents per pixel up to 2.5 times higher than the ones obtained from the first FEA prototype are expected for the single gate FEA.
- It was found that for small gate apertures (between 6 and 10 µm), up to 30% higher emission currents should be expected when compared to bigger gate apertures (20 µm and 30 µm).
- Since the simulation of the single gate geometry resulted in a divergent electron beam, the performance of a double-gate FEA configuration was also evaluated. Results indicated that for collimation gates between 2 and 3 times the size of the extraction gate a convergent electron beam could be obtained with negligible effect on the emission current.

These second sets of simulations led to the microfabrication of an alternative single gate N-UNCD FEA. The microfabrication of this second generation N-UNCD FEA was also carried out in the clean room facilities of the Center for Nanoscale Materials at Argonne National Laboratory.

- Same as the first prototype, this second generation FEA was composed of 9 pixels arranged in a 3x3 array using planar N-UNCD films as field emitters. Field emission from each pixel could be addressed individually.
- In this alternative design, the free-standing copper grid was replaced by a tungsten layer composed of a matrix of 11x11 extraction gates. Each extraction gate corresponds to a circular aperture of 6 µm in diameter. N-UNCD cathode and extraction gates were separated by a 3 µm stand-off layer of SiO_2 deposited by PECVD.
- Design changes incorporated into the second generation N-UNCD FEA solved the delamination problems found for the first prototype.
- The FE characteristics of this alternative FEA were evaluated according to its I-V behavior. An emission current around 0.14 µA per pixel was measured for an extraction field of 7 V/µm. This value is higher than the 0.08 µA per pixel obtained from the first prototype for the same extraction field. Current stability issues were still found in this device. Recommendations to address these current stability issues are also included in this work.

The microfabrication of a double gate FEA prototype was also attempted but results were unsuccessful. The main issues during the microfabrication of this double-gated device were encountered during the steps involving etching of the SiO_2 layers used as stand-off between the cathode and the first gate; and between the first and second gate. Recommendations to solve these problems are presented in Section 8 of this document.

8. RECOMMENDATIONS FOR FUTURE WORK

This project led to the fabrication and testing of two different N-UNCD based electron sources prototypes to be used as cold cathode in the flat panel transmission X-ray source. As shown in Section 6, OOPIC Pro simulations were also conducted for a double-gated N-UNCD based FEA. The presence of this second gate should allow the collimation of the electron beam.

The fabrication of a double gated N-UNCD FEA prototype was attempted but results were unsuccessful. In this regard, developing an alternative process to fabricate this double gated FEA is recommended. The main problem found during the microfabrication of the double-gated prototype was associated to over-etching of the SiO_2 layer used to separate the tungsten layers of the first and second gates, as well as the SiO_2 layer placed between the N-UNCDs and the tungsten layer of the extraction gate. Also, when the profile of the single gate FEA was measured, a difference in level of 1.5 μm was found between the top of each of the pixels and their vicinities. This difference in level can lead to a non uniform deposition of the layer, allowing for etching of SiO_2 in places where it should not occur.

As a result, two alternatives are proposed to attempt the successful fabrication of a double gate N-UNCD FEA prototype. In the first one, the deposition by PECVD of a 1.5 μm layer of SiO_2 in the vicinities of the pixels is recommended before sputtering the W layer used for the extraction gates. This additional SiO_2 deposition is expected to flatten the profile of the FEA in the vicinities of the pixels, improving the results in the subsequent W and SiO_2 etching steps using SF_6 RIE and BOE respectively. If this alternative proves unsuccessful, the deposition of the 1.5 μm layer of SiO_2 is still recommended. However, replacing the isotropic BOE SiO_2 etching process by a more anisotropic alternative, such CHF_3 RIE etching should be considered.

The FE characteristics of this double gated FEA should be tested and compared to results obtained from the other two prototypes fabricated. It is recommended to evaluate collimation characteristics of the second gate by measuring the I-V characteristics at different collimation gate to extraction gate voltage ratios. Simulation values presented in Section 6.2.2 should provide a good starting point for these collimation experiments.

Since the experimental apparatus built for this project was shown to be effective on producing and measuring transmission X-rays generated when a CNT based FE electron source was used, the generation of X-rays up to 30 kV from the N-UNCD FEA prototypes should be possible. Nonetheless, high voltage breakdown issues were encountered during the experiments. Consequently, developing strategies to mitigate the probability of high voltage breakdown is considered paramount in any future research.

Results presented in this dissertation were all obtained for DC voltages. Considering pulse mode operation could provide an alternative mitigating technique to problems associated to the accumulation of charges in the insulating walls of the FEA.

APPENDIX A

INPUT FILE USED FOR THE OOPIC PRO SIMULATIONS

Flat Panel X-ray- Field emission OOPIC PRO Simulations

{

This input file is used to determine the field emission characteristics
of a carbon-nanotube-based cathode located in a triode structure.
OOPIC PRO is the software used in the simulations.
The emitters are simulated according to the Fowler-Nordheim field
emission model implemented in OOPIC. This input file was adapted
from the Fowler_Nordheim.inp input file found in the OOPIC PRO libraries.
The model, which uses cartesian coordinates, corresponds to a triode structure,
composed of a cathode, an anode and an extraction grid. A DC potential difference
is generated across the lower boundary (cathode) and a medium boundary (extraction
grid)
in order to extract the electrons. A much higher DC potential is generated across
the cathode-anode gap in order to accelerate the electrons toward the anode.

Electrons are emitted from a portion of the lower boundary,
according to the Fowler-Nordheim field emission model.

Diagnostics of how much energy they have upon arrival upper boundary (anode)
is kept. Also, the energy, velocity, and distribution of the electrons striking the anode
are diagnosed.

An electrostatic field solver is used.
Modification V3 = All the grids are in place
Modification V4 = Central grids are removed
Modification V5 = Focusing electrodes where added
Modification V6 = Cell size is reduced (80 YCells) 1mm height for the cell
Modification V6-1= Trying to implement a pulse mode for the extracting voltage
(rise_time effect)
Modification V6-2= Voltage diagnostics at the anode is added Modification V9= Rise
time established as a variable of the simulation (initially set at 10 ps)

```
Modification V10= Focusing electrodes are added
}

Variables
{
 //*****************************************************************
 //*************** Geometrical Aspects of the Triode Structure ***************
//*****************************************************************
 //
 speedLight=2.99792458e+08
 //*************** Geometrical Aspects of Ext_Grid **************************
    Gridthik= 0.000003                // Thickness of the metal wire in the extracting grid
    Gridspace= 0.000015               // Open space in the extracting grid
    Gridheight= 0.000001              // Height of the extracting Grid - "Thickness if you
// want to call it that way"
 //
 //*************** Geometrical Aspects of Ext_Grid **************************
 //
  // ThickAnode= 0.00001                // Thickness of the Tungsten target
 //
//*****************************************************************
 //*************** Geometrical Aspects of the Triode Structure ***************
//*****************************************************************
   CellsX= (((6*Gridthik)+(5*Gridspace))*1000000)/3
  //CellsX=100
   numCellsX = CellsX                  // # of cells along horizontal axis

  xGridMKS = (6*Gridthik)+(5*Gridspace)                 // Width of the grid
  xMaxMKS = (6*Gridthik)+(5*Gridspace)        // Length of horizontal axis in meters
  yMaxMKS = 0.001.
  numCellsY = yMaxMKS*80000                  // # of cells along vertical   axis
```

```
  yGridMKS = 2                  // Distance between emitters and extraction grid

                     // Length of vertical   axis in meters
 //xDivisions= 51                           // # of divisions defined for the extraction grid
                                          // (For the sake of symmetry, it has to be a odd number)
 numEmitterCells = 0.5*numCellsX   // # of cells along the emitting surface.
                                          // This number increases the area of the emitter

  Grid_thik= Gridthik*1000000/3
  Grid_space= Gridspace*1000000/3
  Grid_height= Gridheight*1000000/1

dx=xMaxMKS/numCellsX
dy=yMaxMKS/numCellsY
d=1./sqrt(1./(dx*dx)+1./(dy*dy))
//timeStep=0.05*d/speedLight
yGrid=yMaxMKS/numCellsY
timeStep=0.5*yGrid/speedLight
risetime=10e-12                   // Rise Time of Extracting Voltage
 //
// *****************************************************************
 // *************** Potentials Applied to the Triode Structure ****************
// ******************************************************************
 //
  npart=1e+05                          // numerical weight of emitted particles
AnodePotential= 31000          // Accelerating voltage @ the anode (V) (positive     // for
electrons to be attracted
GridPotential= 50//105                    // Potential Specified @ extracting grid (V)
// (negative for electrons to be emitted)
CathodePot= 0 // Potential Specified at the emitting cathode (Must //  be negative respect
to GridPotential)
```

```
ElecPotential= 4000                    // Potential specified for the focusing lens (positive
//- electrons to be repeled)
 //
//*****************************************************************
 //*************** Potentials Applied to the Triode Structure ****************
//*****************************************************************
   }
//
//
//******************************************************************
//******* Definition of Geometry, Max and Min Coordinates in the Grid *********
//******************************************************************

   Region
   {
  Grid
  {
  J   = numCellsX              // number of grids in x
  x1s = 0.0                    // Lower coordinate in x1
  x1f = xMaxMKS                // Upper coordinate in x1
  n1=1.0


  K   = numCellsY              // number of grids in y
  x2s = 0.0                    // Lower coordinate in y
  x2f = yMaxMKS                // Upper coordinate in y
  n2=1.0

 Geometry = 1                  // 0 to specify Cylindrical Geometry
                               // 1 to specify Cartesian Geometry
  }
```

```
//
//*******************************************************************
//******* Definition of Geometry, Max and Min Coordinates in the Grid *********
//*******************************************************************
//
//
//*******************************************************************
//**************** Creation and Definition of Species **********************
//***************** to be used along the simulation  ***********************
//*******************************************************************
//
  Species
  {
   name = electrons                        // name is used below for emitter
   m = 9.11E-31                            // electron mass in KG
   q = -1.6e-19                            // electron charge in C
   rmsDiagnosticsFlag=1                    // Collect time history plots on RMS values for
                                           // beam size and velocity
   collisionModel=electron                 // Model to simulate collisions of electrons
  }
//
//******************************************************************
//**************** Creation and Definition of Species **********************
//***************** to be used along the simulation  ***********************
//*********************************************************************
   Control
   {
   dt = timeStep                 // the time step in s
   ElectrostaticFlag = 1         // specify use of the electrostatic field solve
   }
//
```

```
// The top boundary is a perfect conductor.
// It is further specified that some energy diagnostics should be collected
//   for particles that strike this boundary.
//
//*****************************************************************
//*********************** Begining Extrac_Grid ***********************
//*****************************************************************
//
//*****************************************************************
//*************** Bottom-Sides of the grid ***************************
//*****************************************************************
Equipotential
{
name=Extract_grid
// Segments for grid #1 (Counting from left to right)
Segment //Bottom boundary
{
 j1 = 0
 j2 = Grid_thik
 k1 = yGridMKS
 k2 = yGridMKS
 normal = -1
}
Segment // top boundary
{
 j1 = 0
 j2 = Grid_thik
 k1 = yGridMKS+Grid_height
 k2 = yGridMKS+Grid_height
 normal = 1
}
```

```
Segment // left Boundary
{
 j1 = 0
 j2 = 0
 k1 = yGridMKS
 k2 = yGridMKS+Grid_height
 normal = 1
}
Segment // right boundary
{
 j1 = Grid_thik
 j2 = Grid_thik
 k1 = yGridMKS
 k2 = yGridMKS+Grid_height
 normal = 1
}

// Segments for grid #2 (Counting from left to right)
Segment // Bottom boundary
{
 j1 = (Grid_thik)+(1*Grid_space)
 j2 = (2*Grid_thik)+(1*Grid_space)
 k1 = yGridMKS
 k2 = yGridMKS
 normal = -1
}
Segment // Top boundary
{
 j1 = (Grid_thik)+(1*Grid_space)
 j2 = (2*Grid_thik)+(1*Grid_space)
 k1 = yGridMKS+Grid_height
```

```
 k2 = yGridMKS+Grid_height
 normal = 1
}
Segment // Left boundary
{
j1 = (Grid_thik)+(1*Grid_space)
j2 = (Grid_thik)+(1*Grid_space)
k1 = yGridMKS
k2 = yGridMKS+Grid_height
normal = -1
}
Segment // Right boundary
{
 j1 = (2*Grid_thik)+(1*Grid_space)
 j2 = (2*Grid_thik)+(1*Grid_space)
 k1 = yGridMKS
 k2 = yGridMKS+Grid_height
 normal = 1
}

// Segments for grid #3 (Counting from left to right)
Segment // Bottom boundary
{
 j1 = (2*Grid_thik)+(2*Grid_space)
 j2 = (3*Grid_thik)+(2*Grid_space)
 k1 = yGridMKS
 k2 = yGridMKS
 normal = -1
}
Segment // Top boundary
{
```

```
 j1 = (2*Grid_thik)+(2*Grid_space)
 j2 = (3*Grid_thik)+(2*Grid_space)
 k1 = yGridMKS+Grid_height
 k2 = yGridMKS+Grid_height
 normal = 1
}
Segment // Left Boundary
{
 j1 = (2*Grid_thik)+(2*Grid_space)
 j2 = (2*Grid_thik)+(2*Grid_space)
 k1 = yGridMKS
 k2 = yGridMKS+Grid_height
 normal = -1
}
Segment // Right Boundary
{
 j1 = (3*Grid_thik)+(2*Grid_space)
 j2 = (3*Grid_thik)+(2*Grid_space)
 k1 = yGridMKS
 k2 = yGridMKS+Grid_height
 normal = 1
}

// Segments for grid #4 (Counting from left to right)
Segment // Bottom Boundary
{
 j1 = (3*Grid_thik)+(3*Grid_space)
 j2 = (4*Grid_thik)+(3*Grid_space)
 k1 = yGridMKS
 k2 = yGridMKS
 normal = -1
```

```
}
Segment // Top boundary
{
 j1 = (3*Grid_thik)+(3*Grid_space)
 j2 = (4*Grid_thik)+(3*Grid_space)
 k1 = yGridMKS+Grid_height
 k2 = yGridMKS+Grid_height
 normal = 1
}
Segment  // Left Boundary
{
 j1 = (3*Grid_thik)+(3*Grid_space)
 j2 = (3*Grid_thik)+(3*Grid_space)
 k1 = yGridMKS
 k2 = yGridMKS+Grid_height
 normal = -1
}
Segment // Right boundary
{
 j1 = (4*Grid_thik)+(3*Grid_space)
 j2 = (4*Grid_thik)+(3*Grid_space)
 k1 = yGridMKS
 k2 = yGridMKS+Grid_height
 normal = 1
}

// Segments for grid #5 (Counting from left to right)
Segment // Bottom boundary
{
 j1 = (4*Grid_thik)+(4*Grid_space)
 j2 = (5*Grid_thik)+(4*Grid_space)
```

```
 k1 = yGridMKS
 k2 = yGridMKS
 normal = -1
}
Segment // Top Boundary
{
 j1 = (4*Grid_thik)+(4*Grid_space)
 j2 = (5*Grid_thik)+(4*Grid_space)
 k1 = yGridMKS+Grid_height
 k2 = yGridMKS+Grid_height
 normal = 1
}
Segment  // Left Boundary
{
 j1 = (4*Grid_thik)+(4*Grid_space)
 j2 = (4*Grid_thik)+(4*Grid_space)
 k1 = yGridMKS
 k2 = yGridMKS+Grid_height
 normal = -1
}
Segment // Right Boundary
{
 j1 = (5*Grid_thik)+(4*Grid_space)
 j2 = (5*Grid_thik)+(4*Grid_space)
 k1 = yGridMKS
 k2 = yGridMKS+Grid_height
 normal = 1
}

// Segments for grid #6 (Counting from left to right)
Segment // Bottom Boundary
```

```
{
 j1 = (5*Grid_thik)+(5*Grid_space)
 j2 = (6*Grid_thik)+(5*Grid_space)
 k1 = yGridMKS
 k2 = yGridMKS
 normal = -1
}
Segment // Top boundary
{
 j1 = (5*Grid_thik)+(5*Grid_space)
 j2 = (6*Grid_thik)+(5*Grid_space)
 k1 = yGridMKS+Grid_height
 k2 = yGridMKS+Grid_height
 normal = 1
}
Segment // Left Boundary
{
 j1 = (5*Grid_thik)+(5*Grid_space)
 j2 = (5*Grid_thik)+(5*Grid_space)
 k1 = yGridMKS
 k2 = yGridMKS+Grid_height
 normal = -1
}
Segment // Right Boundary
{
 j1 = (6*Grid_thik)+(5*Grid_space)
 j2 = (6*Grid_thik)+(5*Grid_space)
 k1 = yGridMKS
 k2 = yGridMKS+Grid_height
 normal = 1
}
```

```
  xtFlag=0   // Tells OOPIC to take F as the voltage function instead of using A or C
//fill=1    // It implies the boundary is closed

// IdiagFlag = 1           // TData accumulator for particle current

 //tdelay = 2E-12
 //trise = 2E-15
 //tpulse = 2E-8
 //tfall = 2E-12
 //a0 = 1
 //a1 = 2

 // F = 2*step(sin((2*3.14/2E-11)*t + 90)) // Square Pulses

 // F=-100*pulse(t,2E-12,2E-12,2E-12,2E-12) - 100*pulse(t,10E-12,2E-12,2E-12,2E-
12)-5*pulse(t,20E-12,2E-12,2E-12,2E-12)
    a0 = 0
    a1 = 1
    C = GridPotential              // Voltage applied to the extraction grid
    trise = risetime

 //nxbins = 2.*numCellsX      // resolution of position diagnostic
 // number of spatial bins along boundary segment for Dist. Accumulation)

// nenergybins = 40              // resolution of the energy diagnostic
// energy_min  = 0               // in eV
// energy_max  = 30000           // in eV
 }

//****************************************************************
//******************** Top Sides of the Grid **************************
```

```
//*****************************************************************
//
//*****************************************************************
//*************************** Polarizer ***************************
//*****************************************************************
//Polarizer
//{
//  name=polarizer
//   j1 = 0
 //  j2 = numCellsX
//   k1 = yGridMKS
//   k2 = yGridMKS
//   normal=1
//   transmissivity=1

//   IdiagFlag = 1          // TData accumulator for particle current

//   Ihist_avg=10              // (int) Number of timesteps for averaging current plots.
//   Ihist_len=1024            // (int) Length of the current history arrays.
//  diagSpeciesName= electrons   // (string) species for distribution function
//  accumulation. If not present or set to "Noname", the diagnostic is off.
//   nxbins=100                // (int) Number of spatial bins along boundary segment for
                               // accumulation.
//   nenergybins = 40             // resolution of the energy diagnostic
//   energy_min  = 0      // in eV
 //  energy_max  = 30000        // in eV

//}
//*****************************************************************
//**************** Right Side of the Grid *************************
//*****************************************************************
```

```
//************************ End Extracting Grid ************************
//*****************************************************************
//
//*****************************************************************
//************************ Beginning Cathode *************************
//******************************************************************
//
// The bottom boundary is an equipotential surface.

Equipotential
{
 name=cathode
  j1 = 0
  j2 = numCellsX
  k1 = 0
  k2 = 0
  normal=1

 C = CathodePot                    // specified potential in V (negative respect to GridPot for
// electrons to be emitted)
}
//
//*******************************************************************
//************************ End Cathode********************************
//******************************************************************
//
//******************************************************************
//************************ F-N Emitter*******************************
//******************************************************************
//
// In the following lines, a portion (50%) of the bottom boundary surface is specified
```

```
// to be a surface that emits electrons via the Fowler-Nordheim field
// emission model.
//
//  Below, there are specificied the  Fowler-Nordheim parameters reported in the literature
//  for carbon nanotubes. Some of them are given their default value though
//
FowlerNordheimEmitter
{
   // Bottom side of the emitter of five microns hight
      j1 = ((numCellsX - numEmitterCells) / 2)        // Initial Possition of the emitter in X
      j2 = (numCellsX + numEmitterCells) / 2          // Final Possition of the emitter in X
      k1 = 0
      k2 = 0
      normal=1
 //
 //
 //
       speciesName = electrons                     // name from species group above
       np2c = npart                                // numerical weight of emitted particles
 //
 // Coefficient "A" of the Fowler-Nordheim field emission model.
       A_FN = 1.5414e-06       // The default value is 1.5414e-06, which is specified here.
 //
// Coefficient "beta" of the Fowler-Nordheim field emission model.
          beta_FN = 2200.        // Field enhancement of the material.
// The default value is 1.  Here, we specify beta_FN = 2200, which corresponds to // a
accepted value for Carbon nanotubes

 //
       B_FN = 6.8308e+09       // Coefficient "B" of the Fowler-Nordheim FE model.
                               // The default value is 6.8308e+09, which is specified here.
```

```
//
//
      C_v_FN = 0.       // Coefficient "C_v" of the Fowler-Nordheim field emission model.
                        // The default value is 0, which is specified here.
//
//
      C_y_FN = 3.79e-05        // Coefficient "C_y" of the Fowler-Nordheim FE model.
                               // The default value is 3.79e-05, which is specified here.
//
//
      Phi_w_FN = 5.0.// The work function "Phi_w" for electrons in the surface, in eV.
                        // value 0f 5 eV taken as representative for CNTs samples.
//
                        // The number of intervals to be used for emitting particles.
     nIntervals = 0     // The default value of 0, which is specified here.
                        // In the default case, nIntervals will be reset to the # of cells
                        // along the emitting boundary (with a minimum of 2), which  is
                        // the most reasonable thing to do.
//
//       fill=1                          // it implies the boundary is closed

}


//**************************************************************
//******************** Begining of the Anode ********************
//**************************************************************
Equipotential
{
  name = anode
 //  Top side of the anode
```

```
   j1 = 0
   j2 = numCellsX
   k1 = numCellsY
   k2 = numCellsY
   normal = -1                    // Unit direction of the face normal. (-1):Down/Left

   C = AnodePotential             // Specified potential in V (+  for e- to be attracted)

//  In the following code lines it is specified the energy diagnostics to be collected
//  for particles that strike on this boundary.

 IdiagFlag = 1                    // TData accumulator for particle current
 Ihist_avg=100                    // (int) Number of timesteps for averaging current plots.
 Ihist_len=1024                   // (int) Length of the current history arrays.
 nxbins = 5.*numCellsX            // resolution of position diagnostic
// number of spatial bins along boundary segment for Dist. Accumulation)
 nenergybins = 5.*numCellsX       // resolution of the energy diagnostic
 energy_min  = 0                  // in eV
 energy_max  = 31000              // in eV
 }




//**********************************************************
//************************* Side boundaries *********************
//**********************************************************
// The left boundary is a simple dielectric
Dielectric
{
 j1 = 0
```

```
 j2 = 0
 k1 = 0
 k2 = numCellsY
 normal=1
}
// The right boundary is a simple dielectric
Dielectric
{
 j1 = numCellsX
 j2 = numCellsX
 k1 = 0
 k2 = numCellsY
 normal = -1
}
//**************************************************************
//************************* Side boundaries ***********************
//**************************************************************
//**************************************************************
//
//**************************** Begining **************************
//************************* Initial density of electrons ***************
//**************************************************************

//Load
//{
//	units=EV
//	x1MinMKS = 0
//	x1MaxMKS = 0.00015
//	x2MinMKS = 0.000070
//	x2MaxMKS = 0.001
//	speciesName = electrons
```

```
//      density = 1.0e15
//      np2c = 1.0e6
//      LoadMethodFlag =0
//      temperature = 0
//}

//**********************************************************
//************************ End ******************************
//*********************** Initial density of electrons **************
//**********************************************************

Diagnostic
{
  j1 = 0
  j2 = numCellsX
  k1 = numCellsY-1
  k2 = numCellsY-1
  title = Anode Voltage
  VarName = phi
  HistMax = 1024
  Comb = 2
  x1_Label=X
  x2_Label=Time
  x3_Label=Potential
}

//**********************************************************
//******************** Focusing lens ***************************
//**********************************************************
Equipotential
{
```

```
name=Foc_left // left focusing Electrode.
Segment // Right side
{
 j1 = 1
 j2 = 1
 k1 = 25
 k2 = 27
 normal=1
}
Segment // Left side
{
 j1 = 0
 j2 = 0
 k1 = 25
 k2 = 27
 normal=1

}
Segment// Up side
{
 j1 = 0
 j2 = 1
 k1 = 27
 k2 = 27
 normal=1

}
Segment // Bottom side
{
 j1 = 0
 j2 = 1
```

```
 k1 = 25
 k2 = 25
 normal=-1

}
 C=ElecPotential
}

Equipotential
{
name=Foc_Right // Focusing lens...Right side
Segment // Right side
{
 j1 = numCellsX
 j2 = numCellsX
 k1 = 25
 k2 = 27
 normal=-1
}
Segment // Left side
{
 j1 = numCellsX-1
 j2 = numCellsX-1
 k1 = 25
 k2 = 27
 normal=-1

}
Segment// Up side
{
 j1 = numCellsX-1
```

```
 j2 = numCellsX
 k1 = 27
 k2 = 27
 normal=1

}
Segment // Bottom side
{
 j1 = numCellsX-1
 j2 = numCellsX
 k1 = 25
 k2 = 25
 normal=-1

}
 C=ElecPotential
}
//************** Final bracket ***********
}
```

APPENDIX B

DERIVATION OF THE FOWLER-NORDHEIM EQUATION

This appendix presentes further details in the derivation of the Fowler-Nordheim equation. This derivation was taken and adapted from Fursey, 2005 [5].

Quantitative calculation of the field emission process using the Fowler-Nordheim theory usually involves the evaluation of the emission current density as a function of the electric field. To perform this calculation, the probability for electrons to tunnel through the potential barrier needs to be determined. To calculate this probability, the transparency of the potential barrier (D), and the flow of electrons (N) from the emitter's surface toward the barrier should be computed and integrated over the electrons energy. In this process, the Fowler-Nordheim theory is based on the following assumptions:

1. The metal is assumed to obey the Sommerfeld free electron model with Fermi-Dirac statistics.
2. The emitter's surface is assumed to be planar. In other words, the one-dimensional problem is considered. This assumption can be applied because n most cases the thickness of the potential barrier in fields of 10^6-10^8 V/cm is several orders of magnitude less than the emitter radius. Therefore, the external field can be assumed to be uniform along the surface.
3. The potential $U_i(x)$ within emitters is considered constant $U_i(x) = const = -U_0$.
4. The potential outside the emitters' potential barrier is entirely due to image forces $U_x = -e^2/4x$
5. The calculations are performed for the temperature T = 0 K.

Based on these assumptions, the current density is calculated as:

$$j = e\int_0^\infty n(E_x)D(E_x, F)dE_x \tag{B.1}$$

In this equation, e is the electron charge, $n(E_x)$ is the number of electrons per second having energies between E_x and E_x+dE_x, incident on a 1 cm^2 of the barrier surface

from within the emitters. $E_x = p_x^2 / 2m$ is the portion of the electron kinetic energy carried by the momentum component p_x normal to the surface. m is free electron rest mass, and F is the externally applied electric field.

The barrier transparency is calculated using the method of Wentsel-Kramers-Brillouin (WKB) approximation. The shape of the potential barrier, under the influence of the applied electric field is then given by:

$$U(x) = -\frac{e^2}{4x} - eFx \tag{B.2}$$

Consequently, for this potential barrier the transparency is given by

$$D(E_x, F) = \exp\left[-\frac{8\pi(2m)^{1/2}}{3he}\right]\frac{|E_x|^{3/2}}{F}\upsilon(y) \tag{B.3}$$

Where $\upsilon(y)$ is the Nordheim function:

$$\upsilon(y) = 2^{-1/2}\left[1+(1-y^2)^{1/2}\right]^{1/2} \bullet \left[E(k) - \left\{1-(1-y^2)^{1/2}\right\}\right]K(k) \tag{B.4}$$

Where

$$y = \frac{(e^3F)^{1/2}}{\Phi}, \tag{B.5}$$

And

$$E(k) = \int_0^{\pi/2} \frac{d\alpha}{(1-k^2\sin^2\alpha)^{1/2}}, \qquad K(k) = \int_0^{\pi/2} (1-k^2\sin^2\alpha)^{1/2}\, d\alpha \tag{B.6}$$

The equations above, are complete elliptic integrals on the first and second kinds, and

$$k^2 = \frac{2(1-y^2)^{1/2}}{1+(1-y^2)^{1/2}} \tag{B.7}$$

Therefore, using equation A.3, the Fowler-Nordheim equation at T=0 is expressed by,

$$j = \frac{e^3}{8\pi h}\frac{F^2}{t^2(y)\Phi}\exp\left[-6.83\times10^7 \frac{\Phi^{3/2}}{F}\upsilon(y)\right] \tag{B.8}$$

Expressing the work function Φ in eV, F in V/cm and j in A/cm^2, the FN equation is expressed by

$$j = 1.54\times10^{-6} \frac{F^2}{t^2(y)\Phi}\exp\left[-6.83\times10^7 \frac{\Phi^{3/2}}{F}\upsilon(y)\right] \tag{B.9}$$

With,

$$y = 3.79\times10^{-4}\cdot\sqrt{F}/\Phi, \quad t(y) = \upsilon(y) - \frac{2y}{3}\frac{d\upsilon(y)}{dy} \tag{B.10}$$

Tabulated values of t(y) and $\upsilon(y)$ can be found elsewhere and are presented in this Appendix C

APPENDIX C

TABULATED VALUES FOR THE FN FUNCTIONS s(y) and $\upsilon(y)$ [54]

As described in Sesion 2 and Appendix B, the FN equation includes an expression for a function $v(y)$. However, Burges and Kroemer [54], have found a mathematical error in the equation originally defined in the FN theory. As a consequence, they have recalculated the values of v(y) ans s(y) and results are tabulated below.

Table C.1. Corrected values of v(y) ans s(y). Adapted from [54]

y	$v(y)$	$s(y)$
0	1.0000	1.0000
0.05	0.9948	0.9995
0.1	0.9817	0.9981
0.15	0.9622	0.9958
0.2	0.9370	0.9926
0.25	0.9068	0.9885
0.3	0.8718	0.9835
0.35	0.8323	0.9777
0.4	0.7888	0.9711
0.45	0.7413	0.9637
0.5	0.6900	0.9554
0.55	0.6351	0.9464
0.6	0.5768	0.9366
0.65	0.5152	0.9261
0.7	0.4504	0.9149
0.75	0.3825	0.9030
0.8	0.3117	0.8903
0.85	0.2379	0.8770
0.9	0.1613	0.8630
0.95	0.0820	0.8483
1	0.0000	0.8330

BIBLIOGRAPHY

[1] A. Worlbarst, [*Physics of Radiology*] Medical Physics Publishing. Madison, WI. (2005).

[2] C. M. Posada, C. H. Castano, E. J. Grant, and H. K. Lee, "*Simulation of the Electron Field Emission Characteristics of a Flat Panel X-ray Source,*" J. Vac. Sci. Technol. B, 30 (2), 022201 (2012).

[3] E. J. Grant, C. M. Posada, C. H. Castano and H. K. Lee, *"A Monte Carlo Simulation Study of a Flat Panel X-Ray Source,"* Appl. Radi. and Isot. 70, 8 (2012).

[4] R. H. Fowler, and L. Nordheim, *"Electron emission in Intense Electric Fields,"* Proc. R. Soc. Lond. A, 119, pp. 173-181 (1928).

[5] G. Fursey, [*Field Emission in Vacuum Microelectronics*] Kluwer Academic/Plenum Publishers. New York, NY. (2005).

[6] W. Zhu, [*Vacuum Microelectronics*] John Wiley & Sons, Inc. New York, NY. (2001).

[7] E. J. Grant, C. M. Posada, C. H. Castano, and H.K. Lee, *"Electron field emission particle in cell (PIC) coupled with MCNPX simulation of a CNT-based flat-panel-X-ray source,"* Proc. of SPIE, 7961-7 (2011).

[8] E. J. Grant, C. M. Posada, R. Divan, A. Sumant, D. Rosenmann, L. Stan, A. Avachat, C. H. Castano, and H. K. Lee, "*Construction of a Flat-Panel Cold Cathode X-ray Source,*" SPIE defense, security and sensing, 8709-31, (2013).

[9] R. C. Smith and S.R.P. Silva, *"Design of carbon nanotubes for large-area electron field-emission cathodes,"* Journal of the SID, 16, pp. 615-624 (2008).

[10] Z. B. Li, S.Z., Deng and N.S., Xu, *"Mechanism of field electron emission from carbon nanotubes,"* Front. Phys., 3, 305 (2006).

[11] S. Chhoker, S. K. Srivastava and V.D. Vankar, *"Field Emission Properties of Carbon Nanostructures: A Review,"* Int. Work. on Phys. Semi. Dev, 2007. IWPSD, 16-20 Dec. 2007 pp. 820-826.

[12] I. Brodie, *"Keynote Address to the First International Vacuum Microelectronics Conference, June 1998: Pathways to Vacuum Microelectronics,"* IEEE Transactions on Electron Devices, 36.pp. 2637-2640 (1989).

[13] P. Kruit, *[Introduction to Charged Particle Optics],* Class Notes, Delft University of Technology, Delft, The Netherlands (2010).

[14] J. B. Hudson, [*Surface Science: An Introduction*] John Wiley & Sons, Inc. Troy, NY. 27-48 (1998).

[16] R.G. Forbes and J.H.B Deane, *"Reformulation of the standard theory of Fowler Nordheim tunneling and cold field electron emission"* Proc. R. Soc. A 463, pp. 2907-2927 (2007).

[17] O. Auciello and A.V. Sumant, *"Status review of the science and technology of ultrananocrystalline diamond (UNCD) films and application to multifunctional devices"* Diamond & Related Materials 19, 699 – 718 (2010).

[18] D. Zhou, D. M. Gruen, L.C. Quin, T.G. McCauley, and A.R. Krauss, *"Control of diamond film microstructure by Ar additions to CH_4/H_2 microwave plasmas,"* J. Appl. Phys. 84, 1981 – 1989 (1998).

[19] A.M. Kovalchenko, J.W. Elam, A. Erdemir, J.A. Carlisle, O. Auciello, J.A. Linera, M.J. Pellin, D.M. Gruen, J.N. Hryn, "Development of ultrananocrystalline diamond (UNCD) coatings for multipurpose mechanical pump seals," Wear 270, 325 (2011).

[20] S.A. Getty, O. Auciello, A.V. Sumant, X. Wang D. P. Glavin, and P.R. Mahaffy, *"Characterization of Nitrogen-Incorporated Ultrananocrystalline Diamond as a Robust Cold Cathode Material,"* Proc. SPIE 7679, 7679N-1 (2010).

[21] J.W. Baldwin, M.K. Zalalutdinov, T. Feygelson, B.B. Pate, J.E. Butler, and B.H. Houston,*"Nanocrystalline diamond resonator array for RF signal processing,"* Diamond Relat. Mater. **15**, 2061 (2006).

[22] G. Chimowa, *"Synthesis and characterization of nano-crystalline diamond films,"* MS. Thesis, Faculty of Science, University of the Witwatersrand, Johannesburg (2011).

[23] A.V. Sumant, O. Auciello, H. C. Yuan, Z. Ma, R. W. Carpick, and D.C. Mancini, *"Large Area Low Temperature Ultrananocrystalline Diamond (UNCD) Films and Integration with CMOS Devices for Monolithically Integrated Diamond MEMS/NEMS-CMOS Systems,"* Proc. SPIE 7318, 731817 (2009).

[24] T. Lin, G.Y. Yu, A. T. S. Wee, Z. X. Shen, and K. P. Loh, *"Compositional mapping of the argon-methane-hydrogen system for polycrystalline to nanocrystalline diamond film growth in a hot-filament chemical vapor deposition system,"* Appl. Phys. Lett. **77,** 2692 (2000).

[25] R. Arenal, [*Ultrananocrystalline Diamond, 2nd Edition*] Chapter 4: n-Type Nanocrystalline Diamond Films: Synthesis, Structure, Composition, Properties, and Applications, William Andrew Publishing, Oxford, 2012.

[26] S. Bhattacharyya, O. Auciello, J. Birrell, J. A. Carlisle, L. A. Curtiss, A. N. Goyotee, D. M. Gruen. A. R. Krauss, J. Schlueter, A. Sumant, and P. Zapol, *"Systhesis and characterization of highly-conducting nitrogen-doped ultrananocrystalline diamond films"* Appl. Phys Lett. 79, 1441 (2001).

[27] A. Rokhlenko, K.L. Jensen, and J.L. Lebowitz, *"Space charge effects in field emission: One dimensional theory,"* J. Appl. Phys. 107, 014904 (2010).

[28] R. A. Kishek, S. Bernal, C.L. Bohn, D. Grote, I. Haber, H. Li, P. G. O'Shea, M. Reiser, and M. Walter, *"Simulations and experiments with space-charge dominated beams,"* Phys. Plasmas 10, 2016 (2003).

[29] OOPIC Pro User's Guide, Version 2.0.2. Tech-X Corporation. http://20.txcorp.com/pdf/OOPIC_Pro/documentation/OOPIC_Pro_UsersGuide.pdf

[30] J.P. Verboncoeur, A.B. Langdon and N.T. Gladd, *"An object-oriented electromagnetic PIC code,"* Computer Physics Communications, 87, 199-211 (1995).

[31] Verboncoeur J P, *"Particle simulation of plasmas: Review and advances,"* Plasma Phys. Control. Fusion 47 A231-A260 (2005).

[32] A. Barrie, *"Modeling Differential Charging of Composite Spacecraft Bodies Using the Coliseum Framework,"* MS. Thesis, Faculty of Engineering, Virginia Polytechnic Institute and State University, Blacksburg, VA (2006).

[33] K. Paul, "*VORPAL for Simulating RF Breakdown,"* Tech-X Corporation. Fermilab MuCool RF Workshop III, July 2009.

[34] Y. Di, W. Lei, X. Zhang, Y. Cui and Q. Wang, *"A New Triode Structure With a Carbon Nanotube Cathode,"* IEEE Transactions on Electron Devices 54, 3079 (2007).

[35] W.S. Chang, H.Y. Choi and J.U. Kim, *"Simulation of Field-Emission Triode Using Carbon Nanotube Emitters,"* Jpn. J. Appl. Phys. 45, 7175 (2006).

[36] H. Y. Choi, W. S. Chang, H. S. Kim, Y. H. Park and J. U. Kim, *"Acquisition of X-ray images by using a CNT cold emitter,"* Physics Letters A 357, 36 (2006).

[37] H. Y. Choi and J. U. Kim, *"Carbon-Nanotube (CNT)-Based Triode X-ray Tube Design by Using Computer Simulation,"* J. Korean Phys. Soc. 53, 1388 (2008).

[38] D.M. Garner, *"Modelling of Emitted Current Distribution and Electron Trajectories in the Thin-Film Field-Emission Triode,"* J. Vac. Sci. Technol. B 22, 1250 (2004).

[39] C. Posada, *"Simulation of the Field Electron Emission Characteristics of a Flat Panel X-ray Source,"* MS Thesis, Nuclear Engineering, Missouri University of Science and Technology, 2011.

[40] A. L. Musatov, Y. V. Gulyaev, K. R. Izrael'yants, E. F. Kukovitskii, N. A. Kiselev, O. Y. Maslennikov, I. A. Guzilov, A. B. Ormont, and E.G. Chirkova, *"A compact X-ray Tube with a Field Emitter Based on Carbon Nanotubes,"* J. Commun. Technol. El. 52, 714 (2007).

[41] J. Zhang, G. Yang, Y. Cheng, B. Gao, Q. Qiu, Y.Z. Lee, J.P. Lu and O. Zhou, *"Stationary scanning X-ray source based on carbon nanotubes field emitters,"* Appl. Phys. Lett. 86, 184104 (2005).

[42] . W. Luginsland, Y. Y. Lau, and R. M. Gilgenbach, *"Two-Dimensional Child-Langmuir Law"* Phys. Rev. Lett. 77, 4668 (1996).

[43] Y. Feng and J. P. Verboncoeur, *"Transition from Fowler-Nordheim field emission to space charged limited current density,"* Phys. Plasmas 13, 073105 (2006).

[44] K.L. Jensen, *"Space-charge effects in field emission: Three-dimensional theory,"*J. Appl. Phys 107, 014905 (2010).

[45] Krauss, A. R., Auciello, O., Ding, M. Q., Gruen, D.M., and Huang, Y., Zhirnov, V.V., Givargizov, E.I., Breskin, A., Chechen, R., Shefer, E., Konov, V., Pimenov, S., Karabutov, A., Rakhimov, A., and Suetin, N, *"Electron field emission for ultrananocrystalline diamond films,"* J. Appl. Phys. **89** (11), 2958-2967 (2001).

[46] Wang, X., Ocola, L.E., Divan R., Sumant, A.V., *"Nanopatterning of ultrananocrystalline diamond nanowires,"* Nanotechnology 23, 075301 (2012).

[47] Wang, S., Liu, Z., Sultana, S., Schreiber, E., Zhou, O., and Chang, S., *"A novel high resolution micro-radiotherapy system for small animal irradiation for cancer research,"* BioFactors, 30, 265-270 (2007).

[48] Yamamoto, S., *"Fundamental physics of vacuum electron sources,"* Rep. Prog. Phys., 69, 181-232 (2006).

[49] Al-Tabbakh, A.A., More, M.A., Joag, D.S., Mulla, I.S., and Pillai. V.K., *"The Fowler-Nordheim Plot Behavior and Mechanism of Field Electron Emission from ZnO Tetrapod Structures,"* ACS NANO 4 (10), 5585 -5590 (2010).

[50] Getty, S.A., King, T.T., Bis, R.A., Jones, H.H., Herrero, F., Lynch, B.A., Roman, P., and Mahaffy, P., *"Performance of a carbon nanotube field emission electron gun,"* Proc. SPIE, 6556, 655618 (2007).

[51] Chen, Y.C., Zhong, X.Y., Kabius, B., Hiller, J.M, Tai, N.H., and Lin, I.N., *"Improvement of field emission performance of nitrogen ion implanted Ultrananocrystalline diamond films through visualization of structure modifications,"* Diamond & Related Materials. 20, 238-241 (2011).

[52] Chen, Y.C., Tai, N.H., and Lin, I.N., *"Substrate temperature effects on the electron field emission properties of nitrogen doped ultra-nanocrystalline diamond,"* Diamond & Related Materials. 17, 457-461 (2007).

[53] P. Helfenstein, K. Jefimovs, E. Kirk, C. Escher, H. –W. Fink, and S. Tsujino, *"Fabrication of metallic double-gate field emitter arrays and their electron beam collimation characteristics,"* J. Appl. Physics 112, 093307 (2012).

[54] R. E. Burgess and H. Kroemer, *"Corrected Values of the Fowler-Nordheim Field Emission Functions v(y) and s(y),"* Phys. Review 90, 4 (1953).

VITA

Chrystian Mauricio Posada received his Bachelor of Science in Chemical Engineering from the Universidad Nacional de Colombia – National University of Colombia – in March 2008. For his undergraduate thesis, Mauricio worked on determining the optimum conditions for the transesterification reaction of castor bean oil for biodiesel production.

He joined the Missouri University of Science and Technology in 2009 , earning a Master of Science degree in Nuclear Engineering in May, 2011. His master's thesis was titled: "Particle-in-Cell Simulation of the Field Electron Emission Characteristics of a Flat Panel X-Ray Source". He completed his PhD in Nuclear Engineering in May, 2014. His PhD Dissertation is titled: "Development of a Nitrogen-Incorporated Ultrananocrystalline Diamond Films Based Field Emitted Array for a Flat-Panel X-ray Source".

As part of his graduate studies, Mauricio has also been a visiting researcher of the Center for Nanoscale Materials at Argonne National Laboratory, and the Charged Particle Optics Group at Delft University of Technology, the Netherlands.